

Study of nitrocarburizing plasmas using advanced spectroscopic diagnostics

Inauguraldissertation

zur

Erlangung des akademischen Grades

doctor rerum naturalium (Dr. rer. nat.)

an der Mathematisch-Naturwissenschaftlichen Fakultät

der

Universität Greifswald

vorgelegt von

Alexander Puth

geboren am 01. Mai 1991

in Aschaffenburg.

Greifswald, den 08. Juni 2020

Dekan: Prof. Dr. Gerald Kerth

1. Gutachter: Prof. Dr. Jürgen Röpcke

2. Gutachter: Prof. Dr. Holger Kersten

Tag der Promotion: 30.10.2020

Study of nitrocarburizing plasmas using advanced spectroscopic diagnostics

Contents	I
Abstract	IV
Introduction	V
List of symbols and abbreviations	VI
1 Nitriding and nitrocarburizing	
1.1 Definition and basic description	1
1.2 Methods and comparison	2
References	4
2 Plasma nitrocarburizing	
2.1 Definition of the plasma state	5
2.2 Conventional plasma nitrocarburizing	6
2.3 Active screen plasma nitrocarburizing	8
References	9
3 Plasma diagnostics	
3.1 Introduction into molecular spectroscopy	11
3.2 Laser absorption spectroscopy	13
3.2.1 Lead-salt diode laser sources	14
3.2.2 Quantum cascade laser sources	15
3.3 Fourier-transform spectroscopy	16
3.4 Frequency comb absorption spectroscopy	18
3.4.1 Frequency comb laser sources	18
3.4.2 Detection systems	20
References	23
4 Investigation at an industrial-scale ASPN reactor using an AS made of CFC	
4.1 Study of plasma-chemical processes as functions of the total gas flow and pressure	
4.1.1 Introduction	25
4.1.2 Experimental	27
4.1.3 Results and discussion	29
4.1.4 Summary and conclusion	34
References	35

4.2 Influence of H ₂ -N ₂ gas composition on structure and properties of expanded austenite	
4.2.1 Introduction	37
4.2.2 Materials and methods	38
4.2.3 Results	41
4.2.4 Discussion	46
4.2.5 Conclusions	48
References	49
4.3 Effects of admixed oxygen-containing species in ASPNC processes	
4.3.1 Introduction	51
4.3.2 Experimental	51
4.3.3 Results and discussion	52
4.3.4 Summary and conclusions	57
References	59
5 Investigation at a laboratory-scale ASPN reactor using an AS made of CFC	
5.1 Introduction	61
5.2 Experimental	63
5.3 Results and discussion	66
5.4 Summary and conclusions	73
References	75
6 Application of a FC for investigation of a laboratory-scale ASPN reactor using an AS made of CFC	
6.1 Introduction	77
6.2 Experimental	78
6.3 Methods	79
6.4 Results and discussion	81
6.4.1 General remarks	81
6.4.2 Rotational and translational temperatures	82
6.4.3 Concentrations	85
6.5 Summary and conclusions	86
References	88
7 Investigation of chemically similar plasma processes to PN	
7.1 Introduction	89

7.2 Experiment	90
7.2.1 Experimental arrangement	90
7.2.2 Optical arrangement	91
7.3 Applied methods	93
7.3.1 Determination of atomic and molecular densities via OES	93
7.3.2 Laser absorption spectroscopy	94
7.4 Results and discussion	95
7.4.1 Temperature measurements	95
7.4.2 Species densities	96
7.5 Plasma chemistry and kinetics	100
7.6 Conclusions	103
References	104
8 Summary, conclusions, and outlook	107
Declaration	109
Curriculum Vitae	110
Peer-reviewed publications	111
Contributions to conferences and workshops	112
Acknowledgments	114
Appendix	

Abstract

The active screen plasma nitrocarburizing (ASPNC) technology is a state-of-the-art plasma-assisted heat treatment for improving surface hardness and wear resistance of metallic workpieces based on thermochemical diffusion. In comparison to conventional plasma nitrocarburizing, the use of an active screen (AS) improves thermal homogeneity at the workload and reduces soot formation. Further it can serve as a chemical source for the plasma processes, e.g. by use of an AS made of carbon-fibre reinforced carbon. This compilation of studies investigates the plasma-chemical composition of industrial- and laboratory-scale ASPNC plasmas, predominantly using *in-situ* laser absorption spectroscopy with lead-salt tuneable diode lasers, external-cavity quantum cascade lasers, and a frequency comb. In this way the temperatures and concentrations of the dominant stable molecular species HCN, NH₃, CH₄, C₂H₂, and CO, as well as of less prevalent species, were recorded as functions of e.g. the pressure, the applied plasma power, the total feed gas flow and its composition. Additionally, the diagnostics were applied to a chemically similar plasma-assisted process for diamond deposition.

Resulting from this thesis are new insights into the practical application of an AS made of CFC, the plasma-chemistry involving hydrogen, nitrogen, and carbon, and the particular role of CO as an indicator for reactor contamination. The effect of the feed gas composition on the resulting nitrogen- and carbon-expanded austenite layers was proven by combination of *in-situ* laser absorption spectroscopy with post-treatment surface diagnostics. Furthermore this work marks the first use of frequency comb spectroscopy with sub-nominally resolved Michelson interferometry for investigation of a low-pressure molecular discharge. This way the rotational bands of multiple species were simultaneously measured, resulting in temperature information at a precision hitherto not reached in the field of nitrocarburizing plasmas.

Introduction

The subject of this thesis is the plasma-chemical analysis of nitrocarburizing plasmas with a solid carbon supply. Starting with chapter 1, the process of nitriding and nitrocarburizing is presented with a particular focus on the treatment of austenitic stainless steels. After a short introduction into the characteristics of this group of steels, a basic introduction to the effects of interstitially solved nitrogen and carbon on the surface characteristics is given. The chapter concludes with a short presentation of different methods of achieving nitrogen- and carbon-expanded layers.

Subsequently, chapter 2 focuses on the process of plasma nitrocarburizing, first by introducing the plasma state with regard to low temperature dc plasmas and plasma-surface interactions. Then the process of plasma-assisted nitrocarburizing is described, with typical industrial scale in mind. This includes the active screen plasma nitrocarburizing technology as a modern innovation in the field.

As the fundamentals for molecular spectroscopy, the molecular rovibrational band structure and energetic transitions are introduced in chapter 3, plasma diagnostics. Further, laser sources used in this thesis are discussed, concluding with the frequency comb. As a novel laser source, unique characteristics and detection schemes are discussed for the frequency comb in detail.

In chapter 4, an extensive study at an industrial-scale active screen nitrocarburizing reactor is presented in three sections. The first section describes a plasma-diagnostic investigation of plasma processes as a function of the total gas flow and pressure. Next, the second section is a combination study of *in-situ* plasma diagnostics and *ex-situ* material analysis to gain insights into the effects of the plasma condition on the treatment results. The chapter concludes with a plasma-diagnostic study of the effects of oxygen-containing admixtures on the plasma-chemical composition, as well as their effect on the concentrations of present species for the duration of a nitrocarburizing treatment.

Chapter 5 is a plasma-diagnostic study at a laboratory-scale reactor. It establishes the concentrations of a larger variety of species than the previous industrial-scale reactor, as functions of the applied power, pressure, and gas mixture. Of particular note is the determination of the carbon consumption rate by production rate of carbon-containing species, which was verified with measurement of the macroscopic weight loss of the carbon active screen.

A follow-up study is presented in chapter 6, by application of a frequency comb to measure the rotational and translational temperatures of multiple bands of the dominant molecular reaction products CH_4 , C_2H_2 , HCN , and NH_3 at the same laboratory-scale reactor. This way, a number of assumptions required in chapter 5, as well as the measured concentrations, were confirmed. However, more importantly this experimental study serves as a proof of concept for the application of the frequency comb for plasma studies of nitrocarburizing plasmas in particular and non-thermal plasmas in general.

One example of a plasma application of interest for frequency comb absorption spectroscopy is microwave plasma-assisted chemical vapour deposition of nanocrystalline diamond films with admixture of small amounts of nitrogen, a study thereof presented in chapter 7. In this study, conducted with conventional external-cavity quantum cascade lasers and lead-salt tuneable diode lasers, the increased complexity of the plasma-chemistry with admixed nitrogen is documented.

In chapter 8 the content of the thesis is subsequently summarized. This includes unified conclusions concerning the performance of an active screen made of carbon-fibre reinforced carbon both for the industrial- and laboratory-scale reactors presented in chapter 4 and 5. The proven effect of the plasma-chemical composition on the resulting nitrocarburized layers is noted. A short summary concerns the topic of temperature determination in plasmas, the benefit of frequency comb based spectroscopy therein, and the potential usefulness in applications such as chemical vapour deposition. The thesis closes with an outlook on ongoing progress in the research group related to plasma nitrocarburizing.

List of symbols and abbreviations

Table 1 List of constants

Symbol	Name	Value in SI units
h	Planck constant	$6.626 \cdot 10^{-34} \text{ J s}$
ϵ_0	Vacuum permittivity	$8.854 \cdot 10^{-12} \text{ As V}^{-1} \text{ m}^{-1}$
k_B	Boltzmann constant	$1.38066 \cdot 10^{-23} \text{ J K}^{-1}$
m_e	Electron mass	$9.10938 \cdot 10^{-31} \text{ kg}$
e	Elementary charge	$1.602176 \cdot 10^{-19} \text{ As}$
c	Speed of light	$2.99792 \cdot 10^8 \text{ m s}^{-1}$
N_A	Avogadro's constant	$6.022 \cdot 10^{23}$
e	Euler's number	2.71828
π	Pi, mathematical constant	3.14159

Table 2 List of symbols

Symbol	Physical quantity	Unit
p	Pressure	mbar
P	Plasma power	W
P_{AS}, P_{screen}	Plasma power at the active screen	W
P_{Bias}	Plasma power at the biased workload	W
R_C	Conversion efficiency	molecules J^{-1}
R_F	Fragmentation efficiency	molecules J^{-1}
S	Absorption line strength	$\text{cm}^{-1}/(\text{molecule cm}^{-2})$
T_{gas}	Gas temperature	K
T_{rot}	Rotational temperature	K
T_{vib}	Vibrational temperature	K
T_e	Electron temperature	K
T_{set}	Set temperature	K
κ_D	Degree of dissociation	%
f_{rep}	Repetition rate frequency	Hz or cm^{-1}
f_0	Carrier envelope offset frequency	Hz or cm^{-1}
f_{FTS}^0	Nominal resolution of a FTS	Hz or cm^{-1}
L	Optical path difference	m
λ	Wavelength	nm
ν	Wavenumber	cm^{-1}
n_e	Electron density	cm^{-3}
$[X]$	Absolute density of species X	cm^{-3}
Φ_X	Gas flow of precursor X	sccm or slh
Φ_{Total}	Total introduced gas flow	sccm or slh

Table 3 List of acronyms and abbreviations

Abbreviation	Meaning
AS	Active screen
ASPN	Active screen plasma nitriding
ASPNC	Active screen plasma nitrocarburizing
CCD	Charge-coupled device
CPN	Conventional plasma nitriding
cw	Continous wave
dc	Direct current
DFG	Difference frequency generation
EC-QCL	External-cavity quantum cascade laser
EC-QCLAS	External-cavity quantum cascade laser absorption spectroscopy
FC	Frequency comb
FTIR	Fourier-transform infrared spectroscopy
FTS	Fourier-transform spectrometer
GDOES	Glow discharge optical emission spectroscopy
ILS	Instrumental line shape
IRLAS	Infrared laser absorption spectroscopy
IRMA	Infrared multi-component acquisition system
MCT	Mercury cadmium telluride
MPC	Multipass cell
MPO	Multipass optic
MW-PACVD	Microwave plasma assisted chemical vapor deposition
NALM	Non-linear amplifying optical loop mirror
OES	Optical emission spectroscopy
OPD	Optical path difference
OPO	Optical parametric oscillator
PLANIMOR	Plasma nitriding monitoring reactor
TDL	Tunable diode laser
TDLAS	Tunable diode laser absorption spectroscopy
XRD	X-ray diffraction

1 Nitriding and nitrocarburizing

1.1 Definition and basic description

Iron, often in the alloyed form called steel, is the most widely used metal. In 2017, 1.69 billion tons of raw steel were produced globally, with the US Geological Survey projecting an increase to 1.8 billions in 2018. This widespread application of steel in every aspect of life is due to the versatile properties of different steel mixtures, while at the same time often being more affordable than alternative materials [1].

Steels rich in chromium typically are considered as part of the family of stainless steels, which due to their high corrosion resistance often are valued in specialized applications. Within this family, five subgroups can be identified:

- Martensitic alloys
- Ferritic alloys
- Austenitic alloys
- Duplex alloys
- Precipitation-hardening alloys

To reduce the complexity, this thesis solely focuses on austenitic stainless steels, representing the largest subgroup by production volume. They are identified by possessing a pure face-centred cubic (fcc) lattice structure, also called a pure γ -phase. However, like the other stainless steels, their characteristic corrosion resistance is derived from their high chromium content. Chromium forms an impermeable chromium oxide layer adherent to the alloy substrate, if in contact with an oxygen-containing environment. Thus, the layer is considered self-healing, if scratches or cracks are considered. However, for this process to take place the precipitation of chromium within the material has to be avoided. Since precipitation takes place above a material specific temperature threshold, a too high temperature during processing can result in a chromium depletion of the matrix and thus render the work piece prone to corrosion [2].

While stainless steels have a characteristically high resistance towards corrosion, their range of applications may be limited e.g. due to a too low resistance to abrasion and erosion, or their low surface hardness. Well-established methods of hardening by diffusive introduction of atomic nitrogen, carbon, or both into the surface are typically used to increase the tribological properties of work pieces and thus increase their range of application. These processes are called nitriding, carburizing, and nitrocarburizing, respectively.

The atomic nitrogen or carbon occupy interstitial positions within the fcc crystal structure, thus increasing the lattice parameter. For that reason, compressive stress is introduced, resulting in an enhancement of mechanical, tribological, and fatigue properties [3]. In fact, the lattice expansion can be diagnosed using x-ray diffraction spectroscopy (XRD) as first reported by Ichii in 1986 [4 – 6]. Figure 1.1 shows the XRD patterns of AISI 316 steel samples, with one plasmanitrided (PN) at 400 °C (670 K) for 15 hours, another plasmacarburized (PC) at 400 °C (670 K) for 10 hours, and one untreated control. The two marked features of untreated samples correspond to the (111) and (200) orientation of the γ -phase and appear shifted to lower diffraction angles for the carburized and nitrided sample. A smaller angle corresponds to a larger lattice parameter of the observed structure. Ichii named the newly discovered phase s-phase; accordingly, the corresponding features of the plasmanitrided and plasmacarburized samples were labelled S_N1 and S_N2 , and S_C1 and S_C2 , respectively. Nowadays, as the s-phase does not describe a distinctive crystallographic phase, the terms carbon- or nitrogen-expanded austenite are more common [8].

Eventually expanded austenite can be defined as "... a paraequilibrium phase originating in fcc crystalline structure with strong nitride and/or carbide alloying elements such as chromium and with

large amounts of nitrogen and/or carbon in solid solution. The base of the alloy can be iron, cobalt, or nickel.” [2] However, there is still an immense research interest into the nature and control of expanded austenite within the scientific community [9 – 12].

Comparing nitriding and carburizing, figure 1.1 already shows a less pronounced shift to lower diffraction angles in the case of carburizing, hence a reduced lattice expansion compared with nitriding. This agrees with the observation, that nitriding results in harder surfaces. Furthermore, the carbon-expanded austenite layer is observed at greater diffusion depth than the nitrogen-expanded austenite. Thus the combination treatment, introducing both carbon as well as nitrogen atoms into the work piece, typically results into a gradual change of hardness and a large diffusion zone considered beneficial for most applications. Figure 1.2 shows an etched cross section of a plasmanitrocarburized AISI 316L sample. As both expanded austenite layers are more resistant to corrosion than the unaffected bulk material, they appear light grey. Between the two types of expanded austenite, a slight change of hue can be distinguished due to the different chemical reactivity of both.

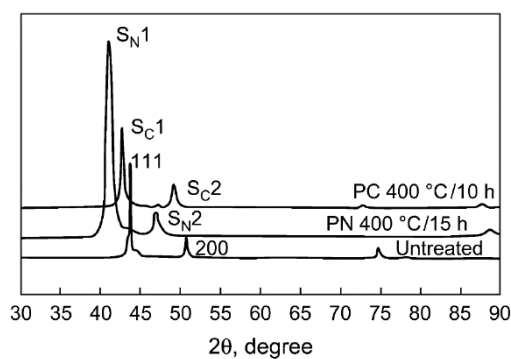


Figure 1.1 XRD patterns of plasmanitrided (PN), plasmacarburized (PC), and untreated AISI 316L samples. The marked features of the untreated sample correspond to the γ -phase. Modified from: [7]

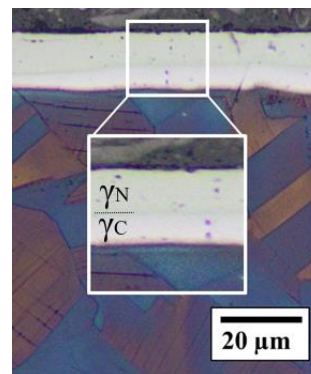


Figure 1.2 Etched cross section of a plasmanitrocarburized AISI 316L sample. The diffusion zone (in light grey) is divided into a nitrogen- and carbon-dominated s-phase, as indicated. Conditions: $t = 5h$, $T = 730 K$, $p = 3 mbar$, $P_{AS} = 5 kW$, $P_{Bias} = 1.25 kW$, $\Phi = 38 slh H_2 + 38 slh N_2 + 4 slh CH_4$. [13]

1.2 Methods and comparison

Within more than 100 years of research, the surface engineering community has developed a multitude of different techniques to optimize the result from nitriding, carburizing, and nitrocarburizing. This includes the development of specialized steel mixtures, pre- and post-treatment procedures as well as reactor designs based on different principles of operation. Some reactor designs and their principles of operation will be presented in this short overview, focused on nitriding. Still, most methods can also be applied to carburize or nitrocarburize, with only minor changes.

Modern **gas nitriding** is relatively close to the first implementations, in that the workload is exposed to a nitrogen-containing gas mixture at a high temperature [14]. The pressure is typically at 1 atmosphere, with the tightly controlled reactor temperature both providing thermal dissociation of the precursors as well as thermochemical diffusion at the surface of the workload. However, the chromium oxide layer presents a challenge, since it limits the diffusion of atomic nitrogen into the material. Conventionally this layer is removed pre-treatment, with methods such as “... dry honing, wet blasting, and pickling; chemical reduction in an appropriate atmosphere; submersion in molten salts; [or] sputtering ...” [2], with corresponding effort in resources and handling. Modern approaches instead include additional steps in the treatment and admixtures to chemically remove the barrier to diffusion, with some of the depassivation methods based on the presence of HCN or C_2H_2 [15 – 19].

Alternatively, **plasma nitriding** solves the problem by sputtering of the chromium oxide layer, thus removing it by ion bombardment. The process, which in some sources is also called ion nitriding, is conventionally conducted in a pulsed dc discharge maintained at low mbar pressure between the anodic reactor wall and the cathodic work piece. With a constant flow of nitrogen-containing precursor gas, reactive species are generated by the plasma, which are in turn able to diffuse into the plasma-heated workload. While this method of nitriding is requiring more equipment, such as a pulsed power supply and vacuum pumps, it is consuming less precursor gas and energy, compared with gas nitriding. As such, it is considered more environmental friendly. Even though it has found industrial applications, thermal inhomogeneity at the workload and resulting inhomogeneity of treatment progress along the diffusion interface is still a problem. Accordingly, the treatment of samples of different geometries is complicated and requires manual labour for precise placement of the work pieces within the reactor.

Consequently, further development resulted in the **active screen plasma nitriding** technology. It differs from conventional plasma nitriding by introducing an additional cathode into the reactor design. This active screen (AS) is placed between the now only weakly biased workload and the anodic reactor wall. As the reactive species and thermal radiation are generated by the high-powered plasma between the AS and the reactor wall, the cathodic bias applied to the work piece can be regulated to only account for the sputtering of the chromium oxide layer. However, this approach further complicates the electrical infrastructure of the reactor design and thus reduces the appeal for a broad industrial application.

Furthermore, alternative ionisation-based nitriding techniques have been reported, using radio-frequency or laser induced plasmas, ion-beams or high-power pulses to achieve the nitriding effect. However, apart from laboratory applications these methods have found little to no industrial use as of yet.

At last, table 1.1 shows a comparison of stainless steel nitriding (N), carburizing (C), and nitrocarburizing (NC) methods in terms of their process parameters [2].

Table 1.1 Comparison of stainless steel nitriding, carburizing, and nitrocarburizing methods in terms of their process parameters, sourced from [2].

Characteristic	Gaseous	Conventional plasma	Active screen plasma
<i>Temperature [K]</i>	700 – 720	620 – 720	620 – 720
<i>Treatment duration [h]</i>	4 – 22	5 – 20	5 – 20
<i>Potential [V]</i>	--	400 – 1000	400 – 100
<i>Hardness [HV]</i>	N: 1200 C: 800 NC: 1350	N: 1300 – 1500 C: 700 – 1000 NC: 1500	1100 – 1300
<i>Layer thickness [µm]</i>	N: 17 (3-5 h) C: 15 (22 h) NC: 10 (9 h)	N: 2 – 20 C: 5 – 40	2 – 20
<i>Used gases</i>	NH ₃ , N ₂ , H ₂ , C ₂ H ₂	N: N ₂ , H ₂ CN: N ₂ , H ₂ , CH ₄	N: N ₂ , H ₂
<i>Gas pressure [mbar]</i>	1013	1 – 10	1 – 10
<i>Consumables cost</i>	Medium	Low	Medium

References

- [1] Mineral commodity summaries, U.S. Geological survey, 28th February 2019
- [2] Casteletti L C, Neto A L, and Totten G E 2014 *Metallogr. Microstruct. Anal.* **3** 477-508
- [3] Pye D 2003. In: *Practical nitriding and ferritic nitrocarburizing*. Ed. D. Pye, ASM International
- [4] Zhang Z L and Bell T 1985 *Surf. Eng.* **1** 131-136
- [5] Ichii K., Fujimura K, and Takase T 1986 *Technol. Rep. Kansai Univ.* **27** 135-144
- [6] Buhagiar J 2010 *Surf. Eng.* **26:4** 229-232
- [7] Bell T 2002 *Surf. Eng.* **18:6** 415-422
- [8] Christiansen T, Hummelshøj T S, and Somers C 2010 *Surf. Eng.* **26:4** 242-246
- [9] Balogh-Michels Z *et al.* 2017 *J. Appl. Phys.* **122** 025111
- [10] Brink B K *et al.* 2017 *Scr. Mater.* **131** 59-62
- [11] Tao X *et al.* 2019 *Acta Mater.* **164** 60-75
- [12] Czerwicz T *et al.* 2019 *J. Alloys Compd.* **811** 151972
- [13] Private communication with Saeed Jafapour (26.01.2020)
- [14] Machlet A 1913 *US Patent Specification* 1,092,925
- [15] Tahara M 1993 *EU Patent Specification* 0588458
- [16] Williams P C 1998 *US Patent Specification* 6165597A
- [17] Hoshino K 2005 *EU Patent Specification* 1707646 B1
- [18] Minemura K 2005 *EU Patent Specification* 1712658 A1
- [19] Christiansen T J 2011 *Intern. Patent Specification* 2011/009463 A1

2 Plasma nitrocarburizing

2.1 Definition of the plasma state

This chapter serves to define the plasma state and introduce key parameters of a plasma. Later on, plasma properties required for comprehension of this thesis will be given. For a deeper understanding and derivation of the formulas, references are provided.

In the simplest possible terms, a plasma is an ionized gas that shows collective behaviour and is quasi-neutral, i.e. is neutral if contained charges are integrated over sufficiently large volumes. Firstly, a plasma will only show collective behaviour once a sufficient level of ionization is provided. Therefore, the degree of ionization κ_i is defined as:

$$\kappa_i = \frac{n_e}{n_e + n_n} \quad , \quad (2.1)$$

with the electron density n_e and n_n being the density of the neutral species. Secondly, a characteristic length scale for the quasi-neutrality of a plasma, called Debye length λ_D , can be derived as:

$$\lambda_D = \sqrt{\frac{\varepsilon_0 \cdot k_B \cdot T_e}{n_e \cdot e^2}} \quad , \quad (2.2)$$

where ε_0 is the vacuum permittivity, k_B is the Boltzmann constant, T_e is the electron temperature, and e is the elementary charge [1]. Implicitly equation (2.2) assumes that the local permittivity ε can be approximated with the vacuum permittivity ε_0 and the electron mobility is much larger than the ion mobility, both of which hold true for a large range of applications. While the condition of quasi-neutrality relates the electron density and the ion density n_i of all species k with a charge of Z_k according to:

$$n_e - \sum_k Z_k \cdot n_{i,k} = 0 \quad , \quad (2.3)$$

the temperatures of electrons, ionic species, and neutral species can vary greatly. This allows to differentiate thermal and non-thermal plasmas, by whether or not the plasma is in a thermal equilibrium between all present species. Plasmas observed in this work are non-thermal plasmas; accordingly, differences between temperatures of different species have to be taken into account.

When laboratory and industrial discharges are concerned, the border regions of the plasma with a surface differ in their characteristics from the plasma bulk. The region is called the sheath, with further distinction drawn between the sheath and the presheath [2]. As electrons collide with the wall, their charge is removed from the plasma, decreasing the local plasma potential until the potential of the wall has been matched at the interface. Positive ions, relatively immobile compared to electrons due to their high mass, maintain this potential and thermal electrons are trapped by the potential well. At this point figure 2.1 illustrates the distribution of electron and ion densities as well as the potential near a wall. In the sheath, the condition of quasi-neutrality described by equation (2.3) is broken, as it possesses a net positive charge. Furthermore, figure 2.1 shows the presheath, which is a zone of quasi-neutrality defined by its decrease of charge carrier density and plasma potential. Typically, the sheath and presheath range up to several Debye lengths from the surface.

In this work, the plasma-surface interactions are of importance. For example, plasma nitriding reactors are often based on a low-pressure dc discharge, where the Townsend breakdown mechanism applies. The resulting threshold condition for a self-sustaining dc discharge can be given as:

$$\gamma \cdot [\exp(\alpha \cdot d) - 1] = 1 \quad , \quad (2.4)$$

where γ is the secondary electron emission coefficient of the cathode, α is the Townsend ionization coefficient, and d the distance between the electrode. Hereby, α is a function of the electric field strength E and gas properties, and γ of the surface material and structure, e.g. roughness. Thus, consideration of

gas and surface properties become necessary. This includes erosion of the cathode through ion-bombardment or heat- or chemically-induced processes.

Furthermore, in particular at low pressures in molecular discharges, plasma-chemical reactions involving the surface become relevant. This is in addition to any catalytic effect the surface may have for the process chemistry.

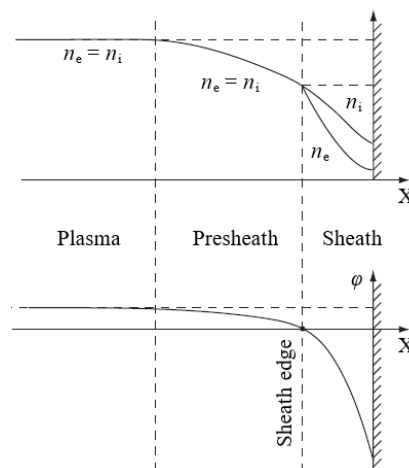


Figure 2.3 Distribution of electron and ion densities (upper part) and potential (lower part) in the sheath and the presheath near the wall. Modified from [2].

2.2 Conventional plasma nitrocarburizing

Nowadays, conventional plasmanocarburizing (CPNC) reactors in sizes ranging from about 0.035 to 32 m³ in volume are commonly available in industry [3, 4, 5]. Figure 2.2 shows a schematic side-view of a CPNC reactor in operation at a few mbar of pressure with the cathodic glow region of the discharge marked in purple. The reactor wall represents the grounded anode of the discharge and has to facilitate gas and electrical throughput, as well as ease of access to the workload between treatments. Furthermore, a window is often incorporated for visual confirmation of a full plasma coverage at the workload [7]. The process gas is typically fed-in through a gas shower positioned opposite to the connection of the vacuum pump, to allow for a complete circulation of the reactor volume.

As current industry-standard, a pulse-modulated negative voltage is applied to the workload, thus forming the cathode of the discharge. In this way, the temperature at the workload can be controlled with the additional parameter of the pulse duty-cycle. Furthermore, the risk of arcing is reduced. Chapter 1 already underlined the importance of temperature for the thermochemical diffusive process and the phase stability; accordingly, the workload temperature is typically measured with e.g. thermocouples and used for regulation of the discharge power. With respect to temperature control, ohmic heaters can be installed into the reactor wall and allow for an additional parameter for temperature control. Reactors of this type are called warm-wall reactors.

However, applying a high cathodic potential to too narrow geometries or even corner and edges, can cause an enhancement of the electrical field, resulting in high localized currents and thus an increase in temperature. This effect, known as edge effect, results in erosion rings due to nitride formation [9].

Figure 2.3 shows the placement of the workload designated for plasma nitrocarburizing. Firstly, the samples are distributed with large distances between them, to avoid thermal hotspots caused by the hollow cathode effect. This effect, caused by the overlap of cathodic glow regions, generates high-energy electrons and additional photo-ionization, resulting in high local currents and thus local

hotspots [2]. Secondly, conical support points elevate the workload. This way, the discharge can cover the whole surface area of the work piece and nitrocarburize it homogenously. Currently, the time, manpower, and experience necessary for manual placement of the work pieces are still a limiting factor for the widespread application of plasma nitrocarburizing.

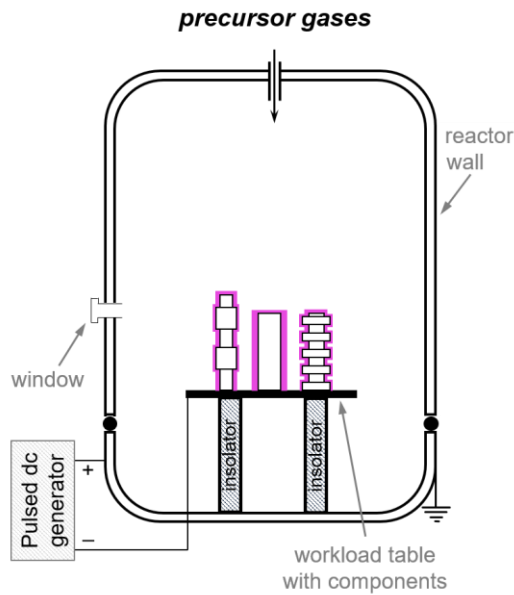


Figure 2.2 Schematic side-view of an operating CPNC reactor with the vacuum system omitted. Modified from [6].

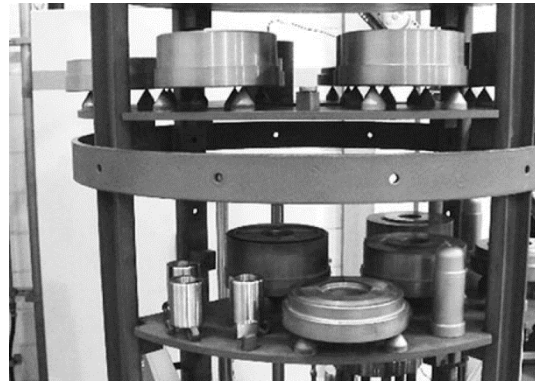


Figure 2.3 Example of workload placement with use of support points. Modified from [8].

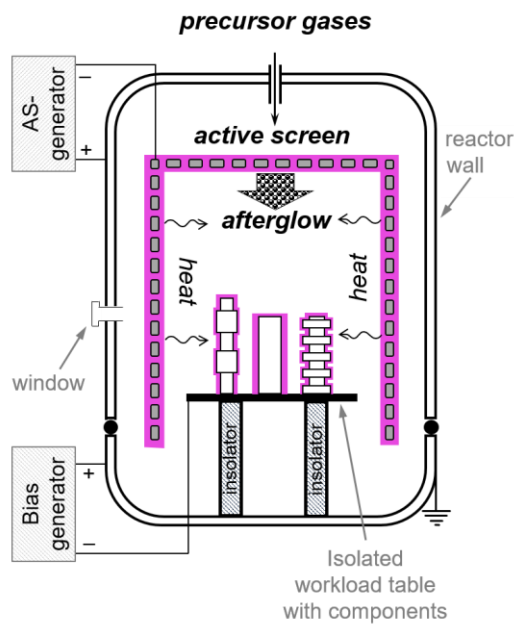


Figure 2.4 Schematic side-view of an operating ASPNC reactor with the vacuum system omitted. Modified from [6].

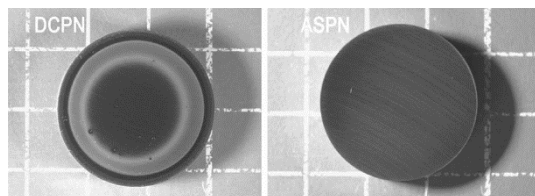


Figure 2.5 Typical appearance of conventional (left) and AS (right) plasmanitrided samples. Damages due to sputtering and the edge effect are clearly visible on the conventionally treated sample. From [11].

2.3 Active screen plasma nitrocarburizing

Figure 2.4 shows the main technological innovation of the active screen (AS) plasma nitrocarburizing technology, as in the schematic side-view an additional cathode can be seen. This AS is placed between the cathodic workload and the grounded reactor wall. Two cathodic glow seams are depicted, one covering the AS, the second covering the work pieces. As only a small dc bias voltage is applied to the workload, the plasma power at the work pieces is lower and serves to sputter the chromium oxide layer. It is also referred to as bias plasma. Heat and reactive species are provided by the more powerful pulsed dc discharge at the AS, alternatively called AS plasma. This principle is known as nitriding in the afterglow, as the work pieces are positioned within the flowing afterglow of the AS plasma.

The use of an AS eliminates or reduces some of the problems associated with a strong cathodic voltage at the workload, such as arcing and thermal inhomogeneity. However, for industrial nitrocarburizing of most steels, a bias to the workload is still required for a sufficient treatment result [9]. This is one of the major limits for a wider application of this technology, as even a low-power bias plasma causes a large requirement of manual placing of the work pieces.

Finally, the ASPNC technology not only decouples heat production from the controlled sputtering of the workload surface, but also introduces a new material interface into the reactor. One mechanism assumed responsible for nitriding in CPNC and ASPNC reactors was the sputtering of iron, which in turn form iron nitride in the plasma, reabsorb on the diffusion interface, and thus introduce atomic nitrogen for the thermos-chemical diffusion process [6]. However, a recent study conducted by Hubbard *et al.* showed that, the influence of this mechanism on the total atomic nitrogen introduced is not significant [10]. Other groups investigated co-alloys to the steel AS, e.g. aluminium and silver, to produce antimicrobial surfaces on the workload [12, 13].

In order to substitute carbon-containing gaseous admixtures to the feed gas, an AS can serve as a plasma-chemical source of carbon in the process, as first proposed by Lebrun *et al.* and first realised by Crespi *et al.* for a different plasma-assisted process [14, 15]. The first use as an AS in an ASPNC process was reported in 2017 by Burlacov *et al.* and Hamann *et al.*, in joint investigations of industrial- and laboratory-scale reactors [16, 17]. Furthermore, the authors reported drastically increased concentrations of HCN and C₂H₂ resulting from the use of a CFC AS as a substitute for a steel AS with CH₄ admixture. Already in the early 1990s, the highly reactive HCN molecule was linked with beneficial diffusion conditions [18, 19]. In addition, recent patents related to low-temperature gas nitriding propose the admixture of C₂H₂ or other carbon-containing compounds, which form HCN or may form HCN in a nitrogen-containing environment [20 – 23]. Accordingly, Burlacov *et al.* identified the concentrations of HCN as a control parameter for the carburizing potential of the nitrocarburizing process for ASPNC with a CFC AS [24].

References

- [1] Chen F F and Chang J P (eds) 2003 *Lecture Notes on Principles of Plasma Processing* (Springer US) ISBN 978-0-306-47497-2 DOI 10.1007/978-1-4615-0181-7
- [2] Friedman A 2008 *Plasma chemistry* (Cambridge University Press) ISBN 98-0-521-84735-3
- [3] rubig.com/anlagentechnik/plasmanitrieranlage-micropulsr-everest/, Rübige GmbH & Co KG, queried 01.02.2020
- [4] eltropuls.de/plasmanitrieranlagen/, Eltro GmbH, queried 01.02.2020
- [5] pvatepla-ivs.com/produkte/plasma-nitrieranlagen/, PVA Industrial Vacuum Systems GmbH, queried 01.02.2020
- [6] Dalke A. *et al.* 2019 *Surf. Coat. Technol.* **357** 1060-1068
- [7] Pye D 2003. In: *Practical nitriding and ferritic nitrocarburizing*. Ed. D. Pye, ASM International
- [8] Casteletti L C, Neto A L, and Totten G E 2014 *Metallogr. Microstruct. Anal.* 3:477-508
- [9] Olzon-Dionysio M *et al.* 2010 *Surf. Coat. Technol.* **204** 3623-3628
- [10] Hubbard P *et al.* 2006 *Surf. Eng.* **22** 243-247
- [11] Gallo S C and Dong H 2009 *Surf. Coat. Technol.* **203** 3669-3675
- [12] Naeem M *et al.* 2017 *Mater. Lett.* **189** 213
- [13] Dong Y *et al.* 2011 *Acta Biomaterialia* **7** 447
- [14] Lebrun J P 2000 *US Patent Specification* 7,074,460 B2 18.04
- [15] Crespi A E *et al.* 2011 *Mater. Lett.* **65** 2985-2988
- [16] Burlacov I *et al.* 2017 *HTM J. Heat Treat. Mat.* 72 254
- [17] Hamann S *et al.* 2017 *J. Appl. Phys.* **121** 153301
- [18] Sproge L and Slycke J 1992 *J. Heat Treat.* **9** 105-112
- [19] Lebrun J P 1996 *EU Patent Specification* 0801142 B1 12.04
- [20] Hoshino K 2005 *EU Patent Specification* 1707646 B1
- [21] Minemura K 2005 *EU Patent Specification* 1712658 A1
- [22] Christiansen T J 2006 *Intern. Patent Specification* 2006/136166 A1
- [23] Christiansen T J 2011 *Intern. Patent Specification* 2011/009463 A1
- [24] Burlacov I *et al.* 2018 *J. Appl. Phys.* **123** 233302

3 Plasma diagnostics

Diagnostics can be classified in *in-situ* and *ex-situ*, invasive and non-invasive, and furthermore qualified by their resolution, e.g. in spatial or temporal aspects. *In-situ* measurements are such, which probe the conditions of the process in its locality. Invasive measurements are such, which may affect the measurement result by disturbance of the process. With respects to their application, additional concerns need to be addressed, e.g. the avoidance of sources of uncertainty and the relevance of the gathered information.

As the plasma state covers a wide range of variables, a large set of methods and techniques have been developed to address them [1]. However, this thesis will be restricted to the diagnostics applied to plasma nitrocarburizing and will further detail those applied within the framework of this thesis.

Previous diagnostic effort on nitrocarburizing plasmas was based on *in-situ* optical emission spectroscopy (OES) to measure relative concentrations and temperatures of electronically excited atomic and molecular species [2 – 7]. To a lesser degree, *ex-situ* mass spectroscopy and particle energy analysis were applied, providing relative concentrations and kinetic energies of atomic and molecular species [8 – 11]. In addition, some studies conducted *in-situ* invasive probe measurements to gather information on the electron energy distribution function and the plasma potential [12, 13]. Eventually starting in 2012, *in-situ* and *ex-situ* laser absorption spectroscopic (LAS) studies were published, including absolute concentrations and temperatures of molecular species [7, 10, 14 – 23].

3.1 Introduction into molecular spectroscopy

Molecules are composite particles, formed by electronically bound atoms. Similar to atoms, the complex system of states that describe a molecule can be given by the notation of quantum numbers. Some of the quantum numbers are associated with classical concepts, such as the electronic, vibrational, and rotational quantum numbers. However, the application of the classical viewpoint on aspects of the quantum numbers, in particular on interactions of molecules with photons, is limited. Therefore, this introduction will be focused on energetic aspects.

Figure 3.1 depicts a simple scheme of energetic levels associated with the molecular states, with indicated transitions due to photon-absorption. Two electrical states A (upper half) and B (lower half) are shown with five vibrational states (long horizontal lines) each. Furthermore, each vibrational level has several rotational sublevels (short horizontal lines). The transitions are differentiated between electronic transitions, if the electronic quantum number is changed, and rovibrational transitions, if the electronic quantum numbers remains unaffected. Furthermore, the change of the rotational quantum number J relates to the classification as P-, Q-, or R-branch of the rovibrational transition: P-branch transitions decrease the value of J , Q-branch transitions maintain the value of J , and R-branch transitions increase the value of J . The energetic difference between the lower level energy E'' and the upper level energy E' corresponds to the wavelength of the absorbed photon according to

$$\frac{h \cdot c}{\lambda} = h \cdot c \cdot \nu = h \cdot f = E' - E'' \quad . \quad (3.1)$$

Therein, λ is the wavelength, ν is the wavenumber, and f is the frequency of the absorbed photon. Furthermore the Planck constant h and the speed of light c are used. Equation (3.1) is also valid for the emission of a photon.

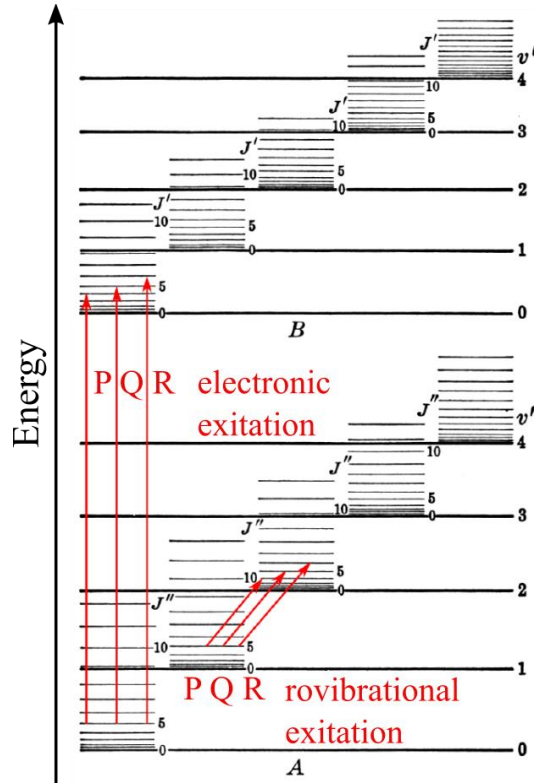


Figure 3.4 Schematic of energetic levels of molecular states. Indicated in red are transitions that correspond to electronic and rovibrational excitations. Modified from [24, 25].

Assuming a population N_2 in an upper energy level state 2 and a population N_1 in a lower energy level state 1 exist, the photon-induced transition between the two populations can be facilitated in three ways:

- **Spontaneous emission**, described by

$$\frac{dN_{21}}{dt} = A_{21} \cdot N_2 \quad (3.2)$$

- **Stimulated absorption**, described by

$$\frac{dN_{12}}{dt} = B_{12} \cdot u(\lambda) \cdot N_1 \quad (3.3)$$

- **Stimulated emission**, described by

$$\frac{dN_{21}}{dt} = B_{21} \cdot u(\lambda) \cdot N_2 \quad (3.4)$$

Equations (3.2 – 3.4) introduce the Einstein coefficients A_{21} , B_{12} , and B_{21} for spontaneous emission, stimulated absorption, and stimulated emission, respectively. Furthermore, the radiation density $u(\lambda)$ is used for stimulated interactions. In this way, the number of transition dN_{XY} in the infinitesimal timeframe dt is determined. Besides the presented photon-induced transitions, other processes such as quenching and collisional excitation may have an influence on the population density distribution in nitrocarburizing conditions [26]. However, they will not be discussed within this thesis.

The correlation between the Einstein coefficients can be given as

$$\frac{\lambda^3}{8\pi h} A_{21} = B_{21} = \frac{g_1}{g_2} B_{12} \quad , \quad (3.5)$$

with g_2 and g_1 being the multiplicities of degeneracy of state 2 and 1, respectively. Accordingly, the definition of the spectral line intensity of a rovibrational transition S_{ij} used by the HITRAN database can be introduced as

$$S_{ij} = I_a \frac{A_{ij}}{8\pi c \nu_{ij}^2} \frac{g_2 \cdot e^{\frac{-h \cdot c \cdot E_1}{T \cdot k_B}} \cdot (1 - e^{\frac{-h \cdot c \cdot \nu_{ij}}{T \cdot k_B}})}{Q(T)} . \quad (3.6)$$

I_a denotes the terrestrial isotopic abundance of the molecule, T the rotational temperature, and Q the temperature-dependent total internal partition sum [27]. The spectral line intensity is often referred to as the line strength.

3.2 Laser absorption spectroscopy

This thesis is in large part based on scientific insights gathered with LAS in the mid-infrared. Firstly, the term laser is assumed to be common knowledge with its wide ranging applications in science, industry, and everyday life. On that topic, the working fundamental principles of operation, e.g. state-inversion and stimulated emission, and lists of available types of lasers can be found in physics textbooks.

In LAS measurements, a laser of intensity I_0 at a wavenumber of ν is passing a sample volume of length L . The loss of intensity follows an exponential decay described by the Beer-Lambert law, wherein the line strength S_{ij} is a cross section for absorption of a molecule with an absolute concentration n within the sample. Finally, by integration along the distance L and the wavenumber range, an integral form can be derived:

$$\int_{-\infty}^{\infty} \ln\left(\frac{I_0}{I}\right) d\nu = S_{ij} \cdot L \cdot n \quad (3.7)$$

The left-hand side of the equation is called the integrated absorbance. Furthermore, the value of n is line-averaged along the beam, thus limiting spatial resolution in one direction.

Given the above facts, figure 3.2 illustrates the application of equation (3.7) with the simulated absorption spectrum of CH₄ at room temperature and 1 mbar of pressure. The dominant feature has a centre wavelength of $\nu = 1356.597 \text{ cm}^{-1}$.

Furthermore, the inset of figure 3.2 shows the simulated transmittance at different pressures $p = 1, 5, 20,$ and 100 mbar . The integral of the normalized intensity, sometimes referred to by the concept of equivalent width, is pressure invariant, although a broadening of the line profile with increasing pressure can be observed [28]. This effect is caused by the frequency of collisions increasing due to an increased gas pressure, thus called pressure or collisional broadening. Additionally, the gas temperature causes a broadening of the natural linewidth, often referred to as Doppler broadening. Those two main broadening mechanisms are typically associated with a Gaussian distribution for the Doppler broadening and a Lorentzian distribution for the pressure broadening, resulting in a Voigt profile as the convolution of both. However, models that are more sophisticated exist for specialized research [29 – 31].

The spectral range of LAS is a limiting factor to the type and number of molecules, as well as the states of said molecules that can be probed. Conventional laser sources used in this thesis will be presented in the following sections.

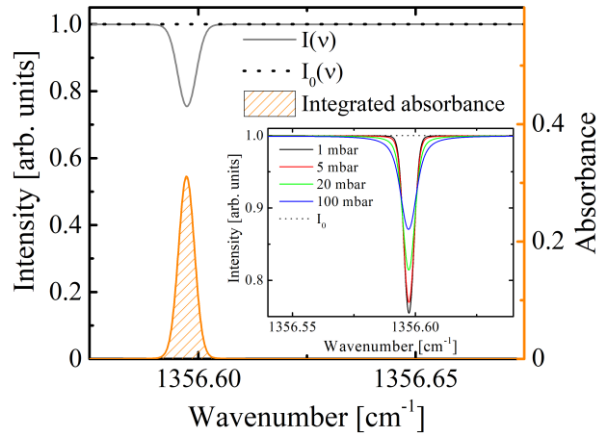


Figure 3.2 Simulated transmission spectrum of CH_4 (black) at $T = 300 \text{ K}$ and $p = 1 \text{ mbar}$, with the integrated absorbance (orange) as a function of the wavenumber. Inset, the transmission spectrum at $p = 1, 5, 20,$ and 100 mbar .

3.2.1 Lead-salt laser sources

Lead salts, such as PbS , PbTe , and PbSe , are semiconducting materials of the IV-VI group, with applications in infrared detectors and diode lasers. For the production of laser radiation, a layered structure as shown in figure 3.3 a) is used. Therein the photo-emitting lead-salt homo- or heterostructure is embedded between two oppositely doped claddings, one of which can be the substrate. The state-inversion is provided by electronic pumping, by applying a voltage between the two indicated contacts. Furthermore, the laser cavity is shown in figure 3.3 b), formed by the reflectivity r_1 and r_2 of the polished front and back crystal facet. The outcoupled emission is indicated in figure 3.3 a). An example of a packaged lead-salt tuneable diode laser (TDL) is depicted in figure 3.4 with a metric scale. The diode in figure 3.3 is a black crystal mounted between the grey ceramic and grey wire in figure 3.4.

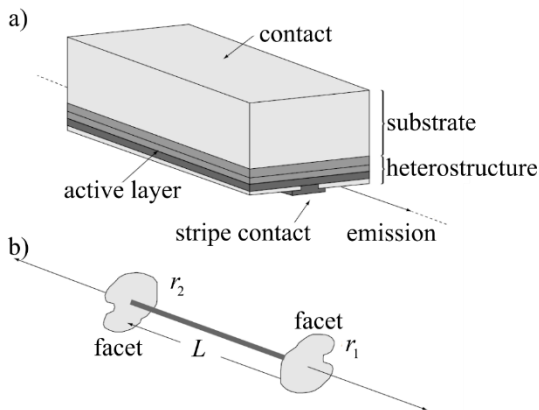


Figure 3.3 Schematic of a lead-salt laser (a) and a schematic of the laser resonator formed by the two polished facets (b). The reflectivities of the cavity mirrors r_1 and r_2 , and the cavity length L are indicated. Modified from [32].

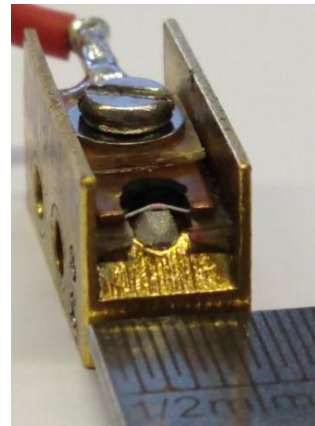


Figure 3.4 Photograph of a packaged tuneable lead-salt diode laser with a metric scale. The diode is mounted between a grey wire and a grey ceramic, located approximately in the centre of the figure.

Concerning laser diodes based on more common semiconductor materials of the III-V group, such as GaAs , the band shape of lead-salts results in a dramatic reduction of the non-radiative recombination of carriers via the Auger effect [32]. As the effect scales with the inverse of the band gap and thus with the wavelength of the emitted radiation, lead-salt lasers can maintain a population-inversion at lower wavenumbers, rendering them uniquely viable below 1000 cm^{-1} . For that matter, figure 3.5 shows the maximum temperatures of continuous-wave (cw) operation for IV-VI laser diodes as well as some other solid-state laser types, as a function of the wavenumber of the emitted radiation.

Concerning their operation, lead-salt TDLs are able to cover up to 100 cm^{-1} by variation of their operational temperature and laser current. Tuning, typically by application of a voltage ramp, can span up to 1 cm^{-1} , which enables the measurement of absorption lines at atmospheric pressure.

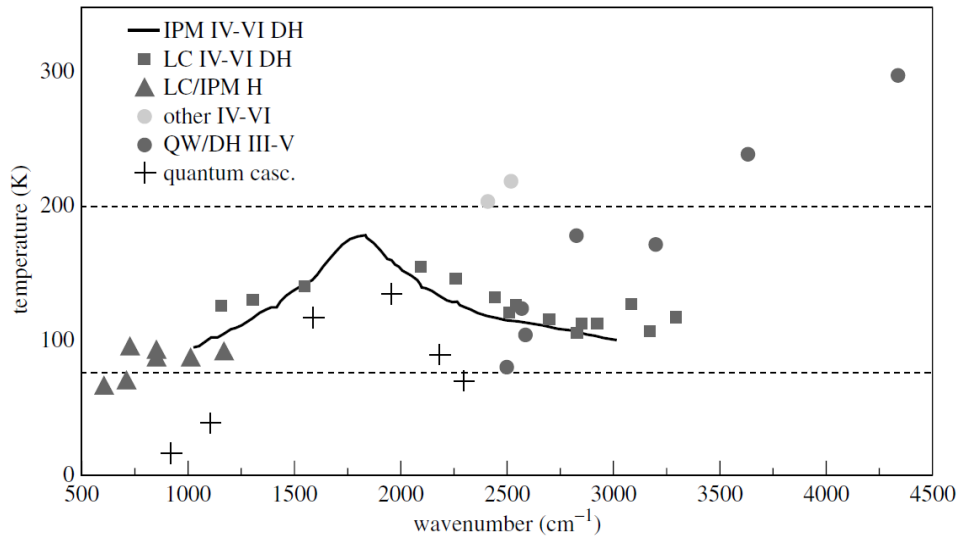


Figure 3.5 Comparison of maximum temperature of cw operation of double heterostructure (HD) or homostructure (H) type IV-VI laser sources with type III-V and quantum cascade lasers as a function of wavenumber. Some laser sources were manufactured by the Fraunhofer Institute for Physical Measurement Techniques (IPM) or Laser Components Company (LC). Published in 1999 [33].

Besides the low operational temperature indicated by figure 3.5, lead-salt diode lasers only permit low power emission up to a few mW. Moreover the emitted radiation is often multimodal, thus the power output is further reduced once a single mode has been selected by use of e.g. a grating. In the years since the publication of figure 3.5, developments in research and industry have resulted in interband cascade lasers (ICL) and quantum cascade lasers (QCL) that cover large parts of the shown wavenumber range. For example, commercially available external-cavity quantum cascade lasers (EC-QCL) operated at room temperature nowadays provide up to several hundred mW of single-mode cw radiation with combined coverage from $1000\text{ to }3000\text{ cm}^{-1}$ [34].

In this thesis, the infrared multi-component acquisition system (IRMA) was used as a logistical and optical framework for up to four individual TDLs, providing cryogenic cooling, control of the laser parameters, combining and shaping of the radiation, and acquisition of the signal. The system is described in detail elsewhere [35].

3.2.2 Quantum cascade laser sources

With further research into the band-structure of materials and improved control of nm layer deposition in laboratory and industrial applications, more complex heterostructures became viable. This development, sometimes referred to as band structure engineering as the band structure of the heterostructure can be precisely managed, resulted in the quantum cascade laser (QCL) [36].

Figure 3.6 shows the conduction band energy diagram of the periodically repeating layered structure during operation [36]. In the active region, the moduli squared wave functions of three electronic states are shown. An energetic electron is injected from the ground state of a neighbouring region, described as digitally graded alloy within the figure, into the excited state 3 of the first quantum well of the active zone. The electron relaxes to the excited state 2 while tunnelling through the potential barrier into the second well. A third relaxation into the lowest state 1 associated with a second tunnelling process completes the process by preventing thermalization between state 2 and 3, as with any three-level-system in laser theory. Continuing, the electron passes to the next digitally graded alloy, from where it

can be injected into the next active zone, thus enabling the cascade. However, for the propagation from one active zone to another the energy of level 1 needs to be higher than the excited state 3 of the succeeding active zone. This is provided by applying a voltage perpendicular to the layer plane. The laser cavity is formed by the polished facets of the heterostructure, in similarity to TDLs.

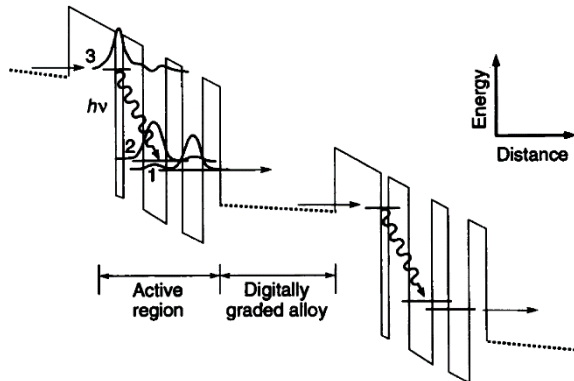


Figure 3.6 Conduction band energy diagram of a QCL. Two active regions are shown, once with the moduli squared wave functions of the relevant energetic states. The photon-emitting transition is indicated. A voltage is applied to generate the staircase shape. From [36].

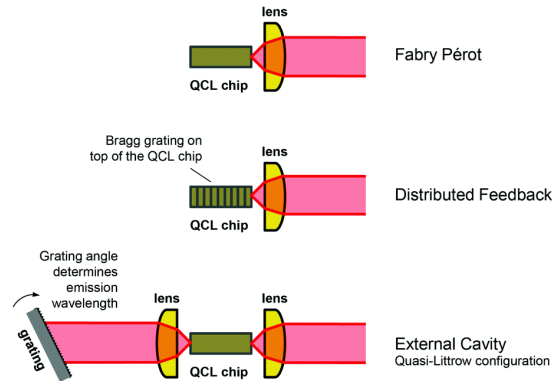


Figure 3.7 Overview of QCL configurations. The laser output is to the right. From [37].

Even though the QCL can be tailored to a specific wavelength by control of the layer thickness within the stack and the cw power of its emission ranges in the hundreds of mW, it is limited in the tuneable range to about 10 cm^{-1} and the emission can be multimodal due to its resonator design. For that reason alternative resonator designs were developed, the three most common of which are depicted in figure 3.7. The distributed feedback QCL (DFB-QCL) integrates a Bragg grating into the waveguide of the heterostructure, thus selecting a single wavelength to be emitted. Accordingly, the radiation is monomodal albeit limited tuneable. Alternatively, an external cavity can be formed by a variable-angled grating, which couples the radiation back into the gain zone. This external-cavity QCL (EC-QCL) allows for a wavelength selection during operation and is presented in figure 3.7 in a simplified Littrow configuration. Tuning ranges of more than 100 cm^{-1} are common for EC-QCL devices.

Regarding the commercially available EC-QCLs used in this thesis, three options of tuning are available:

- Coarse tuning using a stepping motor
- Low-frequency tuning using a piezo-electric actuator
- High-frequency tuning using current modulation

The presented EC-QCLAS data was acquired in spectral windows of about 1 cm^{-1} width by tuning the piezo-electric actuator with a sinusoidal function at 80 Hz frequency. Additional adjustments, by application of an offset to the driving signal, shifted the window. Furthermore, for the shift to other spectral regions of interest, the manufacturer-calibrated stepping motor was used.

3.3 Fourier-transform spectroscopy

Fourier-transform infrared spectroscopy (FTIR) is a broad-band absorption technique that offers multi-component detection with a self-calibrated wavenumber axis. Figure 3.8 schematically shows a Michelson interferometer, upon which many interferometers are based upon [38]. A beam is emitted by the source and split into two arms by the beamsplitter. Two mirrors, one moveable and one fixed, revert the propagation and are adjusted for maximum overlap between the reflexions of both arms, resulting in an interference recorded by the detector. Finally, the interferogram, i.e. the interference signal as a

function of the optical path difference (OPD) Δ , is measured. The second overlap of both reflexions is directed towards the source and ignored in many applications. Typically, a frequency-stabilized cw laser with a corresponding detector is arranged in a parallel setup using the same mirrors, as a reference for calibration of the OPD.

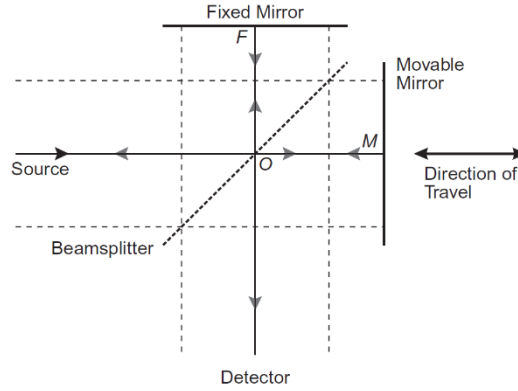


Figure 3.8 Schematic of a Michelson interferometer, with the median ray (solid line) and the two extremes of the collimated beam (dashed lines). The two arms are marked by an F and an M for the fixed and the moveable mirror, respectively. From [38].

For conventional FTIR spectroscopy incoherent continuum sources, e.g. global sources are used. Then the detected interferogram $I(\Delta)$ can be expressed as

$$I(\Delta) = \int_{-\infty}^{\infty} B(\nu) \cdot \cos(2\pi \cdot \nu \cdot \Delta) d\nu \quad , \quad (3.8)$$

where $B(\nu)$ is the wavenumber-dependent intensity, i.e. spectrum of the source [38]. Analytically the spectrum can be derived with the Fourier transform as

$$B(\nu) = \int_{-\infty}^{\infty} I(\Delta) \cdot \cos(2\pi \cdot \nu \cdot \Delta) d\Delta \quad . \quad (3.9)$$

With regard to application, most Fourier transforms are performed by the fast Fourier transform (FFT) routine, with the acquired interferogram $I(\Delta)$ being limited in both range and sampling rate [38]. The spectrum is given by

$$B(\nu) = A \cdot \text{abs}[\text{FFT}(I(\Delta))] \quad , \quad (3.10)$$

with A being an instrumentation factor, which can be omitted by normalization in absorption spectroscopy [39]. The sampling rate f_s is commonly linked to the wavelength λ_{Ref} of the reference laser according to

$$f_s = \frac{\lambda_{\text{Ref}}}{q} \quad , \quad (3.11)$$

where q is an integer, to accommodate the Nyquist theorem. Finally, the maximum OPD Δ_{max} is a limiting factor to the resolution of the spectrum, due to truncation of the infinite integral shown in equation (3.9). Assuming a boxcar profile of the acquired data, the resulting instrumental lineshape (ILS) function g_{ILS} has the form of

$$g_{\text{ILS}}(\nu, \nu_0) = \frac{\Delta_{\text{max}}}{c} \frac{\sin[\pi \cdot (\nu - \nu_0) \cdot \frac{\Delta_{\text{max}}}{c}]}{\pi \cdot (\nu - \nu_0) \cdot \frac{\Delta_{\text{max}}}{c}} \quad . \quad (3.12)$$

Thereby ν_0 is the centre frequency of the ILS function [39]. The latter fraction corresponds to the sinc of the argument of the sinus function. This ILS function limits the resolution of a FTIR setup, resulting in a spectrometer's nominal resolution of $1/\Delta_{\text{max}}$ [38, 40].

Regarding the use of FTIR in low pressure plasma applications, the increase of the maximum OPD will decrease the nominal resolution but on the other hand increase the acquisition time. For that reason, FTIR measurements in plasma nitrocarburizing are limited to qualitative overview spectra, in one reported study *ex-situ* [12].

3.4 Frequency comb spectroscopy

Frequency comb spectroscopy, also referred to as direct frequency comb spectroscopy or broad-band spectroscopy with frequency combs, is a group of recently developed laser spectroscopic techniques based on frequency comb (FC) laser sources. It typically implies spectroscopy over a broad spectral bandwidth [41]. The following will shortly introduce the FC and its basic principle of operation, provide information on the FC source used for this thesis, and give an overview of possible schemes of detection. Finally, direct frequency comb absorption spectroscopy using a Michelson interferometer with sub-nominal resolution will be presented.

3.4.1 Frequency comb laser sources

A FC is defined by its spectrum of phase-coherent evenly spaced narrow laser lines [41]. Figure 3.9 depicts the time and frequency domain of radiation emitted by the FC. In the time domain, the comb emits a train of pulses, which can differ in their respective phase-shift between the carrier wave and the envelope of the pulse trains. Properties in the time domain are reflected in frequency domain. The distance between comb modes corresponds to the repetition rate of the pulses f_{rep} , the pulse duration is inversely correlated to the spectral bandwidth of the FC, and the phase-shift $\Delta\phi_{CE}$ is linked to the carrier-envelope-offset frequency f_0 according to [39]:

$$f_0 = \frac{\Delta\phi_{CE}}{2\pi} f_{rep} \quad (3.13)$$

With control of f_{rep} and $\Delta\phi_{CE}$, the centre wavelength ν_n of the n -th mode is precisely determined by

$$\nu_n = n \cdot f_{rep} + f_0 \quad (3.14)$$

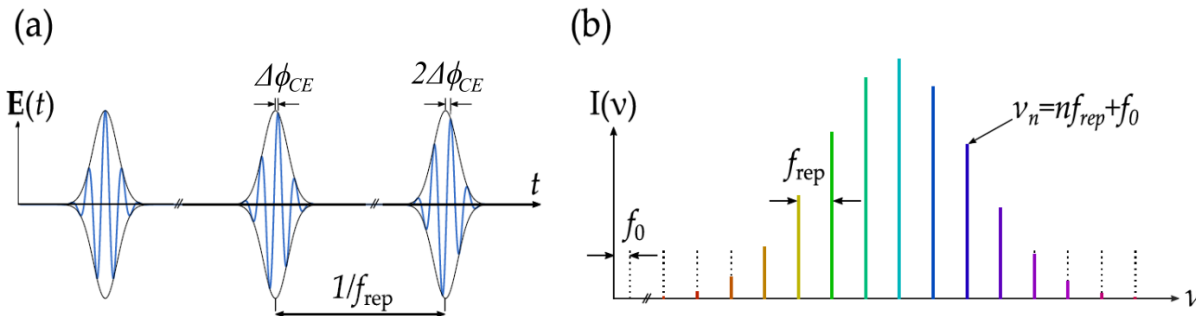


Figure 3.9 Schematic representation of the FC emission in time (a) and frequency (b) domain. The indicated phase-shift between the carrier wave (blue) and the envelope of the pulse trains (black) is increasing by $\Delta\phi_{CE}$ per pulse. The individual comb modes are coloured. Modified from [39].

The described characteristics can be produced using different technological approaches, resulting in FCs with differences in spectral coverage and repetition rate f_{rep} [39]. In a non-exhaustive list, Picqué and Hänsch group the approaches into femtosecond lasers [42 – 44], semiconductor lasers [45, 46], microresonator-based Kerr combs [47 – 49], difference frequency generation (DFG) [50 – 52], optical parametric oscillators (OPO) [53], and electro-optic modulators (EOM) [54]. Thereof, the approach using mode-locked fibre-based femtosecond lasers in the near-infrared region is described as mature, since commercial FCs are available with this technology.

With regard to this thesis, a mode-locked fibre-based femtosecond FC at a centre wavelength of 1560 nm is combined with a stabilized laser at 1040 nm to produce a FC at a centre wavelength of 3114 nm or 3211 cm^{-1} with the DFG process. The comb including the DFG unit was manufactured by Menlo Systems [55].

The used FC is based on the Figure9 geometry, schematically drawn in figure 3.10 and only briefly described here [56]. The laser cavity is composed of a linear section and a non-linear amplifying optical loop mirror (NALM). Radiation from a pump laser (1) is coupled into the NALM, maintaining the state inversion inside the active fibre section (2). This describes a section of the NALM doped with elements such as ytterbium (Yb), erbium (Er), thulium (Th), or holmium (Ho), in such a way to meet the requirements to generate and amplify laser radiation [30]. Next, a dampening element (3) limits the intensity of the laser within the cavity and further a non-reciprocal phase-shift optical element (4) stabilizes the carrier-envelope offset of the FC. The radiation is then coupled (5) into the linear cavity section, that can be partially free space and is terminated by a planar mirror (M) on a translational stage (6) moving coaxial to the linear cavity section. This way, the total length of the cavity is controlled and accordingly the frequency of the eigenmodes of the cavity, which in turn correspond to the repetition rate of the FC and the roundtrip time of the laser pulse. The pulsed radiation can then be extracted by the coupling element (5). Further processing using non-linear optical fibres and amplification result in two FC spectra centred around 1040 and 1560 nm with identical repetition rate f_{rep} and carrier-envelope offset f_0 . Finally, both signals are temporally and spatially overlapped in a DFG crystal, whereby the difference frequency signal is generated at around 3110 nm. Because both input signals possess an identical carrier-envelope offset f_0 , the difference frequency signal has no offset. Furthermore, the repetition rate f_{rep} is equal for all three signals.

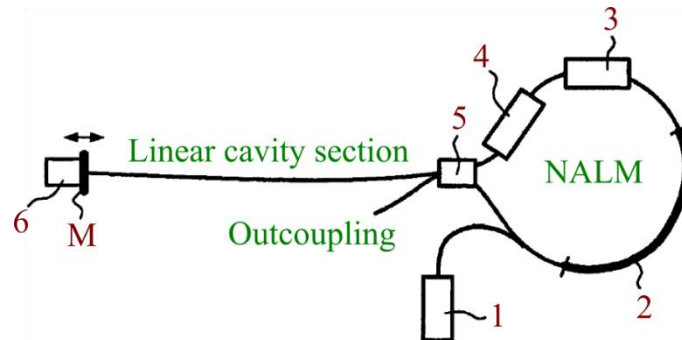


Figure 3.10 Schematic of the Figure9™ cavity geometry, as used in the FC in this thesis. A pump laser (1) maintains state inversion in the active fibre section (2), resulting in laser radiation limited by a loss element (3). The phase-shift is controlled by a non-reciprocal phase-shift optical element (4) and the loop is closed by an optical coupler (5). At the end of the linear cavity section, a planar mirror (M) is placed, that can be moved with a translational element (6). The FC radiation can be coupled out of the resonator by (5). Modified from [56].

Figure 3.11 a) shows the emitted spectrum of the FC between 2700 and 3500 cm^{-1} measured with a Michelson interferometer at a repetition rate f_{rep} of 250 MHz. Present absorption features are due to atmospheric water content with an absorption length of about 4 m. Subfigure b) details two lines of H_2O at circa 3030 cm^{-1} . The spectral distance between the sampling points is 250 MHz or 0.008339 cm^{-1} . Finally, subfigure c) depicts fringes that can be observed throughout the spectrum, caused by the DFG crystal.

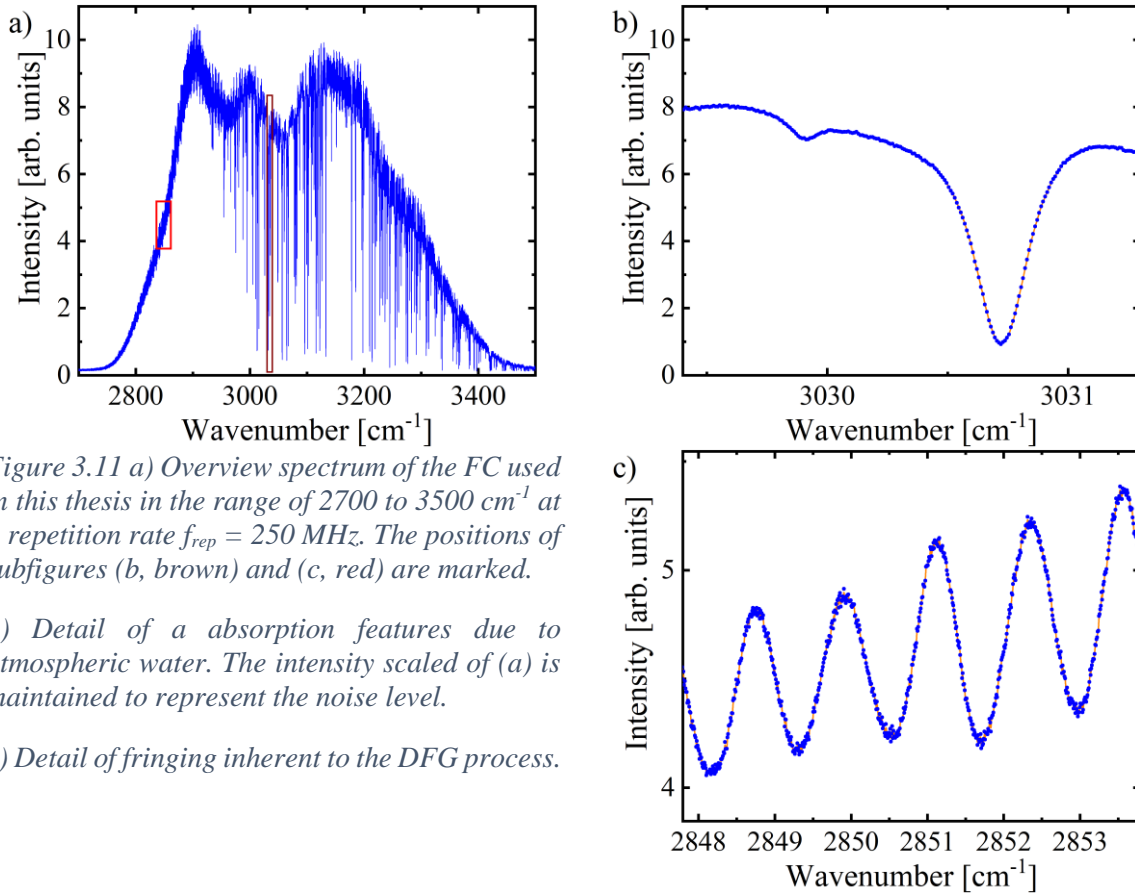


Figure 3.11 a) Overview spectrum of the FC used in this thesis in the range of 2700 to 3500 cm⁻¹ at a repetition rate $f_{rep} = 250$ MHz. The positions of subfigures (b, brown) and (c, red) are marked.

b) Detail of a absorption features due to atmospheric water. The intensity scaled of (a) is maintained to represent the noise level.

c) Detail of fringing inherent to the DFG process.

3.4.2 Detection schemes

To gain an advantage from the characteristics of a FC, a detection scheme should be capable to resolve single comb lines [41]. This way, the wavenumber axis can be calibrated using the well-defined comb spectrum and the data of multiple measurements at different FC parameters can be combined to further increase the resolution, a process called interleaving. Furthermore, the broadband emission of a FC benefits detection schemes that simultaneously measure the full spectral range. Figure 3.12 shows three such detection schemes. In figure 3.12 a) after passing the interrogated sample the FC emission is directed on a dispersive element, such as a grating or a virtually imaged phased array (VIPA) etalon. The spectral components are mapped on a detector, e.g. a CCD chip. Next, in subfigure b) a Michelson interferometer is used to analyse the disturbed FC emission, in analogy to using the FC as a source for a FTIR. Finally, subfigure c) shows the dual-comb approach, whereby one comb interrogates the sample and subsequently beats with an undisturbed reference comb at a slightly deviating repetition rate. From the functional principles this approach is very similar to the FTIR, with the benefit of no moveable parts involved in the setup. However, the lock of the second comb to the primary in terms of their repetition rates and phases to provide coherence between both over the measurement time of minutes or hours has proven a challenge [57]. Furthermore, as the measured time-domain interferogram is also truncated, dual-comb spectroscopy has an identical ILS function as the Michelson interferometer, given in equation (3.12).

To reduce the influence of the ILS function on the recorded spectra, the OPD of the Michelson interferometer or the equivalent delay in the dual-comb interferometer can be chosen considerably large, resulting in long acquisition times for both detection schemes, an example thereof shown in figure 3.13 for a dual-comb interferometer [57]. There the amplitude of the combined ILS halfway between two individual comb lines is approximately 10 % of the maximum amplitude. Furthermore, the FWHM of

the comb lines is given as 3.5 Hz, which is negligible compared with the observed instrumental broadening of some GHz.

An alternative way to reduce the influence of the ILS was first presented by Maslowski *et al.* in 2016 and detailed by Rutkowski *et al.* in 2018 [58, 59]. Figure 3.14 illustrates the benefit of matching the maximum OPD Δ_{max} , or the length of the recorded interferogram, to the repetition rate f_{rep} of the FC to gain subnominal resolution. The well-defined comb spectrum is shown as an equidistant pattern of Dirac δ -functions, with a single mode at the origin attenuated by e.g. a molecular absorption feature. Within the figure two cases are distinguished: Subfigure a) shows a mismatch, with the nominal resolution of a conventional spectrometer

$$f_{FTS}^0 = \frac{c}{\Delta_{max}} < f_{rep} . \quad (3.15)$$

The ILS of the attenuated comb mode is plotted in a dashed line and the superposition of the ILS functions of all individual comb modes is represented by a solid line and named ILS sum. This ILS sum is locally disturbed by the absorption feature and sampled at the frequency of the nominal resolution f_{FTS}^0 (solid points). Due to the mismatch between the nominal resolution and f_{rep} , the sampling of the ILS sum results in a ringing, centred on the absorption feature.

Subfigure b) displays the matched case. With the zero-crossings of the ILS of the reduced comb mode coinciding with the position of the neighbouring comb modes, the amplitude of each mode is reflected by a precisely matched sampling at the comb mode frequencies.

The technical realization of this approach uses a cw-laser at a stabilized wavelength λ_{ref} for length calibration. This way, to achieve a match between the FC and FTS frequency scales, a number of points

$$N_0 = \text{round}\left(q \frac{c}{2 \cdot \lambda_{ref} \cdot f_{rep}}\right) \quad (3.16)$$

are recorded to both sides of the single-burst at $\Delta = 0$. Thereby q is the integer number of sampling points per λ_{ref} . Figure 4.15 shows a single interferogram of 4 MS recorded with a sampling speed of 1 MS s^{-1} , symmetrically measured around the single-burst. Two insets are present, the first shows the centre region of the interferogram (red) with side features of the single-burst. The second focuses on the dominant feature of the single-burst around 1.899 MS. For noise-reduction, several measurements can be averaged either before or after the FFT operation is applied to the interferogram.

Rutkowski further details the effect of finite precision in matching [59]. Since the truncated interferogram has an integer number of sampling points, the nominal resolution f_{FTS}^0 can only be matched discretely to f_{rep} . Furthermore, the carrier envelope offset frequency f_0 needs to be taken into account when matching.

The presented method to effectively cancel the ILS for a FC setup results in high quality data across the recorded broadband spectrum of easily several hundred wavenumbers. This way, the simultaneous measurement of the full range allows for a comprehensive quantitative study of plasma-chemical conditions, involving several species and their translational, vibrational, and rotational temperatures. While this is also possible using traditional techniques such as tuning several EC-QCLs or FTIR spectroscopy using globars, the use of the novel FC sources considerably reduces acquisition times and experimental complexity, which in turn benefits in particular the investigation of plasmas and the reliability of the gathered data.

An experimental study of a nitrocarburizing plasma with a FC emitting at 2750 to 3450 cm^{-1} and recorded using a Michelson interferometer is presented in chapter 6. The measured background spectrum, including lines due to atmospheric absorption, was already presented in figure 3.11.

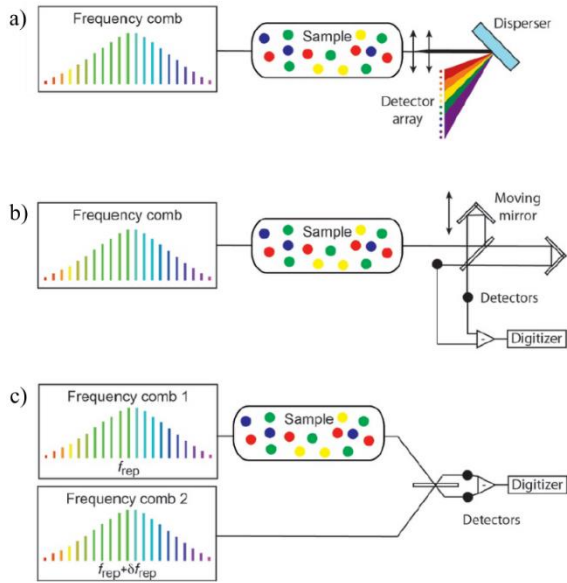


Figure 3.12 Detection schemes for FC absorption spectroscopy, a) using a dispersive element, b) using a Michelson interferometer, and c) by beating with an undisturbed second comb. Modified from [41].

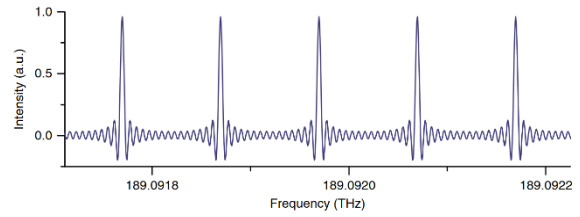


Figure 3.13 Detail of five comb lines around 189 THz (6304 cm^{-1}) with a repetition rate f_{rep} of 100 MHz. The data is averaged over 1860 s. The high sampling rate reflects the superposition of the ILS functions of the individual comb lines. From [57].

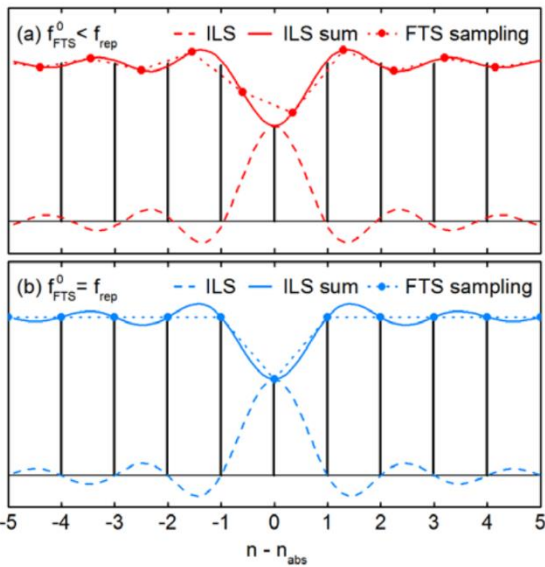


Figure 3.14 Schematic spectra of the ILS as a function of the numbered comb modes (black δ -functions), centred on a single attenuated comb mode at the origin. The ILS of the attenuated comb mode (dashed) and the superposition of the ILS of all comb modes (solid) are shown for a slightly mismatched (red) and a matched (blue) sampling. The sampling points (solid points) sample the ILS sum and show a ringing in case of the mismatch.

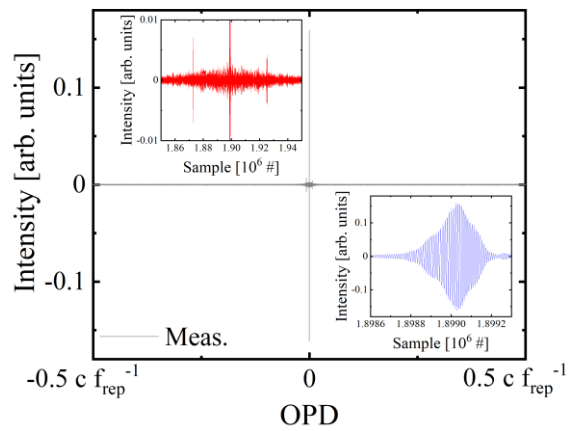


Figure 3.15 Recorded single interferogram as a function of the OPD in units of $0.5 c f_{\text{rep}}^{-1}$ for a FTS matched to a FC. 4 MS were recorded at a sampling speed of 1 MS s^{-1} . In a first inset the centre region (red) between 1.85 and 1.95 MS is showing side features, the centre burst (blue) at 1.899 MS is detailed in a second inset.

References

- [1] Hutchinson I H 2002 *Principles of Plasma Diagnostics*, Cambridge University Press (2nd ed.), Cambridge, UK
- [2] Ricard A *et al.* 1988 *Pure Appl. Chem.* **5** 747-751
- [3] Henrion G *et al.* 1992 *Plasma Sources Sci. Technol.* **1** 117-121
- [4] Rusňák K and Vlček J 1993 *J. Phys. D: Appl. Phys.* **26** 585-589
- [5] Gallo S C and Dong H 2009 *Surf. Coat. Technol.* **203** 3669-3675
- [6] Nagamatsu H *et al.* 2013 *Surf. Coat. Technol.* **225** 26-33
- [7] Hamann S *et al.* 2015 *J. Phys. D: Appl. Phys.* **48** 345204
- [8] Berg M *et al.* 2000 *Surf. Coat. Technol.* **124** 25-31
- [9] Quast M *et al.* 2001 *Surf. Coat. Technol.* **135** 238-249
- [10] Burlacov I *et al.* 2012 *Surf. Coat. Technol.* **206** 3955-3960
- [11] Egert Cortez P *et al.* 2018 *Mater. Res.* **21** e20180133
- [12] Henrion G *et al.* 1997 *Surf. Coat. Technol.* **97** 729-733
- [13] Hannemann M *et al.* 2013 *Surf. Coat. Technol.* **235** 561-569
- [14] Hamann S *et al.* 2013 *Plasma Sources Sci. Technol.* **22** 055022
- [15] Hamann S *et al.* 2015 *Rev. Sci. Instrum.* **86** 123503
- [16] Hamann S *et al.* 2015 *Contrib. Plasma Phys.* **55** 689-700
- [17] Burlacov I *et al.* 2016 *HTM J. Heat Treat. Mat.* **71** 141-147
- [18] Hamann S *et al.* 2017 *J. Appl. Phys.* **121** 153301
- [19] Dalke A *et al.* 2018 *HTM J. Heat Treat. Mat.* **73** 246-257
- [20] Burlacov I *et al.* 2018 *J. Appl. Phys.* **123** 233302
- [21] Puth A *et al.* 2018 *Plasma Sources Sci. Technol.* **27** 075017
- [22] Dalke A *et al.* 2019 *Surf. Coat. Technol.* **357** 1060-1068
- [23] Puth A *et al.* 2020 *Plasma Sources Sci. Technol.* **29** 035001
- [24] Herzberg G 1989 *Molecular Spectra and Molecular Structure, Volume I – Spectra of Diatomic Molecules*, Krieger Publishing Company (reprint ed.), Malabar, Florida, USA
- [25] PhD Thesis of Stephan Hamann, June 26th 2015, Greifswald, Germany
- [26] Gordiets B *et al.* 1998 *Plasma Sources Sci. Technol.* **7** 363-378
- [27] Gordon I *et al.* 2017 *J. Quant. Spectrosc. Radiat. Transfer* **96** 139
- [28] Spitzer L 1998 *Physical Processes in the Interstellar Medium*, Wiley (Wiley classics reprint edition 1998), New York, USA
- [29] Ngo N *et al.* 2013 *J. Quant. Spectrosc. Radiat. Transfer* **129** 89-100
- [30] Tran H *et al.* 2013 *J. Quant. Spectrosc. Radiat. Transfer* **129** 199-203

- [31] Tennyson J *et al.* 2014 *Pure Appl. Chem.* **86** 1931-1943
- [32] Tacke M 2001 *Phil. Trans. R. Soc. Lond. A* **359** 547-566
- [33] Schiebl U P and Rohr J 1999 *Infrared Phys. Technol.* **40** 328
- [34] daylightsolutions.com/home/technology/about-mid-ir-quantum-cascade-lasers/, DRS Daylight Solutions Inc., queried 11.02.2020
- [35] Röpcke J *et al.* 2000 *Rev. Sci. Instrum.* **71** 3706
- [36] Faist J *et al.* 1994 *Science* **264** 553-556
- [37] Schwaighofer *et al.* 2017 *Chem. Soc. Rev.* **46** 5903-5924
- [38] Griffith P R and Haseth J A 2007 *Fourier Transform Infrared Spectroscopy*, John Wiley and Sons (2nd ed.), Hoboken, New Jersey, USA
- [39] PhD Thesis of Alexandra C. Johansson, 2018, Umeå, Sweden
- [40] Davis S A and Brault M 2001 *Fourier Transform Spectrometry*, Academic Press (1st ed.), San Diego, California, USA
- [41] Picqué N and Hänsch T W 2019 *Nat. Photonics* **13** 146-157
- [42] Jun Y and Cundiff S T 2005 *Femtosecond Optical Frequency Comb Technology: Principle, Operation and Application*, Kluwer Academic Publishers / Springer (1st ed.), Norwell, Massachusetts, USA
- [43] Okubo S *et al.* 2015 *Appl. Phys. Express* **8** 082402
- [44] Bernhardt B *et al.* 2010 *Appl. Phys. B* **100** 3-8
- [45] Rösch M *et al.* 2018 *Nanophotonics* **7** 237-242
- [46] Link S M *et al.* 2017 *Science* **356** 1164-1168
- [47] Suh M G *et al.* 2016 *Science* **354** 600-603
- [48] Dutt A *et al.* 2018 *Sci. Adv.* **4** e1701858
- [49] Yu M *et al.* 2018 *Nat. Commun.* **9** 1869
- [50] Seidel M *et al.* 2018 *Sci. Adv.* **4** eaaq1526
- [51] Ycas G *et al.* 2018 *Nat. Photonics* **12** 202-208
- [52] Finneran I A *et al.* 2015 *Phys. Rev. Lett.* **114** 163902
- [53] Maidment L *et al.* 2016 *Optics Letters* **41**:18 4261-4264
- [54] Millot G *et al.* 2016 *Nat. Photonics* **10** 27-30
- [55] Menlo Systems GmbH, Martinsried, Germany
- [56] Hänsel W 2015 *EU Patent Specification* 2846421 A1
- [57] Chen Z *et al.* 2018 *Nat. Commun.* **9**:3035
- [58] Maslowski P *et al.* 2016 *Phys. Rev. A* **93** 021802(R)
- [59] Rutkowski L *et al.* 2018 *J. Quant. Spectrosc. Ra.* **204** 63-73

4 Investigation at an industrial-scale ASPN reactor using an AS made of CFC

In the following, experimental studies conducted at an industrial-scale ASPN reactor using an AS made of CFC will be presented. The first section is based on the 2020 publication of Puth *et al.* and focusses on the dependencies on different total gas flow values and pressure values on the plasma-chemical environment [1]. The second section is based on the 2019 publication of Dalke *et al.* with the focus on correlating material diagnostic results to the plasma-chemical condition as dependent on the mixing ratio of hydrogen to nitrogen $H_2:N_2$ in the feed gas [2]. A final third section presents currently unpublished data on the effect of admixed oxygen-containing species O_2 and CO_2 .

4.1 Study of plasma-chemical processes as functions of the total gas flow and pressure¹

4.1.1 Introduction

In the field of thermal treatments of materials nitriding and carburizing, and the combination of both, called nitrocarburizing, are standard practices to improve the wear and corrosion resistance of steel components. The basic mechanism for this improvement is the diffusion of nitrogen, carbon, or both respectively at temperatures of up to 823 K into the lattice structure of the material, which typically expands and thus forms expanded austenite or the so-called s-phase. Due to the expansion the material is locally hardened, generating hardness profiles that correspond to the diffusion depth from the interface. The benefit of the combination treatment of nitrocarburizing is a smoother transition of hardness and thus typically a higher load-bearing capacity [3]. While the diffusion mechanism can also be achieved using gas or salt bed reactors, the use of plasma nitrocarburizing (PNC) has the advantage of a lower environmental impact at a reduced processing time [4]. In part, this is due to an in-process activation of the diffusion interface by removal of the oxide layer. However, current industrial implementations of the PNC technology still are limited in their variation of the carburizing potential as the carbon content within the process is regulated using carbon-containing admixtures to the feed gas. This can lead to oversaturation of the process atmosphere, in turn causing soot production and generation of cementite in the compound layer [5]. So far, process control in industrial applications is based on the operator's empirical experience. Already in 1997, Mittermeijer and Somers published about the prospect of a general nitriding process control with process control for plasma nitrocarburizing being far out of reach [6].

Current industrial applications of plasma-assisted nitrocarburizing are commonly conducted by conventional plasma nitrocarburizing (CPNC). Therein the workload is negatively biased relative to the grounded reactor walls. At a few mbar of pressure, a pulsed dc glow discharge is maintained, producing reactive species from the feed gas of H_2 , N_2 , and carbon-containing species. The plasma heats the workload to a temperature between 673 and 823 K, thus enabling diffusion processes to take place. However, depending on the workload geometry the temperature distribution may not be homogenous and therefore causes uneven treatment progress, the so-called edge effect [7]. The plasma may as well sputter the workload surface, requiring post-treatment polishing.

These drawbacks have led to the development of the active screen plasma nitrocarburizing (ASPNC) technology. In this approach, the glow discharge is placed at an intermediate steel screen, called active screen (AS), which surrounds the workload and allows a gas flow to pass from the plasma region to the workload providing the reactive species required for the hardening process. Even though for industrial-

¹ Published as: Puth A, Kusýn L, Pipa A V, Burlacov I, Dalke A, Hamann S, van Helden J H, Biermann H, and Röpcke J 2020 *Plasma Sources Sci. Technol.* **29** 035001

scale reactors a secondary plasma directly at the workload is still required to achieve a reasonable nitrocarburizing response, the secondary plasma is operated at a fraction of the power of the AS plasma. Consequently, thermal inhomogeneity and sputtering are reduced [8 – 10].

Several studies and proposals already discussed admixtures to the feed gas to affect the process conditions and treatment results [11 – 13]. However, with the AS being introduced as a cathode in a reactive plasma, it can be sputtered and thus serves as an additional solid chemical source. To investigate the mechanism of nitriding with an ASPNC reactor, Hubbard *et al.* studied the mass transfer from an AS made of steel to the workload and found that sputtered material does not contribute to the nitriding of the substrate [8]. Independent on this study, other groups investigated co-alloys to the AS, such as aluminium and silver, to produce e.g. antimicrobial surfaces, again via the mass transfer from AS to the workload [14, 15]. A different approach is the substitution of steel as screen material with a solid made of carbon, such as graphite or carbon-fibre-reinforced carbon (CFC). The use of a solid carbon source has been first proposed by Lebrun *et al.* and realised by Crespi *et al.* for CN_x deposition on a polymer substrate [16, 17]. The application for ASPNC has then been reported by Burlacov *et al.* and Hamann *et al.* in 2017, for industrial- and laboratory-scale reactors respectively [18, 19]. In both works it has been found that an AS made of CFC affects the process atmosphere most drastically in the concentrations of HCN and C_2H_2 which increased by a factor of 30 and 70 respectively compared with 1% admixture of CH_4 in the H_2-N_2 feed gas typical for ASPNC processes using a steel AS. This is of particular interest since beneficial diffusion conditions created by the highly reactive HCN molecule were first reported in the early 1990s [20, 21]. In a later study, Burlacov *et al.* identified the concentration of HCN as a control parameter for the carburizing potential of the nitrocarburizing process [22].

To monitor the concentrations and temperatures of HCN and further species, non-intrusive *in-situ* diagnostics are required. In the past spectroscopic methods such as optical emission spectroscopy (OES), Fourier transform spectroscopy in the infrared (FTIR), and laser absorption spectroscopy (LAS) have been used for this purpose [18, 19]. Thereof, LAS is exemplary due to the high quality quantitative information and high sensitivity it offers. Depending on the selected laser source, different species are available for detection. In previous studies lead salt diode lasers (TDL) have been used to measure the transient CH_3 radical as well as CO, CO_2 , C_2H_4 , and C_2H_6 [23]. Within the early 2000s, external-cavity quantum cascade lasers (EC-QCL) became commercially available and found widespread application. While technologically limited in their achievable spectral range, they tuned over a much broader range than TDLs and this way allows a near-simultaneous multi-species detection. In the study of ASPNC processes, both types of sources were extensively used in combination with OES and other spectroscopic techniques. This way 14 species were detected within the plasma process, and as mentioned before partially linked with the treatment behaviour [2, 19, 22, 24].

Some of these measurements were conducted at the laboratory-scale plasma nitriding monitoring reactor (PLANIMOR) [25]. This reactor was specifically constructed to simulate the plasma-chemical conditions present in an industrial-scale plasma nitriding process, while simultaneously offering improved access for diagnostics, including spatially resolved LAS measurements of the afterglow region. A comparative study between PLANIMOR and an industrial-scale reactor has proven the general similarities in respect to the plasma-chemical behaviour of both types [26]. Consequently, the plasma-chemical similarities also are reflected in the nitriding treatment of samples in both systems, resulting in a comparable thickness of the compound layer.

Recently, the results of investigations on plasma processes using an AS made from CFC in PLANIMOR have been published [24]. In this study the concentrations, temperatures, and conversion efficiencies of nine molecular species were measured as functions of the plasma power at the AS, the pressure, and the nitrogen fraction in the feed gas. Additionally the carbon mass flow from the AS and the efficiency of the carbon mass flow in relation to the applied power were presented. The present study is a continuation of the former and investigating the plasma processes of an AS in an industrial-scale ASPNC reactor. To find the influence of process pressure and feed gas flow, a constant temperature is maintained inside the

reactor while the concentrations and temperatures of HCN, NH₃, CH₄, C₂H₂, and CO were measured using EC-QCLAS and TDLAS.

The current study focuses on the production rate of the five molecular species, their dependence on the gas flowrate and finally the scalability of the concept for an AS made of carbon materials. Further observations concern the sole detected oxygen-containing species CO as a measure of contamination with oxygen, since previous studies by Burlacov *et al.* pointed out the importance of contamination in industrial-scale reactors [22].

4.1.2 Experimental

A crosscut schematic of the industrial-scale reactor with the LAS setup including three laser sources is shown in figure 4.1. As indicated by the presence of two flipping mirrors the laser sources are co-aligned and cannot be used simultaneously. Furthermore, two Daylight Solutions external-cavity quantum cascade lasers (EC-QCL), labelled as QCL I and QCL II, provide mode-hop free spectral ranges of $\nu_{\text{I}} = 1345 - 1400 \text{ cm}^{-1}$ and $\nu_{\text{II}} = 1770 - 1850 \text{ cm}^{-1}$, respectively [27]. In addition, the infrared multi-component acquisition system (IRMA) has been used, which combines three lead salt tuneable diode laser (TDL) sources to a single acquisition system [28]. Table 4.1 presents a list of detected species and their respective spectral positions, line strengths and limits of detection, whereby the superscript Q and T designate the measurement with an EC-QCL or a TDL source, respectively. The reference and etalon spectra of the EC-QCLs were measured simultaneously using a three-channel setup. For the TDL sources, they were measured separately.

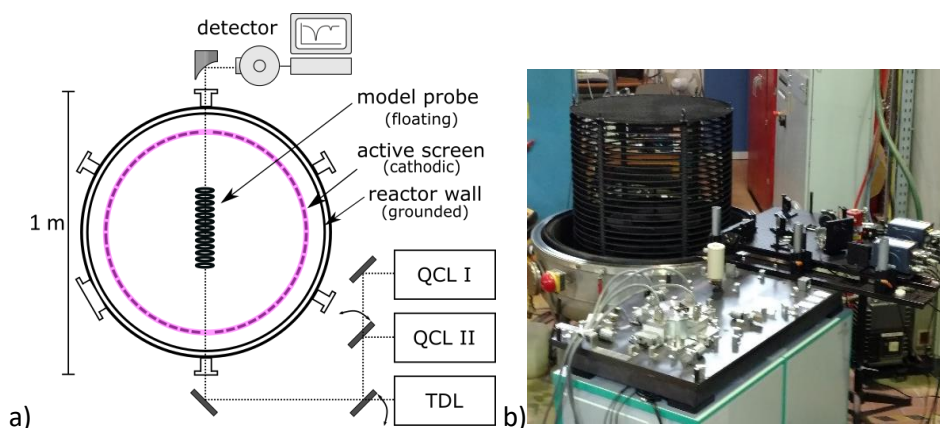


Figure 4.1 a) Schematic top view of the experimental setup and b) photograph of the open reactor (left background), QCLs (right), and IRMA (left foreground). Both QCL and the TDL absorption spectrometer share the same beam path and detector. The beam path passes through the reactor, including the plasma at the AS made of CFC depicted in pink. A scale of the absorption length is given.

The shared beam path enters and exits the reactor through two KBr windows at a distance of 1 m, which is assumed identical to the length of absorption. A model sample composed from 26 equidistant punched discs is placed in the centre of the reactor, aligned to the beam path. It serves to simulate the influence of a workload for nitrocarburizing and can be biased for this purpose. Finally, a liquid nitrogen cooled HgCdTe detector positioned at the focus of an off-axis parabolic generates an analogue signal for data acquisition.

The reactor itself has a cylindrical volume of approximately 1 m^3 , at a diameter of 1 m. It contains the AS made of CFC with a diameter of 0.8 m and a height of 0.75 m. Besides the top plate, the screen is composed of circular sections made of CFC each covering 60° of the cylinder's perimeter with 20 mm radial depth, distanced 20 mm in height between each section. The thickness of the CFC base material is 5 mm. All components included, the AS weighed approximately 30 kg.

Table 4.1 Species, spectral positions, and line strengths, at room temperature, used for infrared LAS measurements and their estimated limits of detection. The laser source for the given spectral position is denoted with a *Q* for an EC-QCL and a *T* for TDL sources. Data taken from the HITRAN database [29].

Species	Spectral position [cm ⁻¹]	Absorption line strength [cm ⁻¹ /(molecule cm ⁻²)]	Limit of detection [molecules cm ⁻³]	Ref.
CH ₄ ^(Q)	1356.4868	1.784·10 ⁻²⁰	2·10 ¹³	[30]
CH ₄ ^(Q)	1356.5974	1.190·10 ⁻²⁰	2·10 ¹³	[30]
NH ₃ ^(Q)	1388.0552	2.726·10 ⁻²²	2·10 ¹⁴	[31]
NH ₃ ^(Q)	1767.5181	6.090·10 ⁻²¹	2·10 ¹³	[31]
C ₂ H ₂ ^(Q)	1356.8305	5.899·10 ⁻²²	5·10 ¹⁴	[32]
C ₂ H ₂ ^(Q)	1356.8881	8.920·10 ⁻²¹	2·10 ¹³	[32]
HCN ^(Q)	1356.9389	4.636·10 ⁻²³	4·10 ¹⁴	[33]
HCN ^(Q)	1388.3225	3.592·10 ⁻²²	1·10 ¹⁴	[34]
CO ^(T)	2150.3409	1.840·10 ⁻²¹	2·10 ¹¹	[35]
CO ^(T)	2150.8560	1.826·10 ⁻¹⁹	2·10 ¹³	[35]

For plasma generation a pulsed dc power supply with a maximum power of $P = 15$ kW at a frequency of $f = 1$ kHz and a duty cycle of 60 % is connected with the AS. The steel reactor wall is grounded and the model probe is on a floating potential. During the measurement, the system regulated the power at the AS between 6.0 and 8.5 kW to maintain a stable temperature of $T_{\text{set}} = 773$ K, measured with a thermal probe integrated in the model probe. The plasma power at the AS as a function of the total gas flow for different pressures is shown in figure 4.2. At the lower limit of the pressure range, the discharge was not stable, reflected by a reduced power consumption.

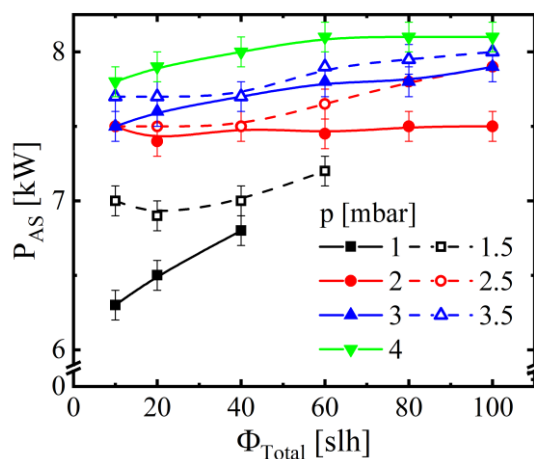


Figure 4.2 Plasma power at the active screen P_{AS} at different pressures measured as a function of the total gas flow. Conditions: $H_2:N_2 = 1:1$, $T_{\text{set}} = 773$ K. Lines are guides of eye.

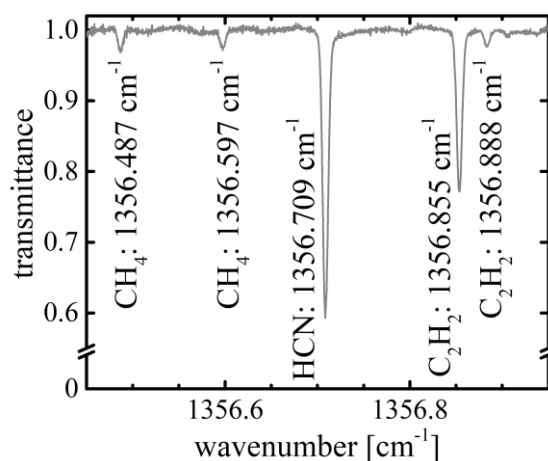


Figure 4.3 EC-QCL absorption spectrum of CH_4 , HCN , and C_2H_2 around 1356.7 cm⁻¹. Conditions: $H_2:N_2 = 1:1$, $\Phi_{\text{Total}} = 80$ slh, $T_{\text{set}} = 773$ K, $p = 3$ mbar.

The precursor composition is controlled by mass flow controllers. In turn, the feed-gas is led into the reactor via a showerhead integrated into the reactor top. This way H_2 , N_2 , and Ar were introduced, the latter only during starting process of the reactor to provide a stable plasma until the chosen treatment temperature was reached. The total mass flow varied from $\Phi_{\text{Total}} = 10 - 100$ slh, at a mixing ratio $H_2:N_2$ of 1:1. The pumping system is connected to the bottom of the reactor, including a butterfly valve allowing the control of gas pressure in the range of $p = 1 - 4$ mbar.

An EC-QCL absorption spectrum in the spectral range near 1356.7 cm⁻¹ with specified absorption lines assigned to CH_4 , HCN , and C_2H_2 recorded with EC-QCLAS is shown in figure 4.3. The conditions were

as follows: $\Phi_{\text{Total}} = 40 \text{ slh H}_2 + 40 \text{ slh N}_2$, $T_{\text{set}} = 773 \text{ K}$, $P_{\text{Bias}} = 0 \text{ W}$, $p = 3 \text{ mbar}$. For the determination of the temperature, line profile analysis has been used to obtain the translational temperature, associated with Doppler broadening. The laser linewidth, determined at a room temperature reference, has been taken into account. We calculated concentrations with Beer-Lambert law using temperature dependent line information from the HITRAN database [29] and derived mole fractions with the ideal gas law. The production rate $r_{\text{Production},i}$ of a species i is given by

$$r_{\text{Production},i} = n_{\text{mole},i} \cdot \Phi_{\text{Total}} \text{ ,} \quad (4.1)$$

whereas $n_{\text{mole},i}$ is the mole fraction of the species i and Φ_{Total} is the total gas flow through the reactor with the unit slh. We assume that the plasma-chemical reactions are in a steady state equilibrium. The rate of production has the unit of slh. The carbon mass flow Φ_C is given by

$$\Phi_C = \sum_i r_{\text{Production},i} \cdot N_{C,i} \text{ ,} \quad (4.2)$$

with $r_{\text{Production},i}$ being the production rate of species i in slh, $N_{C,i}$ being the number of carbon atoms within species i and the sum including all species in the process. The carbon mass flow has natively the unit of slh, which is converted to mg h^{-1} using the atomic mass of carbon and the ideal gas law to better relate it with the macroscopic mass of the AS. Finally, the carbon consumption efficiency E_{CC} is given by

$$E_{CC} = \frac{\Phi_C}{P} \text{ ,} \quad (4.3)$$

whereas Φ_C is the carbon mass flow in mg h^{-1} and P is the plasma power at the AS. Accordingly, E_{CC} has the units of $\text{mg h}^{-1} \text{ W}^{-1}$. Additionally, the overall conversion X_i of a species i is given by

$$X_i = \frac{\sum_j n_j \cdot N_{i,j}}{n_i} \text{ ,} \quad (4.4)$$

with n_i being the concentration of species i , meanwhile $N_{i,j}$ is a proportionality factor for correlation of the resulting species j to the feed gas species i . The right hand side of the equation chain is equivalent to equation (4.2) with the consideration that the feed gas species are diatomic molecules. The concentration is given in the unit of cm^{-3} .

4.1.3 Results and discussion

Due to the temperature dependence of the absorption line strength, the temperature has been determined for the available species using line profile analysis. For the transitions of the available species HCN, CH₄, CO, NH₃, and C₂H₂ the line profiles correspond to the set process temperature of $T_{\text{set}} = 773 \text{ K}$. Apart from that a thermal equilibrium between rotational and translational temperatures is assumed. Even if the rotational temperatures are not directly available in this study, in reference [36] comparable values for the process temperature measured at the model probe and for the rotational temperature measured in the plasma at the steel screen have been found. However, it should be noted that LAS is a line-of-sight method allowing only line-averaged results and as such does not allow any spatially resolved information in the used geometry. Thus, the active plasma zone at the carbon screen may have a higher temperature or even no thermal equilibrium at all.

Using the line strengths for 773 K, the absolute concentrations of the detected species have been determined. To demonstrate the chronological order of measurement, the absolute concentration of HCN at different gas flows measured as a function of pressure is presented in figure 4.4. The measurements were conducted at a set gas flow, varying the pressure until moving on to a new set gas flow starting with a total flow of 10 slh. As the pressure increases, the concentration of HCN increases linear within the margin of error from 2.5 to $14 \cdot 10^{16} \text{ cm}^{-3}$ in case of the lowest gas flow. On the other hand increasing the total flow decreases the concentration from 14 to $6 \cdot 10^{16} \text{ cm}^{-3}$ at the pressure of 4 mbar. At lower

pressures, the decrease is less pronounced, and in some low pressure and high total gas flow settings, no stable discharge was achieved.

In figure 4.5, the concentration of HCN is shown at different gas pressures as a function of the residence time with a logarithmic x-axis. With increasing residence time, a monotonous increase of the concentration of HCN can be seen at every pressure, typically with a steeper increase at higher pressure. Due to the high reactor volume, the residence time ranges in the minutes. Since the concentration of HCN is dependent on the resident time even at high values of the residence time, one has to assume that surface reactions are contributing to the production of HCN. Similar increases were observed for the concentrations of C_2H_2 , CH_4 , and CO , with only the concentration of NH_3 decreasing with residence time. Accordingly, for the generation of all detected species surface processes are non-negligible.

Subsequent figures present the mole fractions in dependence on the total gas flow. Accordingly, figure 4.6 a) – e) shows mole fractions of HCN, C_2H_2 , CH_4 , CO , and NH_3 measured as a function of the total gas flow for different pressures. As the total gas flow increases the mole fractions of HCN, C_2H_2 , CH_4 , and CO decrease. Concerning HCN and C_2H_2 , the respective mole fractions share very similar trends. Accordingly the ratios of the two mole fractions, which is equal to the ratios of the two concentrations can be approximately given as $[C_2H_2]:[HCN] \approx 0.17$ at all gas flow settings. Both mole fractions, as well as the mole fraction of CH_4 , decrease by a factor of 2 between a total flow of 10 and 100 slh. However, the mole fraction of CH_4 reaches a plateau at 60 slh of total gas flow. Furthermore, the mole fraction of CO decreases by approximately a factor of 10 within the same range of the total gas flow, from 5.5 to 0.5 %. In that relation, only NH_3 is an outlier of the five species, its mole fraction increasing linear with the total gas flow by a factor of 2 over the full range of the total gas flow. The mole fractions of HCN, C_2H_2 , and CO indicate only a weak or no dependency on pressure, while those of CH_4 and NH_3 show a clear dependency on pressure. The mole fractions of both species increase with growing pressure.

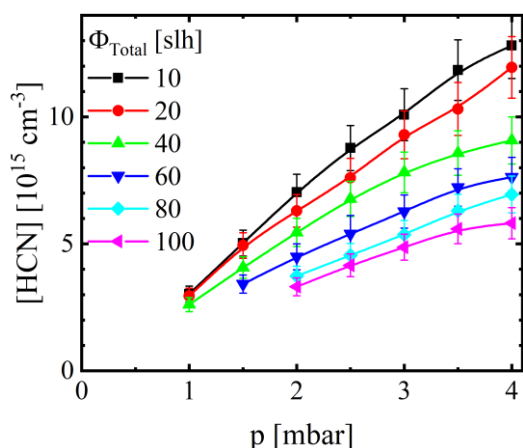


Figure 4.4 Concentration of HCN at different total gas flows measured as a function of the gas pressure. Conditions: $H_2:N_2 = 1:1$, $T_{set} = 773$ K. Curves are guides of eye.

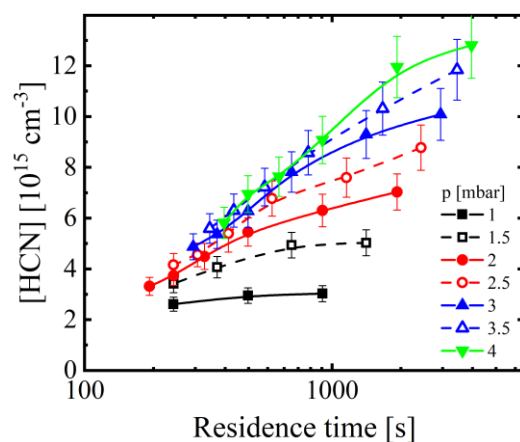


Figure 4.5 Concentration of HCN at different gas pressures measured as a function of the residence time. Conditions: $H_2:N_2 = 1:1$, $T_{set} = 773$ K. Curves are guides of eye.

For further analysis of the data, the production rates at stationary conditions of each molecular species were determined by applying equation (4.1). The production rates of HCN and C_2H_2 for different pressures measured as a function of the total gas flow are shown in figure 4.7 a) and b) respectively. While both are independent on the pressure and increase with the total flow, the slopes decreases with higher total gas flow values. For the production rate of CH_4 in figure 4.7 c) a nearly linear increase with the gas flowrate can be identified, while the production rate of NH_3 , shown in figure 4.7 d), increases over proportionally with the gas flow. However, the production rate of CO , as shown in figure 4.7 e), decreases with the total gas flow with the exception of the lowest gas flow setting. It is independent on pressure. Since we supply no oxygen-containing species, the two available sources for CO formation can be wall attachment and leakage, with the wall attachment contribution typically decreasing with

time. Figure 4.8 shows the production rate of CO as a function of time of measurement. The measurement was taken in two sessions, the first session concluded after circa 9 h and the second session began at 25 h as indicated by the break in the time axis. During the break, no plasma was active, the total gas flow was stopped and the reactor chamber was actively evacuated. From data point to data point the pressure was changed, the stepwise increase of the total gas flow is indicated in green. With the exception of the lowest total gas flow setting, the production rate of CO decreases linear from 0.6 to 0.4 slh during the active time of the plasma. Even the break has little influence on the trend, as indicated by the good continuity of two linear fits, fit A before and fit B after the break. Therefore, the most likely oxygen source is the contamination of the reactor wall and the active screen with oxygen-containing species. With CFC being a highly porous material, this assumption is well founded. The observed dependency of the production rate of CO on the total gas flow, as shown in figure 4.7 e), should therefore be interpreted as a dependency on the active time of the plasma. Since the measurement procedure created a direct correlation between the active time of the plasma and the total gas flow, deriving a pure dependency of the production rate of CO on the total gas flow is impossible.

Focusing again on the intentionally admixed feed gas, in figure 4.9 the conversions of hydrogen, X_{H_2} , and nitrogen, X_{N_2} , are shown at different pressures measured as functions of the total gas flow, as determined by equation 4 assuming that only the detected species and the feed gas species are present in the reactor. While measurements at PLANIMOR have shown that other species are created, such as C_2N_2 or CN, their concentrations are negligible [24]. The higher set of curves corresponds to the conversion of hydrogen and the lower set to the conversion of nitrogen. Both set of curves in figure 4.9 decay from 62 to 45 % and from 35 to 25 % respectively, while at the same time showing no dependency on the pressure. Figure 4.9 also allows to calculate the mole fractions of hydrogen and nitrogen according to

$$n_{mole,i} = \frac{(1-X_i)}{2} , \quad (4.5)$$

with $n_{mole,i}$ being the mole fraction of species i . One can see the decrease of the mole fraction of the most abundant species HCN with increasing total gas flow being reflected in a decreased conversion of both hydrogen and nitrogen. This is only partially compensated by an increased mole fraction of NH_3 , resulting in a larger mole fraction of both hydrogen and nitrogen at high total gas flow compared with a low total gas flow. In order to explain this trend the third constituent of HCN, i.e. carbon, was investigated.

The detected species can be separated in carbon-containing species, such as HCN, C_2H_2 , CO, and CH_4 , and carbon-free NH_3 . Consequently, the carbon mass flow is determined by using equation (4.2), as shown in figure 4.10 a) for different pressures measured as a function of total gas flow. The carbon mass flow reflects the consumption rate of the CFC cathode of finite mass, as previously shown at PLANIMOR [24]. It can be assumed that no carbon-containing species of noteworthy concentrations remained undetected. Since HCN is the most abundant carbon-containing species, the trends of the carbon mass flow are similar to those of the absolute production rate of HCN, so increasing with the total gas flow but being independent on the pressure. The slope of the carbon mass flow in dependency on the total gas flow decreases at high values of total gas flow, indicating a limit to the release of carbon.

Such a limit to the release of carbon may explain the trends of the production rates as seen in figure 4.7. At low total gas flow settings, the release of carbon is sufficient to create large amounts of carbon-containing species. In turn, these carbon-containing species bind a large fraction of the available hydrogen and nitrogen, leading to lowered concentrations of NH_3 . As the total gas flow increases, the release of carbon can only scale weaker than linear. This limits the production rates of carbon-containing species, thus e.g. the mole fraction of HCN is reduced. Accordingly, the conversions of the feed gas species are lowered and higher amounts of hydrogen and nitrogen are available for the formation of NH_3 . Finally, the mole fraction of NH_3 increases, as observed in figure 4.6 d). The production rate of

CO is the only outlier of the carbon-containing species, due to its dependence on oxygen concentration, which is not intentionally admixed.

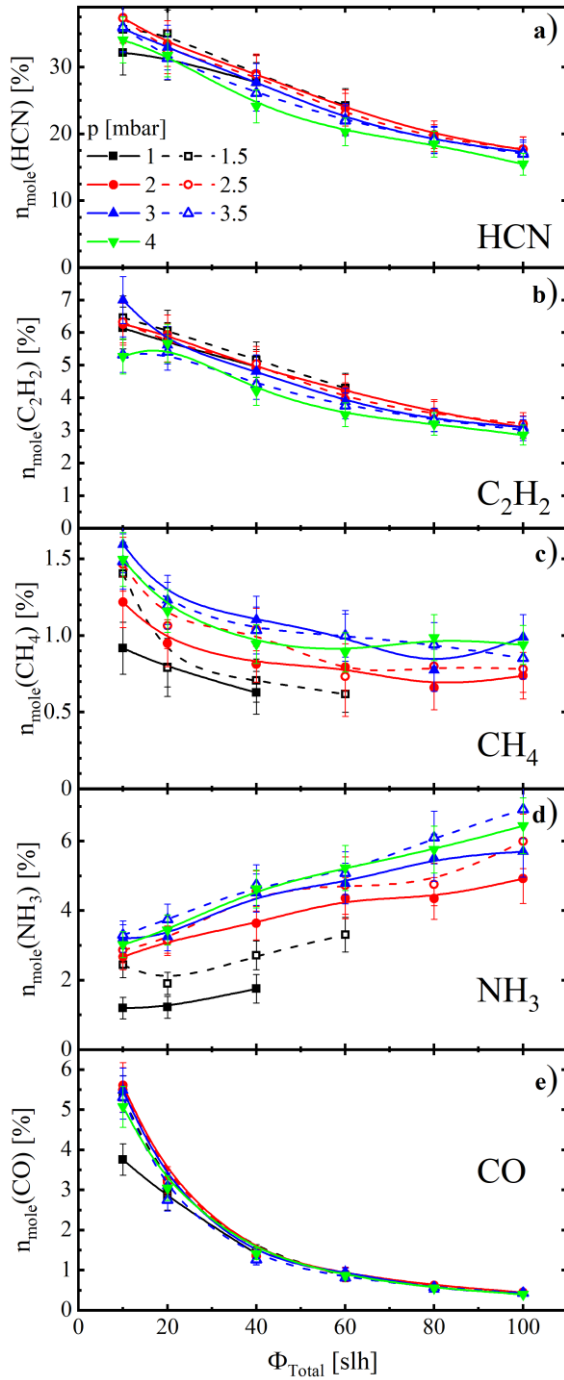


Figure 4.6 Mole fractions of a) HCN , b) C_2H_2 , c) CH_4 , d) NH_3 , and e) CO at different gas pressures measured as a function of the total gas flow. Conditions: $H_2:N_2 = 1:1$, $T_{\text{set}} = 773$ K. Curves are guides of eye.

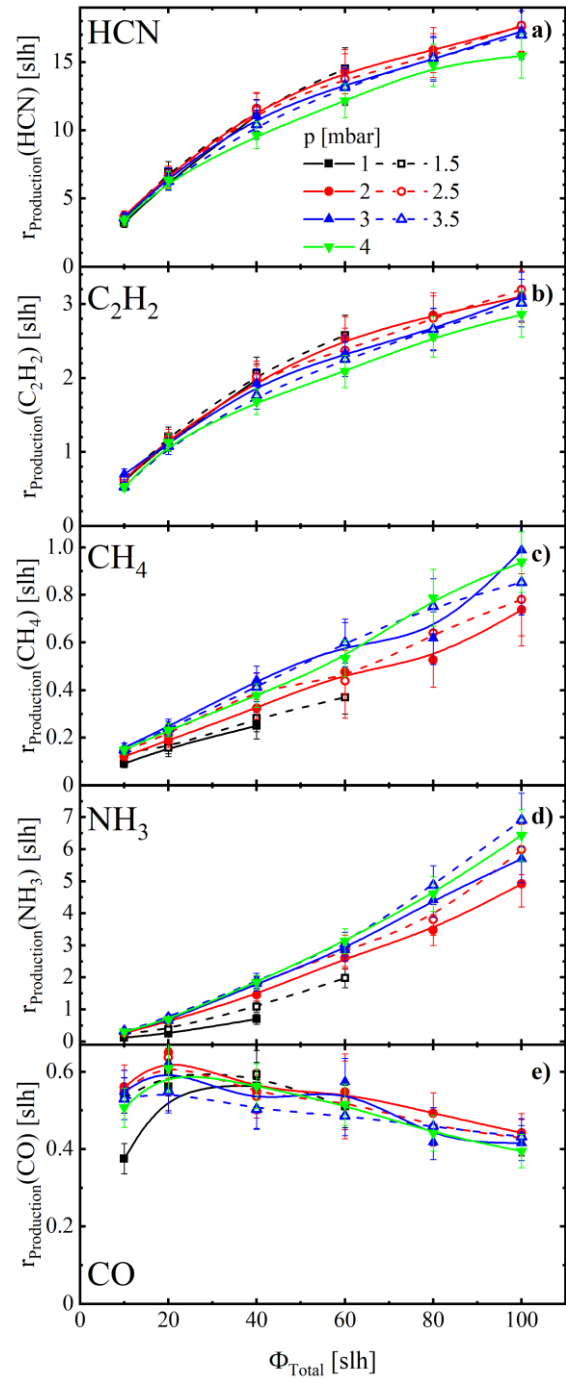


Figure 4.7 Production rates of a) HCN , b) C_2H_2 , c) CH_4 , d) NH_3 , and e) CO at different gas pressures measured as a function of the total gas flow. Conditions: $H_2:N_2 = 1:1$, $T_{\text{set}} = 773$ K. Curves are guides of eye.

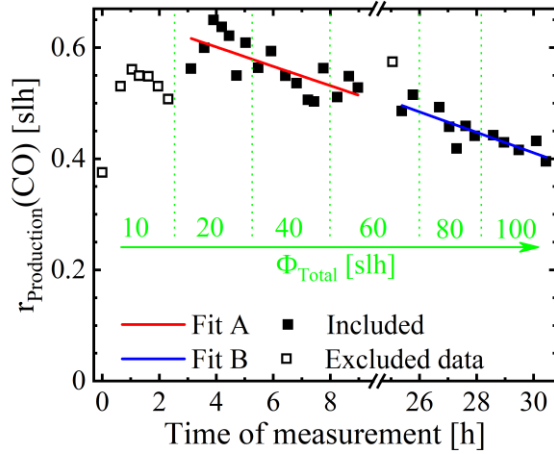


Figure 4.8 Production rate of CO as a function of the time of measurement. During the indicated break in the x-axis, no plasma was applied and the reactor was actively evacuated. The stepwise increased gas flowrate is indicated in green, as well as two linear fits before and after the break.

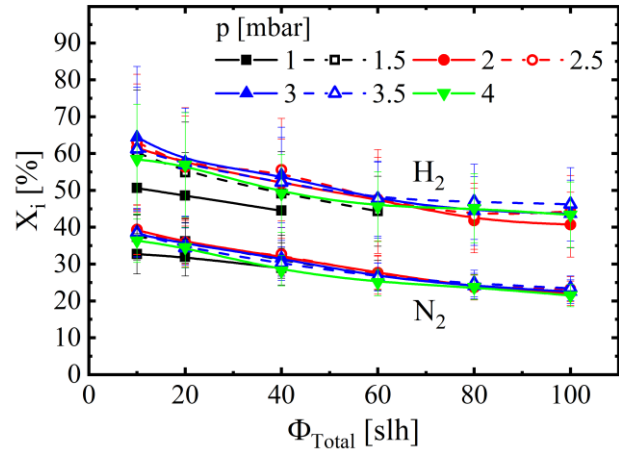


Figure 4.9 Conversions X_{H_2} and X_{N_2} at different gas pressures as a function of the total gas flow. The higher set of curves is associated with H_2 , the lower for N_2 . Conditions: $H_2:N_2 = 1:1$, $T_{set} = 773$ K, $P_{Bias} = 0$ W.

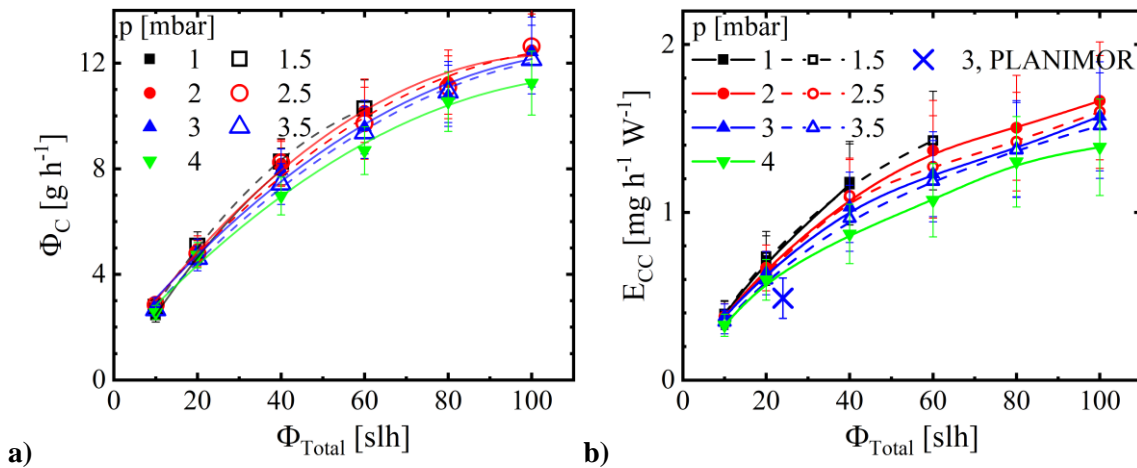


Figure 4.10 a) Carbon mass flow Φ_C and b) carbon consumption efficiency E_{CC} measured at different pressures as a function of the total gas flow. Conditions: $H_2:N_2 = 1:1$, $T_{set} = 773$ K, $P_{Bias} = 0$ W. In a) second order polynomial fits are used as guides of eye. In b) the carbon consumption efficiency at 3 mbar in PLANIMOR is added with a x as comparison [24]. Curves are guides of eye.

Using equation (4.2), the carbon consumption efficiency E_{CC} has been calculated and found to range between 0.13 and 1.9 $\text{mg h}^{-1} \text{W}^{-1}$, as presented in figure 4.10 b). The trends of E_{CC} strongly correlate with the trends of the total carbon mass flow, as the power only slightly varies for different gas flows and different pressures. For comparison we can again refer to investigations on the laboratory-scale PLANIMOR [24] where for a pressure $p = 3$ mbar and a feed gas mixture $H_2:N_2 = 1:1$ the carbon consumption efficiency ranged between 0.7 and 0.9 $\text{mg h}^{-1} \text{W}^{-1}$ depending on the power at the AS.

Taking the cross section of both reactor designs into account to compare flow speeds, the mass flow of PLANIMOR of 20 sccm corresponds to a flow of 24 slh in the industrial scale reactor. The closest measured value of gas flow is 20 slh with a carbon consumption efficiency of $E_{CC} = 0.6 \pm 0.07$ $\text{mg h}^{-1} \text{W}^{-1}$, being in quite good agreement. Considering previously established differences in temperatures and levels of contamination a small mismatch can be expected.

4.1.4 Summary and conclusions

In the current *in-situ* spectroscopic study, an industrial-scale plasma nitrocarburizing process with an active screen made of carbon-fibre-reinforced carbon was investigated using TDL and EC-QCL sources in the mid-infrared. This way the absolute concentrations of CH₄, C₂H₂, HCN, CO, and NH₃ were monitored in dependence on the total gas flow of the feed gas and the gas pressure in the reactor. To approximate common industrial conditions the plasma power at the active screen was regulated to maintain a steady temperature $T_{\text{set}} = 773$ K. The translational temperatures of the five molecular species were found to agree with the set temperature.

The plasma-chemical environment was strongly influenced by reaction products, which accounted for 50 to 30 % of the mole fraction at low and high total gas flows, respectively. Furthermore, the mole fraction of C₂H₂, HCN, and CO were found to be independent on the pressure, while for CH₄ and NH₃ the mole fractions increased with the pressure. Since all the concentrations of all detected species increased monotonously with the residence time, surface reactions should play a role in the production of the five species. HCN was the most abundant measured reaction product, ranging in the tens of percent in mole fraction and followed by C₂H₂ and NH₃, both in the high percent of mole fraction range. Since a stable plasma-chemical equilibrium was assumed, the production rates could be derived from the concentrations of the species. This allowed to distinguish CO from the other species, since its production rate is the only one to drop with the increase of flow. Further investigation then highlighted the linear decay of the CO production rate with the progressing active time of the plasma. The release of adsorbed oxygen-containing species from the large surface area of the carbon cathode during the plasma process is the likely source for oxygen in the formation of the CO molecule. The influence of the oxygen-contamination of the reactor was unique to the CO molecule and made conclusions about the dependency of its production rate on the total gas flow impossible.

However, for the production rates of the remaining four molecular species dependencies on the total gas flow trends could be established. The dominating production rate is of HCN with up to 18 slh, followed up by the production rate of NH₃, which increased from 0.25 to 7 slh with increasing total gas flow. While the production rates of all oxygen-free species increase monotonously with the total gas flow, only for NH₃ the production rate scales over proportionally. In addition, it shows the highest relative increase over the given range. For CH₄ a linear scaling was observed. However, HCN and C₂H₂ production rates flatten with higher total gas flows. This is mirrored in the carbon consumption rate also flattening with higher total gas flows, indicating a limit to the amount of carbon released by the active screen. The largest value for the carbon consumption rate in this experiment was approximately $\Phi_{\text{C}} \approx 12 \text{ g h}^{-1}$, which for an active screen with a mass of 30 kg allows for 2500 h of treatment time, assuming ideal circumstances. However, with the current data a reduction of screen size is considered for future measurement campaigns.

References

- [1] Puth A *et al.* 2020 *Plasma Sources Sci. Technol.* **29**(3) 035001
- [2] Dalke A *et al.* 2019 *Surf. Coat. Technol.* **357** 1060-1068
- [3] Casteletti L C, Neto A L, and Totten G E 2014 *Metallogr. Microstruct. Anal.* **3**:477-508
- [4] Bell T, Sun Y, and Suhadi A 2000 *Vacuum* **59** 14-23
- [5] Spies H-J 2013 *HTM J. Heat Treat. Mat.* **68** 86
- [6] Mittemeijer E J and Somers M A J 1997 *Surf. Eng.* **13** 483-497
- [7] Olzon-Dionysio M *et al.* 2010 *Surf. Coat. Technol.* **204** 3623-3628
- [8] Hubbard P *et al.* 2010 *Surf. Coat. Technol.* **204** 1145-1150
- [9] Georges J 1999 *US Patent Specification* 5,989,363
- [10] Gallo S C and Dong H 2009 *Surf. Coat. Technol.* **203** 3669
- [11] Ebersbach U *et al.* 1991 *HTM J. Heat Treat. Mat.* **46** 339
- [12] Skolek-Stefaniszyn E *et al.* 2010 *Vacuum* **85** 164-169
- [13] Yue W *et al.* 2011 *Tribol. Int.* **44** 2029-2034
- [14] Naeem M *et al.* 2017 *Materials Letters* **189** 213-216
- [15] Dong Y *et al.* 2011 *Acta Biomaterialia* **7** 447
- [16] Lebrun J P 2000 *US Patent Specification* 7,074,460 B2
- [17] Crespi Â E *et al.* 2011 *Mater. Lett.* **65** 2985-2988
- [18] Burlacov I *et al.* 2017 *HTM J. Heat Treat. Mat.* **72** 254-259
- [19] Hamann S *et al.* 2017 *J. Appl. Phys.* **121** 153301
- [20] Sproge L and Slycke J 1992 *HTM J. Heat Treat. Mat.* **9** 105-112
- [21] Lebrun J P 1996 *European Patent Specification* EP 0 801 142 B1 12.04
- [22] Burlacov I *et al.* 2018 *J. Appl. Phys.* **123** 233302
- [23] Hamann S *et al.* 2013 *Plasma Sources Sci. Technol.* **22** 055022
- [24] Puth A *et al.* 2018 *Plasma Sources Sci. Technol.* **27** 075017
- [25] Hamann S *et al.* 2015 *Rev. Sci. Instrum.* **86** 123503
- [26] Hamann S *et al.* 2015 *Contrib. Plasma Phys.* **55** 689-700
- [27] Lopatik D *et al.* 2012 *Meas. Sci. Technol.* **23** 115501
- [28] Röpcke J *et al.* 2000 *Rev. Sci. Instrum.* **71** 3706
- [29] Gordon I *et al.* 2017 *J. Quant. Spectrosc. Radiat. Transfer* **96** 139
- [30] Ba Y *et al.* 2013 *J. Quant. Spectrosc. Radiat. Transfer* **130** 62
- [31] Cottaz C *et al.* 2000 *J. Mol. Spectrosc.* **203** 285
- [32] Gomez L *et al.* 2010 *J. Quant. Spectrosc. Radiat. Transfer* **111** 2256

- [33] Maki A G *et al.* 2000 *J. Mol. Spectrosc.* **202** 67
- [34] Maki A G, Quapp W, and Klee S 2000 *J. Mol. Spectrosc.* **171** 420
- [35] Coxon J A and Hajigeorgiou P 2004 *J. Chem. Phys.* **121** 2992
- [36] Hamann S *et al.* 2015 *J. Phys. D: Appl. Phys.* **48** 34

4.2 Influence of H₂-N₂ gas composition on structure and properties of expanded austenite²

4.2.1 Introduction

Low temperature plasma assisted thermochemical diffusion treatments like plasma nitriding (PN) [1 – 4], plasma carburizing (PC) [5 – 7] and plasma nitrocarburizing (PNC) [8 – 10] are - besides well-established commercially available gaseous processes [11] - industrially applied to austenitic stainless steels. The use of these technologies meets the requirements of high surface hardness and improved wear behaviour without deteriorating the excellent corrosion resistance of austenitic stainless steels. Being independent on the applied method, the steel surface incorporates nitrogen or/and carbon forming a diffusion layer termed as “expanded austenite” [12, 13]. In case of conventional PNC a dual-layer structure consisting of nitrogen-expanded austenite γ_N on top of a carbon-expanded austenite γ_C is generated. Such a duplex layer combines the high hardness of γ_N being characteristic for PN layers and the smooth hardness gradient of γ_C at the layer-core interface being typical for PC layers. For conventional PNC the generation of these advantageous layer properties is only possible at well-defined but very constricted process windows especially regarding the approvable amount of carbon-containing gases [14, 15]. In the absence of an established process control of plasma-assisted nitrocarburizing processes the standard method is the control of the mass flow of the carbon-containing gases, e.g. methane (CH₄), based on traditional recipes combined with the operator’s experience. Therefore, even for a low percentage of addition of carbon-bearing gases, the risk of soot production is high. Besides the gas composition, the temperature control of the process has a great influence since the expanded austenite is metastable [16, 17]. If a technology-specific threshold temperature is exceeded the precipitation of chromium nitrides and/or carbides occurs within the expanded austenite [10]. The resulting undesired depletion of chromium in solid solution in austenite impairs the corrosion resistance [8]. Therefore, a precise temperature control is essential [18]. In the conventional DC systems mentioned at the beginning, the plasma discharge is located directly at the components to be treated providing the active species as well as heating up the components. Temperature limitations often arise due to common problems like the edge effect, the hollow cathode effect or a non-homogenous temperature distribution especially in case of components with different geometries [19, 20].

The active screen plasma nitriding (ASPN) technology has been developed to overcome the limitations of conventional plasma processes by relocating the glow discharge from the workload to an additionally introduced separate metal mesh screen, the active screen (AS), which surrounds the worktable and the components to be treated [19 – 22]. This approach is sometimes referred to as nitriding in “afterglow”, where energetic neutrals rather than charged species are responsible for the nitriding and/or carburizing effect [23 – 25]. Highly reactive gas species are produced in the AS plasma [26, 27]. However, a weak bias directly applied to the components to be treated is essential for large industrial-scale ASPN systems to achieve a reasonable nitriding response [25, 28]. This results in a second glow discharge directly at the workload with a typically lower plasma power. Recently, an additional technological advantage of the AS technology was reported by Burlacov and co-workers for the active screen plasma nitrocarburizing (ASPNC) technology [29, 30]. By adding different levels of carbon-containing gases to the H₂-N₂ plasma the specific contribution of the plasma discharge at the AS responsible for the control of the carburizing potential was identified. In particular, steels with higher Cr content demonstrated a significant nitriding/nitrocarburizing effect even without application of a bias, i.e. at floating potential. In early studies, Lebrun already reported on the importance of highly reactive gaseous products generated in the H₂-N₂ plasma with admixtures of even a few percentage of CH₄ [31]. The volatile and thermally stable CN-radicals generated in the plasma were found to be responsible for the beneficial effect of CH₄. Advanced plasma diagnostics methods applied during ASPN and ASPNC

² Published as: Dalke A, Burlacov I, Hamann S, **Puth A**, Böcker J, Spies H-J, Röpcke J, and Biermann H 2019 *Surf. Coat. Technol.* **357** 1060 – 1068

processes confirm the presence of highly reactive H-C-N bindings in the reaction gas of H₂-N₂ plasmas admixed with CH₄ or CO₂ [32]. In case of gaseous carbon-containing precursors, the production of reactive species results from the dissociation reactions between H₂, N₂, and carbon-bearing gases. These chemical reactions exhibit a very low reaction constant, and thus, the admixture of carbon-containing gases needs to be limited to avoid soot production or even not reproducible process results [33]. The use of an AS made of graphite as a solid carbon source for the deposition of CN layers on polymer substrates was proposed by Crespi and co-workers [34]. In industrial-scale nitriding devices current studies proved the feasibility of using solid carbon sources like carbon-fibre reinforced carbon (CFC) for conventional PNC and for ASPNC using a CFC AS [35 – 37], respectively. In a laboratory-scale reactor, Hamann *et al.* [38] have shown the very high reactivity of a CFC AS compared to a steel screen. As a major result, the net production rate of detectable highly reactive gases, in particular HCN and C₂H₂, was 30 and 70 times higher for the CFC AS than for the steel screen, respectively. Diagnostic investigations of the resulting process gas atmosphere of an ASPNC process using a CFC AS proved the correlation between H₂-N₂ precursor gas composition and resulting kind of reactive species and their concentrations in the laboratory-scale plasma nitriding monitoring reactor PLANIMOR [39].

In this work, the advantage of using a carbon AS for plasma nitrocarburizing of AISI 316L austenitic stainless steel was verified in an industrial-scale ASPNC unit. The effect of the variation of the nitrogen content from 0 % to 100 % nitrogen in the H₂-N₂ precursor gas composition on the expanded austenite layer properties, i.e. structure, thickness, hardness, and phase composition was investigated. Additionally, for comparable H₂-N₂ precursor gas compositions the achievements obtained in the laboratory-scale reactors [38, 39] have been verified by performing *in-situ* monitoring of the reaction gas by means of infrared laser absorption spectroscopy (IRLAS). Thus, a correlation between reaction gas composition, i.e. reactive gas species, and resulting layer formation and properties should provide a deeper understanding of the AS plasma nitrocarburizing process, and in turn predictability of treatment results.

4.2.2 Materials and methods

A representative austenitic stainless steel grade AISI 316L (wt.%: C0.05, Cr16.98, Ni11.39, Mo1.92, Mn1.54, Si0.33 and Fe balance) was used for the investigation. Specimens of 20 mm in diameter and 5 mm in thickness were machined from a commercial cylindrical bar. All samples were wet ground up to 1000 SiC paper grid, cleaned with ethanol in an ultrasonic bath and dried in hot air prior to ASPNC.

The ASPNC experiments were performed in an industrial-scale pulsed DC plasma system (15 kW main power supply working at 1 kHz 60 % duty cycle, worktable diameter $\varnothing_{WT} = 0.70$ m, reactor volume $V_r = 1$ m³). A separate Magpuls generator supplied a negative bias to the worktable and samples (up to 1.2 kW bias power supply working at 10 kHz 50% duty cycle). An AS made of CFC with 800 mm in diameter and 750 mm in height was placed in the centre of the reactor surrounding the workload (figure 1 a)). The process started by evacuating the reactor in 10 min down to a base pressure of 0.3 mbar. Subsequently, a hydrogen-argon gas mixture was introduced into the recipient and the main power supply was turned on to run the plasma at the CFC AS heating up the worktable, model probe, and specimen, respectively. After reaching a sample temperature of 373 K, measured with a thermocouple, a sputter-cleaning step at 0.6 kW bias power was set for 45 min heating up the samples to 623 K. Subsequently, the gas exchange to a hydrogen-nitrogen atmosphere was conducted, and the bias power was gradually increased up to a constant set point of 1.25 kW. The nitrogen content within the H₂-N₂ precursor gas varied between 0 % up to 100 % N₂ by changing the flow rates of the gases maintaining a total constant flow rate of 80 slh. At the end of the process, the recipient was evacuated and cooled down to room temperature under vacuum conditions.

In a first benchmark experiment, the measurement of the reaction gas, which is the resulting process gas composition inside the AS reactor, i.e. detection of molecular gas species and their absolute

concentrations, was conducted as a function of the H₂-N₂ precursor gas composition. The experiment was done at $T_{\text{set}} = 773$ K and $p = 3$ mbar applying a bias power at the workload of $P_{\text{Bias}} = 1.25$ kW and $P_{\text{Bias}} = 0$ kW, respectively. For this purpose two external-cavity quantum cascade lasers (EC-QCL) and the tuneable diode laser (TDL) based infrared multi-component acquisition system (IRMA [32]) were combined into a single IRLAS setup. The single beam path passed the reactor diagonally (figure 4.11 b)). This allows for line-integrated monitoring of the target species' infrared absorption features. The temperature of 773 K was chosen in order to compare to the results obtained at a laboratory setup [39]. Table 4.2 compiles the spectral positions, line strengths, and the estimated limits of detection of the molecular species used for the IRLAS measurements in the present study. The spectral positions and the identification of the absorption lines of the monitored molecular plasma components have been performed using well-documented reference gas spectra and an etalon of known free spectral range [40].

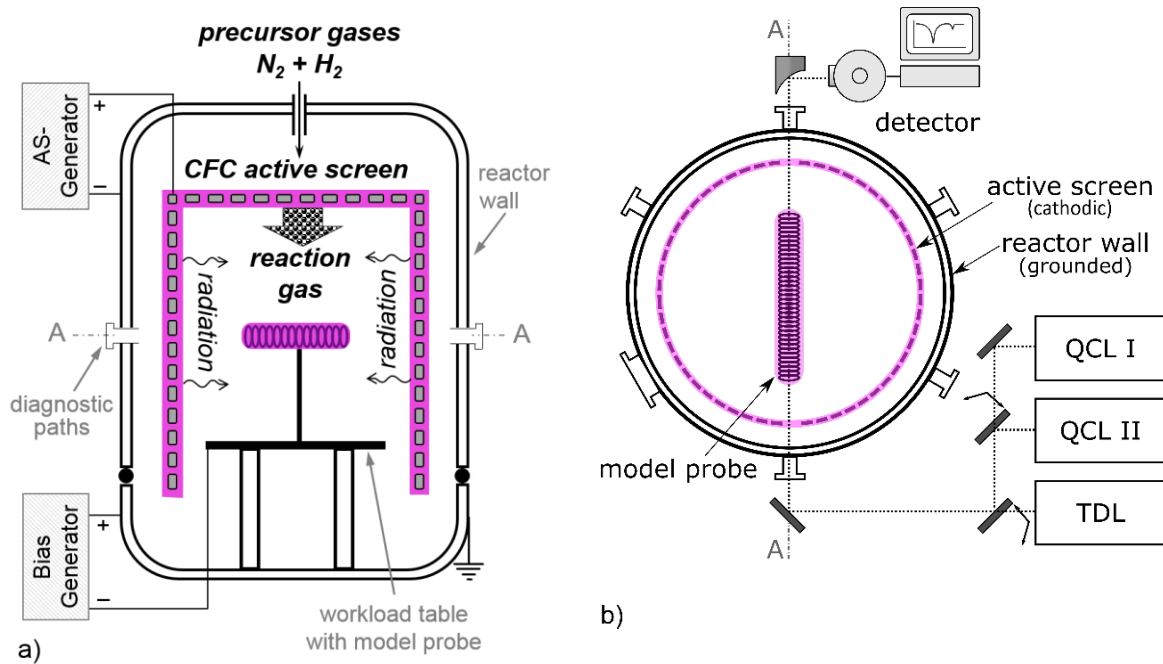


Figure 4.11 Schematic of the experimental setup in a) side and b) top view. EC-QCLs and the IRMA setup are denoted as QCL I, QCL II, and TDL, respectively and combined on a single beam path.

In a second test series, the ASPNC treatments of samples made of austenitic stainless steel were performed in order to generate thermochemically modified surface layers. Therefore, defined H₂-N₂ precursor gas compositions, which were verified out of to the plasma diagnostics benchmark experiment, were applied. Differing from the temperature of the benchmark experiment, the ASPNC treatments of AISI 316L were conducted at $T_{\text{set}} = 733$ K in order to prevent an unwanted CrN precipitation [16]. The treatment duration was kept constant for $t = 5$ h at a working pressure of $p = 3$ mbar. The treatment temperature and duration were selected according to common plasma carburizing treatment conditions because the presence of hydrocarbons in the process gas was always observed in preliminary tests. The H₂-N₂ precursor gas composition was varied starting from 0 % N₂ content to increasing N₂ ratios. It must be mentioned that an addition of 5 % (4 slh) of argon to the H₂-N₂ plasma was required to stabilize the discharge for gas compositions with high H₂ volume fractions (75 % – 100 % H₂). Further details concerning the experimental conditions and in-line electrical parameters are summarized in table 4.3.

Table 4.2 Species, spectral positions, and line strengths at room temperature, used for IRLAS measurements and respective estimated limits of detection using a combined TDLAS^(T) and QCLAS^(Q) spectrometer at the ASPNC reactor. Concentrations of species not shown in figure 4.12 were below their detection limit.

Species	Spectral position [cm ⁻¹]	Absorption line strength [cm ⁻¹ /(molecule cm ⁻²)]	Limit of detection [molecules cm ⁻³]	Ref.
CH ₃ ^(T)	606.1203	4.547·10 ⁻¹⁹	2·10 ¹²	[41, 42]
CH ₄ ^(Q)	1356.4868	1.784·10 ⁻²⁰	2·10 ¹³	[40]
CH ₄ ^(Q)	1356.5974	1.190·10 ⁻²⁰	2·10 ¹³	[40]
NH ₃ ^(Q)	1388.0552	2.726·10 ⁻²²	2·10 ¹⁴	[40]
NH ₃ ^(Q)	1767.5181	6.090·10 ⁻²¹	2·10 ¹³	[40]
C ₂ H ₂ ^(Q)	1356.8305	5.899·10 ⁻²²	5·10 ¹⁴	[40]
C ₂ H ₂ ^(Q)	1356.8881	8.920·10 ⁻²¹	2·10 ¹³	[40]
HCN ^(Q)	1356.9389	4.636·10 ⁻²³	4·10 ¹⁴	[40]
HCN ^(Q)	1388.3225	3.592·10 ⁻²²	1·10 ¹⁴	[40]
C ₂ H ₄ ^(T)	2993.8362	3.850·10 ⁻²¹	4·10 ¹³	[40]
C ₂ H ₆ ^(T)	2993.4710	1.496·10 ⁻²⁰	2·10 ¹²	[40]
C ₂ N ₂ ^(T)	2150.6668	1.13·10 ⁻²⁰	1·10 ¹³	[43]

Table 4.3 ASPNC process parameters: feed gas composition and electrical draw for AS and bias generator. Conditions: $T_{set} = 460$ °C, $t = 5$ h, $p = 4$ mbar.

N ₂ fraction [%]	Feed gases [slh]			AS parameters			Bias parameters		
	H ₂	N ₂	Ar	U _{AS} [V]	I _{AS} [A]	P _{AS} [W]	U _{Bias} [V]	I _{Bias} [A]	P _{Bias} [W]
0	80	0	4	254	21.8	5537	597	2.1	1265
10	72	8	4	281	17.6	4945	654	1.9	1249
25	60	20	4	282	16.2	4568	662	1.9	1248
50	40	40	0	282	16.3	4596	686	1.8	1249
75	20	60	0	280	16.3	4564	673	2.0	1252
90	8	72	0	268	15.8	4234	611	2.0	1253
100	0	0	0	318	11.6	3688	588	2.1	1255

All treated steel samples were analysed by glow discharge optical emission spectroscopy (GDOES) on a LECO SDP 750 spectrometer. The calibration Multi-Matrix method was used as a standard quantification procedure for the determination of concentration depth profiles. Cross-sections of specimens were metallographically polished and chemically etched with Beraha II etchant in order to examine the microstructure and to assess the generated layer thickness by using a Carl Zeiss Neophot 30 equipped with a JVC TK C1381CCD-camera and the Image C/A4i-Analysis software. Microhardness depth profile measurements were conducted at a LECO M-400G3 equipped with a Knoop micro indenter applying a load of 10 g. The phases present in the nitrocarburized layers were analysed by X-ray diffraction (XRD) with a SEIFERT-FPM URD6 (SEIFERT-FPM) diffractometer operating at $U = 40$ kV and $I = 30$ mA. A conventional θ - 2θ Bragg-Brentano symmetric configuration with CoK α ($\lambda = 1.78897$ Å) radiation was used applying a Bragg angle scanning ranging from 20° to 150° at a scan rate of 0.01°/min. The Co anode ensures a high penetration depth up to ~15 μ m at the highest diffraction angle, to obtain a high amount of information from the nitrocarburized layer.

4.2.3 Results

Process gas monitoring using IRLAS

Figure 4.12 shows the concentrations of CH₄, HCN, NH₃, and C₂H₂ determined by IRLAS as a function of the H₂-N₂ precursor gas mixture, with a bias power at the workload of (a) 1.25 kW and (b) 0 kW. Both experiments were conducted in separate measurement campaigns. Measurement of the spectral position of C₂H₂ was not possible for the biased case, due to unavailability of the laser source at the time. However, since C₂H₂ was already detected in various tests in a laboratory-scale reactor exhibiting concentrations as high as of CH₄, the existence of C₂H₂ was expected in an industrial-scale reactor as well, and successfully proven for AS experiments conducted without bias power (figure 2 b)) [38, 39].

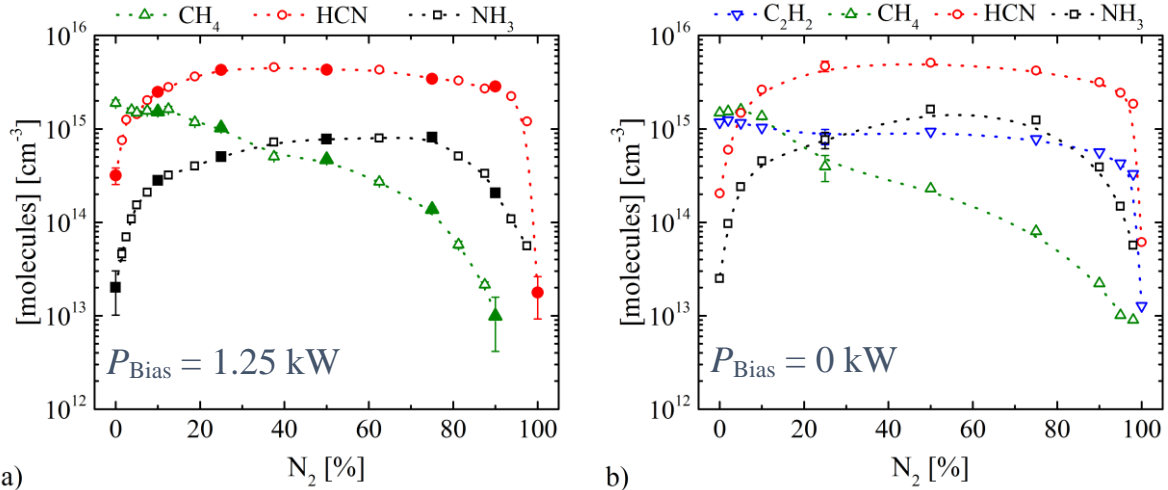


Figure 4.12 Concentrations of CH₄, HCN, NH₃, and C₂H₂ measured as functions of the nitrogen fraction in the H₂-N₂ feed gas mixture with an applied bias power of a) $P_{Bias} = 1.25$ kW and b) $P_{Bias} = 0$ kW. Conditions: $T_{set} = 773$ K, $p = 3$ mbar. Closed symbols in a) correspond to treated samples of AISI 316L.

By analysing the development of the molecular concentrations at variation of bias, a similar behaviour of the monitored reaction products CH₄, HCN, and NH₃ has been found both for the biased (figure 2 a)) and non-biased case (figure 2 b)), respectively. Due to this, for comparable H₂-N₂ ratios in the feed gas the resulting reaction gas composition and the existing gas species, respectively, are assumed similar for both test configurations and the results of the non-biased experiment can also be used for interpretation.

For a pure hydrogen precursor gas (0 % N₂) or at a strong hydrogen excess in the feed gas, respectively, the detected reaction products are dominated by hydrocarbons CH₄ and C₂H₂. This is in good agreement to earlier experiments at a laboratory-scale reactor, in which CH₄ and C₂H₂ were shown to be the most abundant hydrocarbons, with C₂H₄ at least by a factor of 5, C₂H₆ at least by a factor of 10 smaller than CH₄ [39]. The hydrocarbon species CH₄ and C₂H₂, respectively, decrease with an increase of nitrogen in the feed gas. With increasing nitrogen content, the concentration of CH₄ is continuously decreasing by at least two orders of magnitude. In contrast, C₂H₂ remains nearly constant up to 75 % nitrogen fraction in the precursor gas, sharply dropping by a factor of 50 when 100 % nitrogen is admixed.

In case of H₂-N₂ precursor gas mixtures containing of at least 5 % nitrogen, HCN and NH₃ are the dominant reaction products as previously shown in a laboratory-scale reactor [38, 39]. The admixture of up to 10 % nitrogen leads to a jump of the HCN concentration by a factor of nearly 10, and of the NH₃ concentration by a factor of 15, respectively. Being independent on the applied bias, for nitrogen fractions of 10 % to 95 % the curves of HCN show maximal values of $3 - 5 \cdot 10^{15}$ cm⁻³. In principle, the development of the NH₃ concentration is similar for nitrogen fractions between 10 % and 90 %, both for the biased and the non-biased mode. In both cases, maximal NH₃ concentrations are measured for nitrogen fractions between 50 % and 75 % N₂, i.e. $8 \cdot 10^{14}$ cm⁻³ for the biased, and $1.5 \cdot 10^{15}$ cm⁻³ for the

non-biased condition. Exceeding 75 % nitrogen in the feed gas yields an abrupt decrease of the NH_3 concentration both for biased and non-biased process conditions.

For a pure nitrogen precursor gas (100 % N_2) or at a strong nitrogen excess in the feed gas the detected concentrations of the reaction products drop altogether. Only the detection of HCN ($2\text{-}6 \cdot 10^{13} \text{ cm}^{-3}$) and C_2H_2 ($1 \cdot 10^{13} \text{ cm}^{-3}$) was possible.

Contrary to the steep drop of the concentration of NH_3 at 80 % nitrogen, the concentration of C_2H_2 remains at high values for nitrogen fractions between 80 % and 98 %. Comparing the behaviour of the HCN and the NH_3 concentrations as functions of the nitrogen fraction in the feed gas it can be seen that the concentration ratio of NH_3 and HCN is close to constant for all $\text{H}_2\text{-N}_2$ ratios. Contrary to this, the ratio of CH_4 to C_2H_2 concentrations monotonously drops with an increase of the nitrogen fraction in the feed gas, only failing to do so at the previously mentioned extreme feed gas compositions.

Nitride layer structure and properties of nitrocarburized AISI 316L

Figure 4.13 shows the concentration depth profiles of nitrogen and carbon of the near-surface area after applying ASPNC using a CFC screen under variation of the $\text{H}_2\text{-N}_2$ precursor gas composition given in table 4.2.

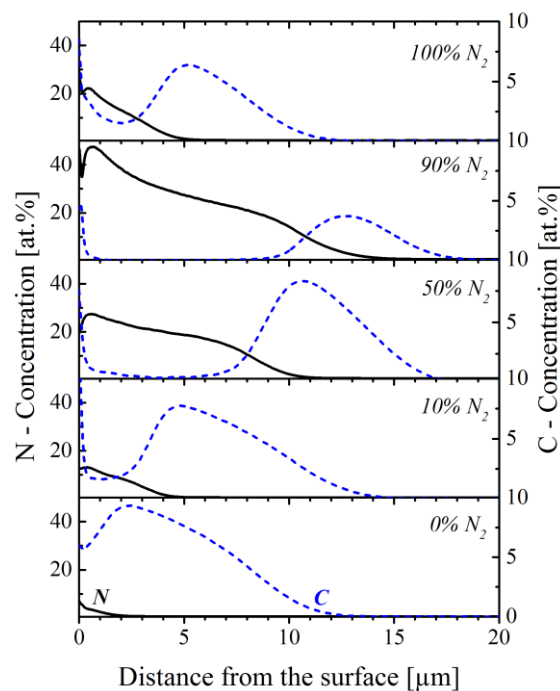


Figure 4.13 GDOES concentration depth profiles of nitrogen (solid line, left axis) and of carbon (dashed line, right axis) in the expanded layer measured in the samples treated under variation of the N_2 fraction, given in percentage of the total $\text{H}_2\text{+N}_2$ concentration.

The application of a pure H_2 precursor gas (0 % N_2) results in the generation of a single carbon-expanded austenite layer γ_{C} . The maximum carbon concentration obtained in the γ_{C} layer reaches 9 at.%. The slight nitrogen content detected near the surface is attributed to reactor contamination already reported by Burlacov et al. [33].

The addition of nitrogen to the $\text{H}_2\text{-N}_2$ precursor gas leads to the formation of a dual-structure. Generally, the structure of nitrogen-expanded and carbon-expanded austenite layers generated by means of ASPNC applying an AS made of CFC exhibits a composition being typical for nitrocarburized layers on austenitic stainless steels [8]. The carbon-expanded layer γ_{C} is located underneath the nitrogen-expanded layer γ_{N} . This distribution results due to the modification of the activity of carbon and nitrogen with their

respective concentration in the layer [18]. According to this, nitrogen significantly enhances the activity of carbon in γ_N resulting in an uphill diffusion of C already reported by Kucera *et al.* [44]. With increasing N_2 content up to 50 % in the H_2 - N_2 precursor gas, the diffusion depth of nitrogen increases continuously without changing the thickness of the carbon-expanded layer. The maximal diffusion depth of both nitrogen and carbon is reached for N_2 fractions between 50 % up to 90 % N_2 in the N_2 - H_2 precursor gas mixture. For these conditions a total layer thickness of about 15 μm results. In the above-mentioned range of N_2 addition, the nitrogen-expanded layer is successively enriched with nitrogen accompanied by the reduction of the carbon uptake in the dual layer. Notably, the highest nitrogen enrichment of the γ_N layer near the surface yields a value of about 47 at.% obtained after the treatment with 90 % N_2 in the N_2 - H_2 precursor gas. This value exceeds the one reported by Christiansen [45] for gaseous nitriding of AISI 316L austenitic stainless steel, specifying 38 at.% as the maximum nitrogen concentration dissolved in the octahedral sites of the austenitic fcc-lattice. Since the maximum of 38 at.% N sets the upper limit for what is possible in a homogeneous stress-free nitrogen expanded austenite foil, the concentration of nitrogen detected by means of GDOES originates elsewhere due to other effects, i.e. formation of additional phases near the surface.

The changeover of the precursor gas from a N_2 - H_2 mixture to pure nitrogen (100 % N_2) shows a significant impact both on the electrical discharge by a strong reduction of the plasma power (see table 4.3) and on the resulting total layer thickness. Remarkably, the thickness of the γ_N layer obtained after the treatment in a pure nitrogen atmosphere is only one third of that generated in a high nitrogen – low hydrogen precursor gas mixture (90 % N_2 + 10 % H_2), and simultaneously, the carbon concentration within the carbon-expanded layer γ_C increases.

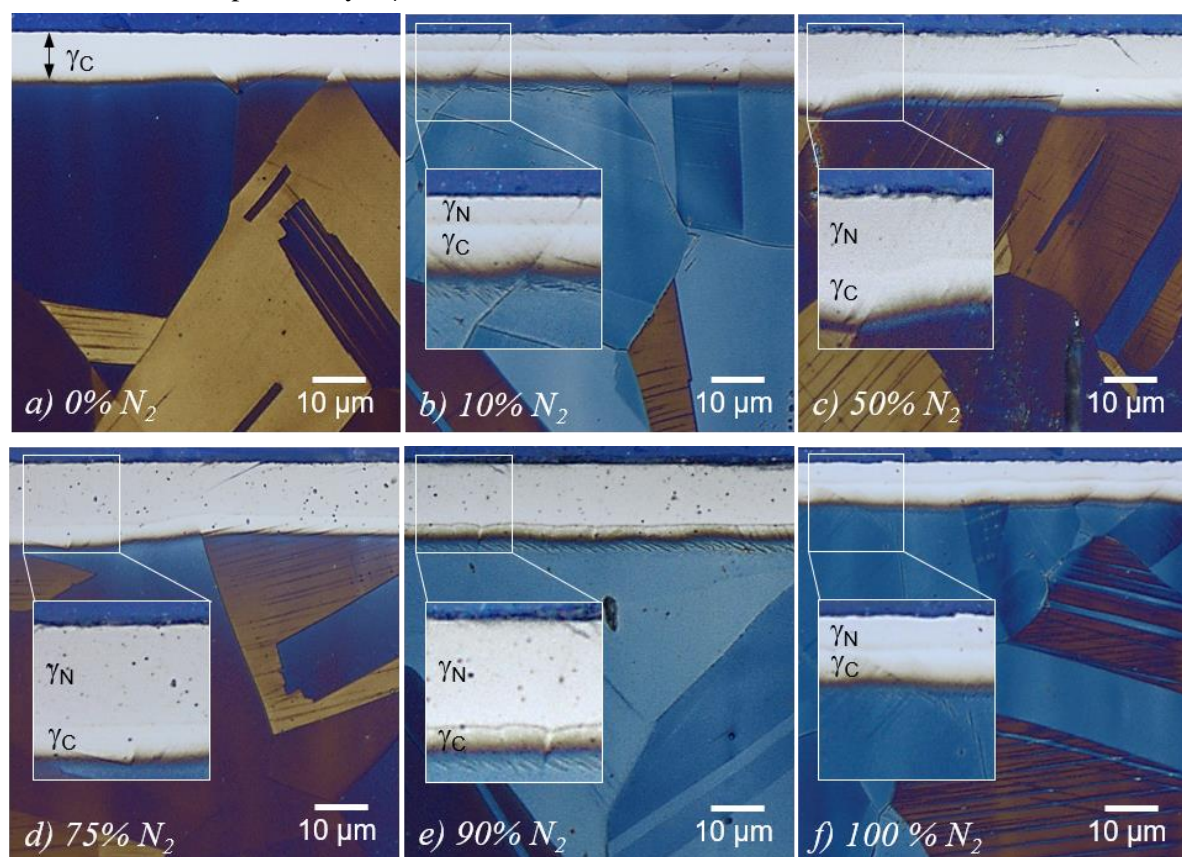


Figure 4.14 Cross-sectional light optical micrographs of the expanded austenite layer of selected specimens treated different N_2 fractions, given in percentage of the total H_2+N_2 concentration. Etchant: Berah II reagent.

Light optical micrographs of cross-sections from samples treated at different N_2 - H_2 precursor gas mixtures are depicted in figure 4.14. The expanded austenite layer is visible as a “white layer” due to a

different etching reactivity compared to the substrate. The duplex structure of the expanded austenite layer consisting of nitrogen-expanded γ_N and carbon-expanded γ_C layer becomes visible after etching with Beraha II reagent. In case of a pure H_2 precursor gas (figure 4.14 a)) the single γ_C layer is observable. In contrast, by applying N_2 - H_2 precursor gas mixtures the typical dual-phase layer is formed and the two expanded layers γ_N and γ_C are separately visible (figure 4.14 b) – f)). The thickness of each layer depends strongly on the precursor gas composition and is consistent with the value estimated from GDOES analysis, c.f. figure 4.13. No CrN precipitations are visible in the modified layer except at some grain boundaries in the case of N_2 fractions exceeding 50 % in the feed gas (figure 4.14 c) – f)).

Figure 4.15 shows the evolution of thickness of both the γ_N and γ_C layer as well as the entire thickness of the expanded layer ($\gamma_N + \gamma_C$) as a function of the N_2 fraction in the N_2 - H_2 precursor gas. The thickness values are estimated on basis of the GDOES profiles (figure 4.13) and of light optical measurement (figure 4.14). By analysing the GDOES profiles, the thickness of the nitrogen-expanded layer γ_N is defined at the depth where nitrogen and carbon concentrations are equal, which is around 4 – 5 at.%. The thickness of the entire expanded layer ($\gamma_N + \gamma_C$) is defined at a carbon threshold concentration of 2 at.% C. The difference of these two values gives the thickness of the carbon-expanded layer γ_C .

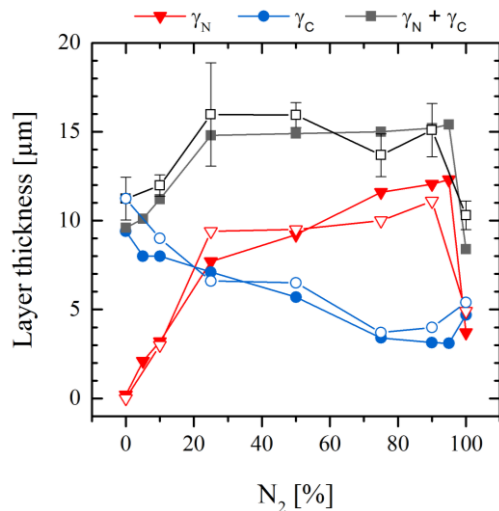


Figure 4.15 Thickness of nitrogen-expanded γ_N , carbon-expanded layers γ_C , and entire layer thickness $\gamma_N + \gamma_C$ as functions of the N_2 fraction, given in percentage of the total $H_2 + N_2$ concentration. Measured by cross section (open) and GDOES profiles (closed symbols).

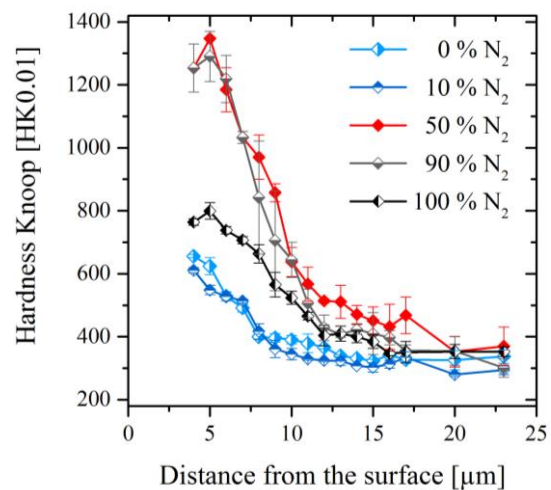


Figure 4.16 Microhardness depth profiles measured in the nitrocarburized layers as a function of N_2 fraction, given in percentage of the total $H_2 + N_2$ concentration.

Microhardness-depth profiles measured on cross-sections of samples treated at selected N_2 fractions in the N_2 - H_2 precursor gas are shown in figure 4.16. The resulting hardness profile depends on the N_2 - H_2 ratio of the precursor gas composition. For the condition of a pure hydrogen feed gas, in the carbon-expanded layer γ_C a value of about 600 HK 0.01 is measured and a smooth hardness gradient to the substrate is generated, a typical feature of carburized layers on austenitic stainless steel [5 – 7]. A nitrogen fraction in the N_2 - H_2 precursor gas of 50 % to 90 % correlates with an increase in hardness to values in the range of 1250 – 1350 HK 0.01. The sample treated in 100 % N_2 exhibits a thin expanded layer and a sufficient hardness of 800 HK 0.01. This hardness increase is about 30 % higher compared to the condition of using only hydrogen as precursor gas, which can be explained with the simultaneous incorporation of both carbon and nitrogen into the austenite solid solution. Moreover, the thickness of the hardened cases is in good agreement with the diffusion profiles of figure 4.13 and the microstructure presented in figure 4.14.

The diffractograms of the base material as well as the modified layers obtained after the treatments with different H_2 - N_2 ratios of the precursor gas are shown in figure 4.17. Although the X-ray diffraction

analysis was performed for 2θ angles ranging between 20° and 150° , only the diffraction peaks obtained between 43° and 62° are shown for clarity. For the untreated AISI 316L austenitic substrate two strong peaks are obtained, corresponding to fcc $\gamma(111)$ and $\gamma(200)$. The variation of the X-ray diffraction patterns with H_2-N_2 ratio of the precursor gas mixture can be seen clearly. For a pure hydrogen precursor gas, i.e. without nitrogen addition, diffraction peaks similar to the ones obtained for the untreated substrate are measured. However, compared with the pattern of the substrate austenite, the two corresponding diffraction peaks from the treated specimen are shifted to lower angles, indicating expansion of the initial austenitic fcc lattice. These peaks are attributed to the formation of carbon-expanded austenite γ_C due to the enrichment of the near-surface region with carbon clearly visible in the GDOES profile in figure 4.13. By adding nitrogen to the hydrogen precursor gas the two identifying main peaks remain visible for all N_2-H_2 ratios of the precursor gas mixtures applied, but their characteristics change in dependence of N_2 content. For a low nitrogen fraction of 10 % N_2 the detected peaks are further shifted to lower angles and get concurrently broadened, indicating the increasing expansion of the austenite lattice and the presence of new phases. Since a carbon- and nitrogen-rich atmosphere is given, austenite expands for two reasons, the incorporation of carbon and the incorporation of nitrogen. These two different species lead to different expansion degrees being visible as peak splitting. With increasing N_2 fraction in the precursor gas, the expanded austenite peaks are characterized by asymmetric broadening to the right side, corresponding to the high angle side of the peak. This effect is related to the increasing nitrogen concentration over the information depth of the probing X-rays, c.f. GDOES profiles in figure 4.13. The higher expansibility for the (200)-direction compared to the (111)-direction typically results from the crystallographic anisotropy of the Young's modulus where $E_{200} < E_{111}$ [46]. This is directly related to the occurrence of compressive stresses in the expanded austenite layer being constrained by the substrate. Hence, the anisotropy leads to hkl-dependent peak shifts. However, further increase of nitrogen concentration in the N_2-H_2 precursor gas results in an increased diffusion depth in the austenite both of carbon and of nitrogen, as visible in the GDOES profiles shown in figure 4.13. As a consequence, the expansion due to carbon exceeds the penetration depth of the X-rays for a N_2 fraction higher than 50 vol.%, and only the reflection of nitrogen-expanded austenite γ_N is measurable. For nitrogen fractions exceeding 90 % N_2 a small peak near $2\theta = 48^\circ$ is likely related to ϵ -carbonitride phase precipitated in the nitrogen-rich zone close to the surface [47]. This peak has been detected on specimens treated with nitrogen-rich precursor gas mixtures exceeding 75 % N_2 . However, in the case of such high nitrogen contents peaks related to the presence of CrN were not clearly measured.

ASPNC treatment using a pure nitrogen precursor gas results in a lower lattice expansion, indicated by the two characteristic peaks. Moreover, separated peaks related to nitrogen-expanded austenite γ_N and carbon-expanded austenite γ_C are detected again, because the entire thickness of the expanded layers did not exceed the penetration depth of the X-rays.

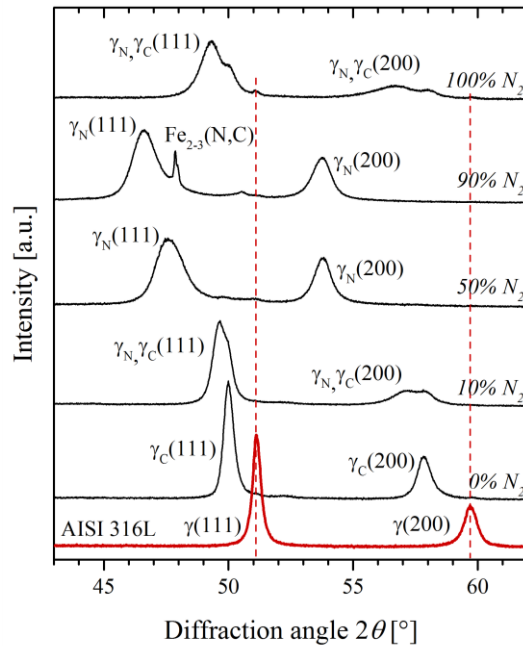


Figure 4.17 X-ray diffraction patterns of the nitrogen- and carbon-expanded austenite for samples treated under different N_2 fractions, given in percentage of the total H_2+N_2 concentration. Untreated control in red. Baselines offset for clarity.

3.2.4 Discussion

The use of an AS made of CFC enables the *in-situ* generation of highly reactive gases, in particular unsaturated hydrocarbons, directly in the reactor chamber because of the interaction of H_2-N_2 plasma and carbon material [38, 39]. This phenomenon is generally denoted as chemical sputtering, which results in a much higher generation rate of volatile products compared to physical sputtering [48]. A characteristic signature of chemical sputtering is the very low threshold ion energy for initiating the production of chemical species being only a few eV compared to about 100 eV in case of physical sputtering. The interactions between carbon targets and energetic particles, e.g. ions or neutral atoms, has been in the focus of fusion research for a long time [49-53]. A detailed model describing the mechanism of chemical sputtering was proposed by Hopf and Jacob [49]. Thereby carbon-carbon bonds get broken by impinging particles and are subsequently passivated by reactive hydrogen forming volatile hydrocarbons. Subsequently, the hydrocarbons diffuse to the surface and desorb. The main reaction products resulting due to the interaction of a hydrogen plasma and carbon surface, e.g. CH_4 and higher hydrocarbons C_xH_y with $x \geq 2$, were systematically investigated by further research groups [50].

The admixture of other reactive gases to the hydrogen plasma, for example nitrogen, increases the complexity of the reaction products, and the formation of new volatile species, e.g. HCN, CN, and C_2N_2 , caused by chemical sputtering was reported [51 – 53].

Recently, a method of gaseous nitrocarburizing of stainless steels in the atmosphere of unsaturated hydrocarbons and CN-compounds has been patented [54]. The reported reactive gaseous species produced through thermal pyrolysis of complex organic compounds include free radicals and/or compounds containing both C and N, e.g. HCN. The effectiveness of this process relies on the specific feature of these gaseous compounds both to activate or de-passivate the steel surface and to provide simultaneously nitrogen and carbon for surface hardening [11].

Combining the above-described findings facilitates the interpretation of the outcome of the presented spectroscopic investigation and stainless steel surface modification.

The results of the TDLAS experiments performed in an industrial-scale ASPNC system align with those obtained in the laboratory reactor examining the influence of H₂-N₂ precursor gas composition on resulting reaction gas composition [39]. In case of thermochemical diffusion treatments, the understanding of the interaction between reactive gas species and materials' surface is essential to gain optimal process results.

In said previous investigations the hydrocarbon concentrations showed similar behaviour, with CH₄ and C₂H₂ being most abundant [38, 39]. In our present investigation, a hydrogen fraction in the feed gas in excess of 90 % leads to hydrocarbon concentrations considerably higher compared to HCN and NH₃. The carbon uptake into the stainless steel surface controls the layer structure causing a carbon-expanded austenite γ_C only (figure 4.14 a)), and the γ_C -layer predominates the layer thickness within the dual-layer structure in case of such low nitrogen fractions (figure 4.15), respectively.

Increasing the nitrogen fraction in the precursor gas up to 20 % to 95 % N₂ HCN and NH₃ are most abundant with their maximal values in concentration at around 50 % of nitrogen fraction, see figure 4.12. The nitrocarburizing treatment using a precursor gas composition of equal N₂-H₂ fraction produced an expanded layer structure consisting of both well-developed nitrogen-expanded and carbon-expanded austenite sublayers (figure 4.14 c)). A further increase of the nitrogen fraction in the precursor gas of 50 % up to 90 % N₂ strongly decreased the thickness of the carbon-expanded layer, whereas both the nitrogen concentration in and the thickness of the nitrogen-expanded layer increased (figures 4.13 and 4.15, respectively). It is interesting to note that for a precursor gas mixture with a nitrogen content of 90 % to 95 % N₂ the resulting reaction gas is dominated by HCN species maintaining almost 30 % from its maximum, whereas the concentration of NH₃ dropped to one tenth of its highest level. The outcome of such a HCN-rich reaction gas is a high nitrogen supersaturation of the nitrogen-expanded austenite (figure 4.13) possibly causing the precipitation of additional phases on top of the γ_N layer, e.g. iron nitrides or carbonitrides. An indication for this assumption is the peak at 48° in the XRD pattern at a content of 90 % nitrogen in the precursor gas (figure 4.17). From this result, one can deduce that HCN contributes mostly to the nitrogen uptake on the austenitic surface rather than NH₃.

With increasing nitrogen fraction in the precursor gas the concentrations of hydrocarbons (CH₄ and C₂H₂) were monotonously reduced, which in turn is reflected in the reduction in thickness of the carbon-expanded layer (figure 4.15).

A reaction gas resulting from a precursor gas with pure nitrogen (100% N₂) differs considerably from that obtained by adding few percent of hydrogen. The presence of hydrogen in the precursor gas is essential for generating H-C-N species. With no admixture of hydrogen, the HCN concentration drops drastically by almost two orders of magnitude from its previous value (see figure 2 a)), and is probably sourced solely by residual hydrogen remaining inside the carbon AS. Pardanaud *et al.* reported an H-release from plasma-deposited hydrogenated amorphous carbon films at a temperature of 450 °C [55]. Thus this effect is assumed to occur in the case of carbon AS as well especially due to the experimental sequence starting with pure hydrogen precursor gas. In a pure nitrogen precursor gas the concentrations of most other species, in particular of hydrocarbons, were below their detection limits. The anomalous structure of the expanded layer produced with pure nitrogen precursor gas could be explained by a change of sputtering mode from chemical sputtering, where hydrogen is contributing, back to physical sputtering performed by nitrogen ions and energetic particles without the participation of hydrogen. Nevertheless, in a model reactor applying pure nitrogen plasma a low concentration of C₂N₂ species was spectroscopically registered that could be contributing to both the nitrogen and carbon uptake into the steel surface [39]. However, in the industrial-scale ASPNC reactor the presence of such a gas species has not been verified yet.

The concept of a solid carbon source applied to the AS technology has been proven to work in the industrial-scale ASPNC system. A technological advantage of the application of the AS made of carbon is the avoidance of the use of external gaseous carbon-bearing precursors. Moreover, a smooth variation

of the ratio of the N_2 - H_2 precursor gases considerably influences the composition of the generated reaction gas, which in turn determines the rate of the uptake reactions in the steel surface both for nitrogen and for carbon. In particular, a relation between the concentrations of HCN and hydrocarbons (CH_4 and C_2H_2) in the resulting reaction gas was found to be important and representative to control the structure and properties of the expanded austenite layer obtained after nitrocarburizing.

Finally, a relation between the concentration of HCN and the concentrations of major hydrocarbons in the reaction gas, such as CH_4 and C_2H_2 , could have a control function over the structure of the modified layer on austenitic stainless steel. A detailed study of the interaction mechanism of any certain species with the metallic surface under such conditions will be a focus of further investigations.

4.2.5 Conclusions

A novel plasma-assisted method based on the active screen technology using carbon-fibre reinforced carbon (CFC) as active screen material instead of conventional steel has been applied in an industrial-scale AS system for thermochemical surface treatment of austenitic stainless steel AISI 316L. A new concept of the use of a solid-carbon-source for generating a reaction gas consisting predominantly of unsaturated hydrocarbons, e.g. CH_4 and C_2H_2 , HCN, and NH_3 has been realized. The results of the conducted spectroscopic investigations in the industrial-scale ASPNC reactor confirmed those obtained in spectroscopic studies performed in a laboratory-scale setup. The current study demonstrated that the interaction of a CFC-AS in a H_2 - N_2 plasma results in a reaction gas that provided significant structural modifications in nitrocarburized layers of austenitic stainless steel. The development of nitrogen-expanded and carbon-expanded austenite sublayers was verified. A variation of the N_2 - H_2 precursor gas composition in a wide range allowed a development of the expanded layer with a defined structure. A mono-phase carbon-expanded layer was produced using pure hydrogen precursor gas, whereas a predominant structure of nitrogen-expanded austenite was generated using a precursor gas with 90 – 95 % nitrogen fraction.

An advantage of the nitrocarburizing treatment over the pure nitriding or carburizing treatment is the possibility to design a required case hardness gradient using a two-layer structure of the expanded layer (γ_N and γ_C) with a superposition of their concentrations and therefore of their hardness profiles. A variation of process parameters, in particular the composition of the N_2 - H_2 precursor gas, can be used for effective control of the expanded layer structure.

The composition of the generated reaction gas was monitored *in-situ* by laser absorption spectroscopy in the infrared (IRLAS). External-cavity quantum cascade lasers (EC-QCL) as well as tuneable diode lasers (TDL) were used to monitor spectral positions associated with transitions of CH_4 , C_2H_2 , HCN, and NH_3 . A relation of the concentrations of HCN and of hydrocarbons, e.g. CH_4 and C_2H_2 , measured in the reaction gas for different N_2 - H_2 precursor gas compositions correlates with the structural changes of the steel emphasizing the importance of the HCN species for nitrogen uptake in the austenitic steel. Both advanced spectroscopic methods can thus be used for the purpose of process control.

References

- [1] Zhang Z L and Bell T 1985 *Surf. Eng.* **1** 131-136
- [2] Kaestner P *et al.* 2008 *Surf. Coat. Technol.* **203** 897-900
- [3] De Las Heras E *et al.* 2017 *Surf. Coat. Technol.* **313** 47-54
- [4] Braceras I *et al.* 2018 *Surf. Coat. Technol.* **355** 116-122
- [5] Sun Y, Li X, and Bell T 1999 *Surf. Eng.* **15** 49-54
- [6] Souza R M *et al.* 2009 *Surf. Coat. Technol.* **204** 1102-1105
- [7] Molleja J G *et al.* 2010 *Surf. Coat. Technol.* **204** 3750-3759
- [8] Spies H-J, Eckstein C, and Zimdars 2002 *HTM Z. Werkst. Waermebeh. Fertigung* **57** 409-414
- [9] Cheng Z *et al.* 2005 *Surf. Coat. Technol.* **191** 195-200
- [10] Sun Y 2010 *Surf. Eng.* **26** 114-122
- [11] Sommers M A J and Christiansen T L, *Gaseous processes for low temperature surface hardening of stainless steel*, in: Mittemeijer E J, Somers M A J (Eds.), *Thermochemical Surface Engineering of Steels*, Elsevier; 2015, pp. 581-614
- [12] Dong H 2010 *Inter. Mater. Rev.* **55**:2 65-98
- [13] Casteletti L C, Neto A L, and Totten G E 2014 *Metallogr. Microstruct. Anal.* **3** 477-508
- [14] Chen F-S and Chang C-N 2003 *Surf. Coat. Technol.* **173** 9-18
- [15] Sun Y and Haruman E 2006 *Vacuum* **81** 114-119
- [16] Li X Y 2001 *Surf. Eng.* **17** 147-152
- [17] Djellal R *et al.* 2017 *Surf. Coat. Technol.* **325** 533-538
- [18] Lebrun J P, *Applications of low-temperature surface hardening of stainless steels*, in: Mittemeijer E J, Somers M A J (Eds.), *Thermochemical Surface Engineering of Steels*, Elsevier; 2015, pp. 615-632
- [19] Georges J 1999 *US Patent Specification* 5,989,363
- [20] Georges J 2001 *Heat Treat. Metals.* **28** 33-37
- [21] Li C X, Bell T, and Dong H 2002 *Surf. Eng.* **18** 174-181
- [22] Li C X 2010 *Surf. Eng.* **26** 135-141
- [23] Ricard A 1993 *Surf. Coat. Technol.* **59** 67-76
- [24] Hubbard P *et al.* 2010 *Surf. Coat. Technol.* **204** 1145-1150
- [25] Hubbard P *et al.* 2010 *Surf. Coat. Technol.* **204** 1151-1157
- [26] Jaoul C *et al.* 2006 *Thin Solid Films* **506-507** 163-167
- [27] Jaoul C *et al.* 2006 *Appl. Surf. Sci.* **252** 8360-8366
- [28] Burlacov I *et al.* 2014 *J. Int. Heat Treat. Surf. Eng.* **8** 139-143
- [29] Spies H-J *et al.* 2014 *J. Int. Heat Treat. Surf. Eng.* **8** 94-106

- [30] Burlacov I *et al.* 2016 *HTM J. Heat Treat. Mat.* **71** 141-147
- [31] Lebrun J P 1996 *EU Patent Specification* 0 801 142 B1, 12.04.
- [32] Hamann S *et al.* 2013 *Plasma Sources Sci. Technol.* **22** 055022
- [33] Burlacov I *et al.* 2018 *J. Appl. Phys.* **123** 233302
- [34] Crespi A E *et al.* 2011 *Mater. Lett.* **65** 2985-2988
- [35] Dalke A *et al.* 2018 *Vacuum* **149** 146-149
- [36] Burlacov I *et al.* 2017 *HTM J. Heat Treat. Mat.* **72** 254-259
- [37] Dalke A *et al.* 2018 *HTM J. Heat Treat. Mat.* **73** 246-257
- [38] Hamann S *et al.* 2017 *J. Appl. Phys.* **121** 153301
- [39] Puth A *et al.* 2018 *Plasma Sources Sci. Technol.* **27** 075017
- [40] Rothmann L S *et al.* 2013 *J. Quant. Spectros. Radia. Transfer* **130** 4-50
- [41] Stancu G D, Röpcke J, and Davies P B 2005 *J. Chem. Phys.* **122** 014306
- [42] Stancu G D *et al.* 2005 *Contrib. Plasma Phys.* **45** 358-368
- [43] Jacquinet-Husson N *et al.* 2016 *J. Mol. Spectrosc.* **327** 31-72
- [44] Kucera J *et al.* 1996 *Metall. Mater.* **34** 336-348
- [45] Christiansen T and Somers M A J 2006 *Metall. Mater. Trans. A* **37** 675-682
- [46] Nye J F, *Physical Properties of Crystals*, Oxford University Press (1985)
- [47] Sun Y, Li X Y, and Bell T 1999 *J. Mater. Sci.* **34** 4793-4802
- [48] Jacob W and Roth J, *Chemical sputtering*, in: *Sputtering by Particle Bombardment. Experiments and Computer Calculations from Threshold to MeV Energies*, Springer; 2007, pp. 329-399
- [49] Hopf C and Jacob W 2005 *J. Nucl. Mater.* **342** 141-147
- [50] Hopf C, von Keudell A, and Jacob W 2003 *J. Appl. Phys.* **94** 2373
- [51] Jacob W, Hopf C, and Schlüter M 2005 *Appl. Phys. Lett.* **86** 204103
- [52] Jacob W, Hopf C, and Schlüter M 2006 *Phys. Scr.* **2006** 32-36
- [53] Schlüter M, Hopf C, and Jacob W 2008 *New J. Phys.* **10** 053037
- [54] Christiansen T L 2011 *EU Patent Specification* 2278038 A1, 26.01.
- [55] Pardanaud C *et al.* 2013 *Diam. Relat. Mater.* **37** 92-96

4.3 Effects of admixed oxygen-containing species in ASPNC processes³

4.3.1 Introduction

As chapters 4.1 and 4.2 have shown, the use of an AS made of CFC results in high concentrations of carbon-containing species and concerning the nitrocarburizing treatment a high carburizing potential. In order to control the level of carburizing, the admixture of oxygen-containing species to the feed gas was investigated, in particular O₂ and CO₂. While CO₂ is an established admixture in industrial ASPNC [1 – 3], the use of molecular oxygen was previously reserved for post-treatment oxidation of an initially plasma nitrocarburized workload [3 – 5]. The well-known affinity of oxygen to hydrogen, carbon, and nitrogen can result in a large number of stable oxidative products, such as H₂O, CO and CO₂, and some nitrogen oxides, N_xO_y. Accordingly, the underlying plasma chemistry is rather complex, with plasma-kinetic models typically excluding at least one of the four mentioned elements [6 – 10]. By use of O₂ or CO₂ in an ASPNC process, the first expected effect was a reduction in the concentrations of the hydrocarbons and HCN, allowing for partial control of the carburizing potential. Secondly, an increased consumption of the solid carbon AS was expected, resulting in increased concentrations of CO and CO₂ and presenting a considerable drawback for any practical application of this setup. Finally, the time-independent effect of leakage and time-dependent effect of wall-attachment of oxygen-containing species was expected to be lessened.

In this set of experiments, the effects of both CO₂ and O₂ admixtures on the plasma-chemical condition of an ASPNC process were investigated. While fraction of the oxygen-containing admixture was stepwise increased from 0 to 10 % of the total gas flow, the fraction of nitrogen was correspondingly decreased from 90 to 80 % to maintain a constant hydrogen fraction of 10 % in the constant total gas flow of 80 slh. The concentrations of the seven observed molecular species CH₄, C₂H₂, HCN, NH₃, CO, CO₂, and H₂O were measured and respective production rates derived. Finally, this results in an analysis of e.g. carbon consumption rate as function of the oxygen-containing admixed fraction.

In a separate set of experiments, the development in time of concentrations were investigated for the full treatment time of 8 h typical for nitrocarburizing treatments, with and without admixture of 6 % oxygen in the total gas flow. As well in an ASPNC process with strong nitrogen excess, the oxygen-contamination of the reactor was studied by the trend in time of the CO concentration and compared with trend in a nitrocarburizing treatment with substantial O₂ admixture.

4.3.2 Experimental

Descriptions of the reactor and the laser spectroscopic setup are given in sections 4.1.2 and 4.2.2. The process temperature, measured with a thermocouple placed at the sample workload, was maintained at $T_{\text{set}} = 773$ K for all experimental settings, at a stable AS plasma power of 7.1 kW and no use of bias. Further, the pressure p and the total gas flow Φ_{Total} were set to 3 mbar and 80 slh, respectively.

In table 4.4 a list of detected species and with their spectral positions, line strengths and limits of detection are compiled. The superscript Q or T designate a measurement with an EC-QCL or a TDL source, respectively. If multiple transitions were available for a single species, the concentration with the lowest relative error was assumed to be representative for the species.

An ASPNC treatment of material samples and concurrent time-dependent LAS measurement was conducted for both an admixture of 6 % O₂ relative to the total flow and no admixture. For the initial heating of the reactor, a hydrogen flow of $\Phi_{\text{H}_2} = 30$ slh and an argon flow of $\Phi_{\text{Ar}} = 10$ slh were set in

³ Parts of this chapter are intended to be published in the future. For a list of contributing authors, see **Puth A**, Kusýn L, Pipa A V, Burlacov I, Dalke A, Hamann S, van Helden J H, Biermann H, and Röpcke J 2020 *Plasma Sources Sci. Technol.* **29** 035001 .

combination with a pressure of 1.5 mbar and a stepwise increased AS plasma power until the treatment temperature of $T_{\text{treat}} = 813$ K was reached. Next the argon flow was stopped, with either the oxygen-containing gas mixture ($\Phi_{\text{H}_2} = 8$ slh, $\Phi_{\text{N}_2} = 67.2$ slh, and $\Phi_{\text{O}_2} = 4.8$ slh) or the oxygen-free gas mixture ($\Phi_{\text{H}_2} = 8$ slh and $\Phi_{\text{N}_2} = 72$ slh) being selected. After some minutes, a bias was applied to the workload, with the bias power stabilized at 0.9 kW, resulting in a plasma power at the AS of 6.3 kW. The treatment concluded after 8 h, at which point the power and gas supply were switched of, resulting in vacuum conditions during cooling. Finally, the two treated samples of pure iron and 42CrMo4 steel were extracted and metallographically analysed. At a later point in time, the comparative treatment experiments were repeated with no LAS monitoring, to treat 31CrMoV9 and X38CrMoV5-1 steel samples.

Table 4.4 Species, spectral positions, and line strengths, at room temperature, used for infrared LAS measurements and their estimated limits of detection. The laser source for the given spectral position is denoted with a Q for an EC-QCL and a T for TDL sources. Data taken from the HITRAN database [11].

Species	Spectral position [cm ⁻¹]	Absorption line strength [cm ⁻¹ /(molecule cm ⁻²)]	Limit of detection [molecules cm ⁻³]	Ref.
CH ₄ ^(Q)	1356.4868	1.784·10 ⁻²⁰	2·10 ¹³	[12]
CH ₄ ^(Q)	1356.5974	1.190·10 ⁻²⁰	2·10 ¹³	[12]
NH ₃ ^(Q)	1388.0552	2.726·10 ⁻²²	2·10 ¹⁴	[13]
NH ₃ ^(Q)	1767.5181	6.090·10 ⁻²¹	2·10 ¹³	[13]
H ₂ O ^(Q)	1387.9337	8.769·10 ⁻²³	5·10 ¹⁴	[11]
H ₂ O ^(Q)	1388.3483	9.843·10 ⁻²⁴	2·10 ¹⁵	[14]
H ₂ O ^(Q)	1781.9619	1.167·10 ⁻²¹	1·10 ¹⁴	[14]
C ₂ H ₂ ^(Q)	1356.8305	5.899·10 ⁻²²	5·10 ¹⁴	[15]
C ₂ H ₂ ^(Q)	1356.8881	8.920·10 ⁻²¹	2·10 ¹³	[15]
HCN ^(Q)	1356.9389	4.636·10 ⁻²³	4·10 ¹⁴	[16]
HCN ^(Q)	1388.3225	3.592·10 ⁻²²	1·10 ¹⁴	[17]
CO ^(T)	2150.3409	1.840·10 ⁻²¹	2·10 ¹¹	[18]
CO ^(T)	2150.8560	1.826·10 ⁻¹⁹	2·10 ¹³	[18]
CO ₂ ^(T)	606.2771	2.713·10 ⁻²¹	5·10 ¹³	[19]

4.3.3 Results and discussion

In accordance with the results from chapter 4.1, the temperature as determined by spectroscopic means was found to be in good agreement with the set temperature $T_{\text{set}} = 773$ K and thus used for determination of absolute concentrations. The resulting column-averaged concentrations of the species CH₄, C₂H₂, HCN, NH₃, CO, CO₂, and H₂O measured as functions of the oxygen-containing fraction of the total gas flow for a) O₂ and b) CO₂ are shown in figure 4.18. The admixed level of O₂ and CO₂ are indicated with dashed grey lines in their respective subfigures.

The trends of all species are comparable between the admixture of O₂ and CO₂, with most of them either monotonously increasing or decreasing in concentration. Except for H₂O and CO₂, in subfigure b) the concentrations of all species are identical for the initial condition of no admixed oxygen-containing precursor. This deviation of both species can assumed to be due to a statistical outlier, as the concentration values are at the limit of detection for both molecules. For the initially predominant molecule HCN, the addition of oxygen to the plasma-chemical environment in both forms leads to a linear decrease of about 30% in concentration of HCN. An identical trend at lower absolute values of concentrations can be found in C₂H₂. This results in their ratio of concentrations $[HCN]/[C_2H_2]$ being

approximately 5.6, independent on the admixture and the level of admixture. Concerning CH_4 , trends are hard to establish, due to its concentration remaining at its limit of detection for both O_2 and CO_2 admixture. The oxygen-containing species CO , CO_2 , and H_2O increase linearly with the fraction of oxygen-bearing precursor. In case of H_2O , the concentrations between both admixtures are agreeing well. However, for CO as well as for CO_2 , the slope of the increasing trend is higher by approximately a factor of two with admixture of CO_2 . Finally, due to the strong linear increase of the oxide species, CO is the predominant measured species at admixture fractions higher than 4 % to the total feed gas fraction. This results in a maximum mole fraction of CO of 20 % at 10 % admixture of CO_2 .

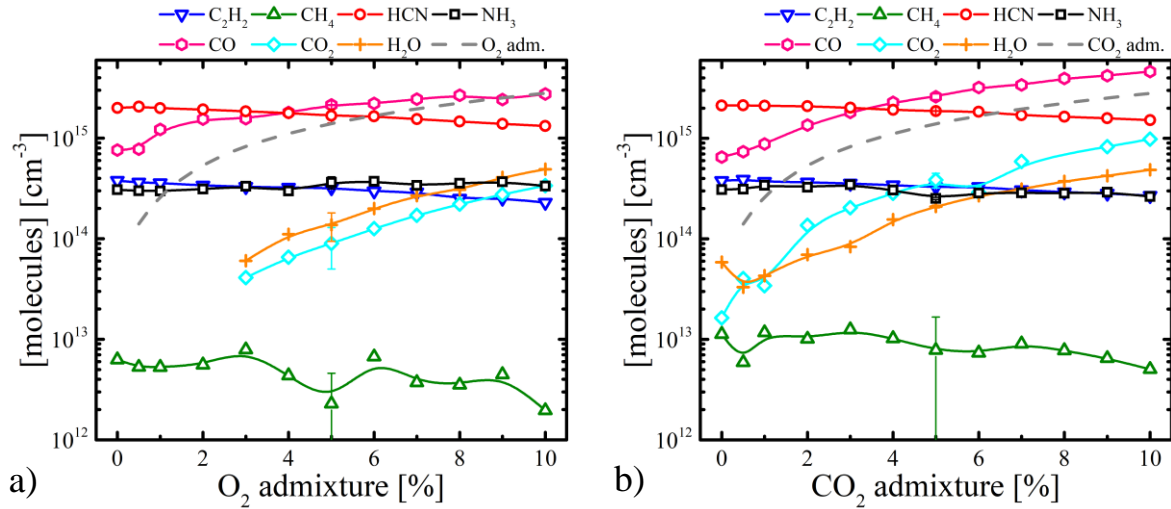


Figure 4.18 Concentrations of C_2H_2 , CH_4 , HCN , NH_3 , CO , CO_2 , and H_2O measured as functions of the a) O_2 and b) CO_2 fraction in the total feed gas mixture. The concentration of admixed oxygen-containing gas is indicated in dashed grey lines. Conditions: $T_{\text{set}} = 773 \text{ K}$, $p = 3 \text{ mbar}$, $P_{\text{AS}} = 7.1 \text{ kW}$, $\Phi_{\text{H}_2} = 8 \text{ slh}$, $\Phi_{\text{N}_2} = (72 - 67.2) \text{ slh}$; a) $\Phi_{\text{O}_2} = (0 - 4.8) \text{ slh}$ and b) $\Phi_{\text{CO}_2} = (0 - 4.8) \text{ slh}$.

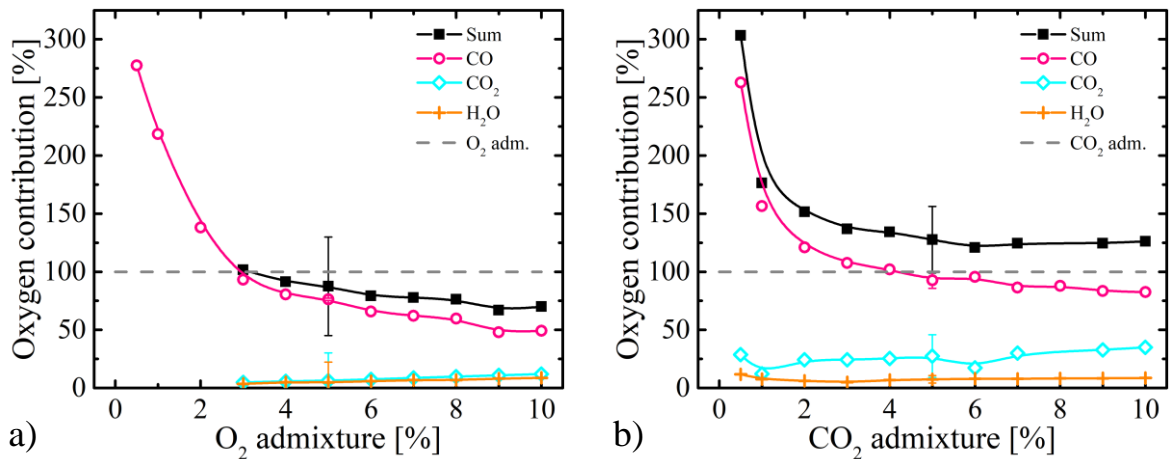


Figure 4.19 Contributions of atomic oxygen of CO , CO_2 , H_2O , and their sum normalized to the oxygen introduced via admixture of a) O_2 and b) CO_2 , indicated as 100 %. Conditions: See figure 4.18.

As can be derived from figure 4.18 b) and 4.19 b), the degree of dissociation of CO_2 is at about 74 %. By accounting for the number of oxygen atoms, figure 4.19 was prepared to show the relative contributions of CO , CO_2 , and H_2O , normalized to the 100 % of introduced oxygen atoms. In both cases, the oxygen-contribution of CO alone exceeds the admixed oxygen content for levels of admixture up to 3 % of total gas flow. This is due to leakage and contamination of the reactor. Again, for both cases, the fraction of oxygen stored in CO molecules monotonously drops, while the fraction stored in CO_2 and H_2O molecules remain constant, in consideration of the indicated margins of error. In particular on figure 4.19 b) at high levels of CO_2 admixture, the sum contribution of all oxide species account for more oxygen than introduced to the process, if the margin of error is ignored. Since the influence of leakage should be negligible at this high levels of admixture, a valid if unlikely explanation can be a faulty

calibration of the CO₂ mass flow controller, admixing approximately 25 % more CO₂ than intended. Similarly for the admixture of O₂ as shown in figure 4.19 a), the sum contribution of all oxide species account for noticeably less, if still well within the margin of error, than the introduced oxygen. This can be explained in multiple ways, e.g. undetected oxide species such as nitrogen oxides, non-dissociated oxygen in the feed gas, or a faulty calibration of the O₂ mass flow controller. As the sum contribution of detected oxide species drop below 75 % of introduced oxygen, the most likely explanation is the decreasing degree of dissociation of O₂ at higher levels of admixture thereof.

The carbon mass flow Φ_C and the carbon consumption efficiency E_{CC} , as previously established in e.g. references [19, 20], are of particular interest due to the difference in carbon content introduced between the two admixed species O₂ and CO₂. Furthermore, the carbon mass flow serves as a measure of weight loss of the AS made of CFC and thus service time of the reactor part. Figure 4.20 presents the carbon mass balance and the carbon consumption efficiency as functions of admixture of a) O₂ and b) CO₂ in % of the total gas flow, considering the concentrations of carbon-containing species detected within the reactor. Both increase linearly with the admixed fraction of oxygen-containing feed gas from approximately 5 to 7 g h⁻¹. The slope of increase is in good agreement between both admixed species, as indicated by the linear fits presented in figure 4.20, with an offset between both fits being smaller than the individual margins of error. An overall lower carbon mass flow compared with the value of (11 ± 1) g h⁻¹ measured for the feed gas ratio of H₂:N₂ = 1:1 at a total flow rate $\Phi_{total} = 80$ slh in reference [20], validates results obtained in a laboratory-scale reactor for the dependency of the carbon mass flow on the feed gas composition published in [19].

Figure 4.20 additionally shows the carbon mass flow Φ_C ([CH₄], [C₂H₂], [HCN]) due to the production of the oxygen-free species CH₄, C₂H₂, and HCN. This contribution to the total carbon mass flow is linearly decreasing from 4 to about 3 g h⁻¹ with increasing admixture of O₂ or CO₂. Furthermore, an offset is noticeable between both curves, albeit again below the margin of error of the respective measurements. The higher oxidative impact of the admixture of O₂ can be seen by the resulting higher overall carbon mass flow while simultaneous lower carbon mass flow of CH₄, C₂H₂, and HCN when O₂ is admixed.

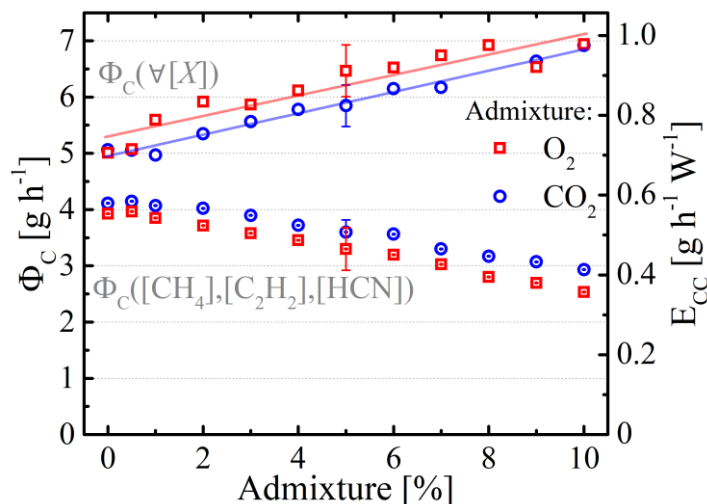


Figure 4.20 Carbon mass flow Φ_C (left axis) and corresponding carbon consumption efficiency E_{CC} (right axis) for all species (upper curves) and for oxygen-free species (lower curves) measured as functions of the admixture of oxygen-containing species O₂ (red) and CO₂ (blue) in % of the total gas flow. Corresponding linear fits are coloured like the respective species. Conditions: See figure 4.18.

Finally, figure 4.21 shows the contributions of atomic hydrogen fixed in the produced and detected molecular species CH₄, C₂H₂, NH₃, H₂O, and HCN, as well as all accounted for hydrogen normalized to the total number of hydrogen atoms introduced via the feed gas, measured as functions of the fraction of the oxygen-containing admixture. Overall, for both admixture species O₂ and CO₂, the produced

species account for 70 % of the available hydrogen. Since NH_3 maintains a stable concentration independent on admixture conditions, the amount of hydrogen bound in H_2O increases by the amount of hydrogen released in the reducing concentrations of CH_4 , C_2H_2 , and HCN with increasing fraction of admixture. The unaccounted for fraction of hydrogen of 30 % can be attributed to undetected species such as atomic and molecular hydrogen, and others.

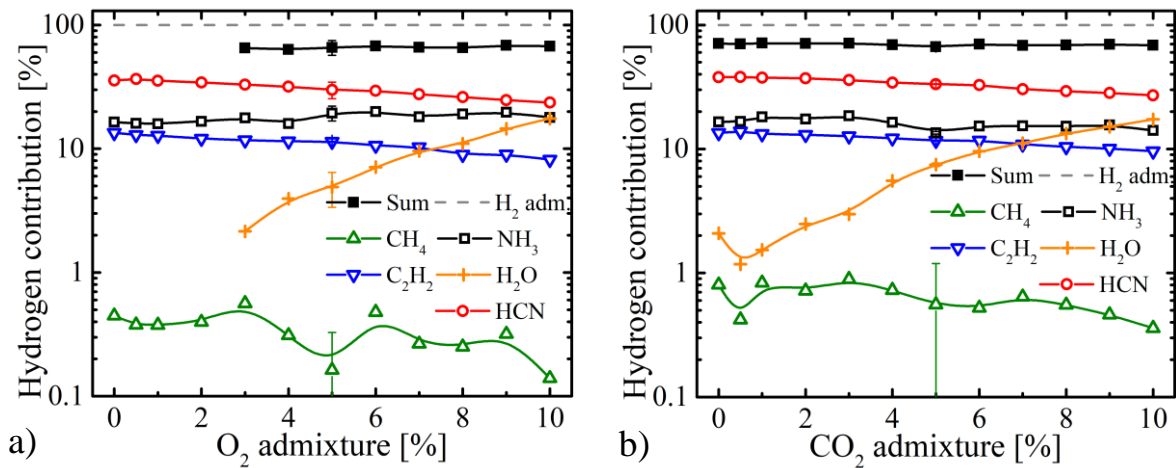


Figure 4.21 Contributions of atomic hydrogen of CH_4 , C_2H_2 , NH_3 , H_2O , HCN and their sum normalized to the hydrogen introduced in the feed gas, measured as functions of the a) O_2 or b) CO_2 admixture in % of the total feed gas flow. The fed-in hydrogen is indicated in a grey dashed line. Conditions: See figure 4.18.

With regards to the stability of the process, time-dependent measurements of the concentrations of CH_4 , C_2H_2 , HCN , NH_3 , CO , CO_2 , and H_2O are shown in figure 4.22 for a) no admixture and b) 6 % admixture of O_2 . Albeit the process temperature has increased by 50 K, the measured concentrations match the values shown in figure 4.18 a) with only minor increases in the concentrations of NH_3 , CO , CO_2 , and H_2O at elevated temperature. With progressing treatment time and in both admixture conditions, the concentrations of most species remain constant. In subfigure a), all species deviate from this at the last measurement point, with NH_3 increasing, while HCN , C_2H_2 , CO , and CH_4 decrease. This behaviour is due to a brief instability of the power supply. An instantaneous doubling in the concentration of CO_2 in subfigure b) is related to a failure of the cryogenic cooling, affecting the laser diode used for CO_2 detection and resulting in a worse signal-to-noise ratio, thus much increased error of measurement. Beside those externally caused deviations, only the decrease from $5 \cdot 10^{14}$ to $9 \cdot 10^{13} \text{ cm}^{-3}$ of the concentration of CO with no admixture of O_2 can be identified as a temporal trend. Figure 4.23 shows the fit of an exponential decay with offset to the concentration curve of CO , excluding the last measurement point.

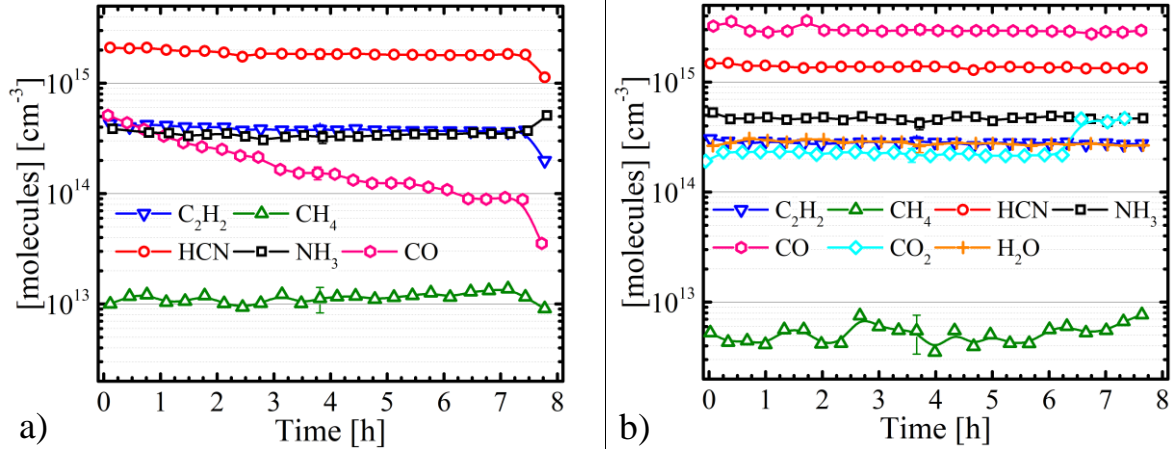


Figure 4.22 Concentrations of CH_4 , C_2H_2 , HCN , NH_3 , CO , CO_2 , and H_2O measured as functions of time during sample treatment. Conditions: $T_{\text{set}} = 813 \text{ K}$, $p = 3 \text{ mbar}$, $P_{\text{AS}} = 6.3 \text{ kW}$, $P_{\text{Bias}} = 0.9 \text{ kW}$, $\Phi_{\text{H}_2} = 8 \text{ slh}$; a) $\Phi_{\text{N}_2} = 72 \text{ slh}$, b) $\Phi_{\text{N}_2} = 67.2 \text{ slh}$ and $\Phi_{\text{O}_2} = 4.8 \text{ slh}$.

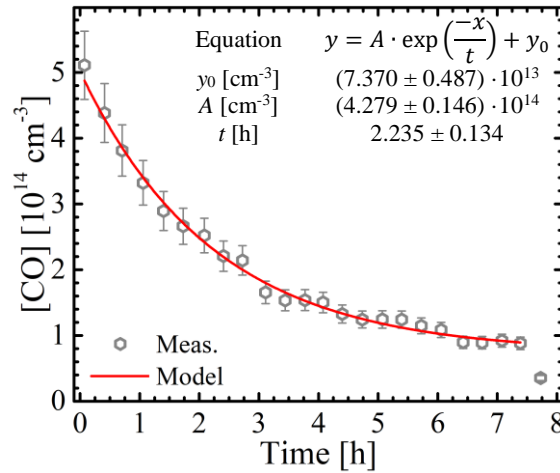


Figure 4.23 Concentration of CO as a function of time during sample treatment fitted with an offset exponential decay. The results of the fit are given in the inset table. Conditions: See figure 4.22.

From the fit shown in figure 4.23, the base concentration of CO of $7.4 \cdot 10^{13} \text{ cm}^{-3}$ and the decay constant of 2.23 h, equivalent to a half-life of 1.54 h. As no oxygen is introduced to the plasma process, two sources are to be considered to supply oxygen to form CO : desorption of oxygen-containing species, such as O_2 and H_2O , from surfaces inside the reactor vessel and leakage of atmospheric O_2 into the vessel. In a previous publication, the function of walls as sources of oxygen was observed to be dependent on an active discharge, with no release under vacuum conditions; however the process could not be fitted with a model [20]. As figure 4.23 shows, the decay constant is on the same time scale as the treatment process, indicating the high surface area of the AS made of CFC. On the other hand, the process is to be neglected if some percent of oxygen-containing species are admixed, as figure 4.19 shows. Next, the base concentration of CO can be correlated to a constant O_2 leakage of 0.12 slh or 2 sccm. Considering a typical atmospheric composition, a total leak of 0.57 slh in flow rate can be assumed. The O_2 leakage is considerably smaller than the CO production rate reported in [20], ranging from 0.6 to 0.4 slh. This is due to the previous study not differentiating between the two sources of oxygen, as well as the factor of 2 between O_2 and CO in atomic oxygen content.

4.3.4 Summary and conclusions

Two sets of systematic measurements of the concentrations of CH₄, C₂H₂, HCN, NH₃, CO, CO₂, and H₂O as functions of the time and the feed gas admixture of O₂ or CO₂ were conducted in an industrial-scale active screen nitrocarburizing reactor equipped with an active screen made of carbon-fibre reinforced carbon. This was achieved using two different laser sources, external-cavity quantum cascade lasers and lead-salt tuneable diode lasers, operated in the infrared spectral region to monitor the temperatures of the molecular species and the absorbance of select associated transitions. In agreement with previously published studies [20, 21], the determined temperatures matched the temperature measured with a thermocouple at a model probe within the reactor volume.

The admixture of O₂ or CO₂ to the feed gas resulted in decreases in the concentrations of C₂H₂ and HCN and increases in the concentrations of CO, CO₂, and H₂O, in all cases linear with the admixed fraction relative to the total feed gas flow. For the concentrations of CH₄ and NH₃, no such dependency was noted. Comparing between both admixed species, with increasing admixture of CO₂ the concentrations of CO and CO₂ were strongly increased. Furthermore, the initial values of concentration at 0 % admixture validated the values reported in [20].

By accounting for the number of introduced atoms, mass balances were established. This way, for high levels of admixture a decreasing fraction of the supplied oxygen was bound in CO, with the contributions of CO₂ and H₂O increasing. However, most accounted for oxygen was found in the form of CO.

Next concerning the practical matter of the carbon mass flow Φ_C , a linear increase in the mass flow with increasing levels of admixture was observed. As the concentrations of HCN and C₂H₂ decrease, the net gain in carbon mass flow can be ascribed to the increase in concentrations of CO and CO₂. Only minor differences between both admixed species were discerned, with O₂ admixture resulting in slightly decreased carbon mass flow by production of C₂H₂ and HCN, while simultaneously the overall carbon mass flow was increased.

Finally, by accounting for the hydrogen introduced by the H₂ fraction of 10 % of the total feed gas flow, a degree of dissociation for hydrogen was found to be constant at 70 %, by measurement of the concentrations of the reaction products as functions of the admixed oxygen-containing fraction. Consequently, the increase in concentration of H₂O is balanced for the number of hydrogen atoms with the decrease in concentrations of C₂H₂ and HCN.

From a plasma-chemical viewpoint, the drawback of an increased carbon mass flow with increasing levels of oxygen-containing admixtures outweighs the benefits of lowered concentrations of C₂H₂ and HCN and thus lowered carburizing potential. In particular, for plasma nitrocarburizing of stainless steels, the production of H₂O may adversely affect the reaction balance of the reduction of CrO₂ with HCN, as in this reaction H₂O is formed [22]. However, the thermochemical diffusion process at the workload surface needs to be considered too, which requires post-treatment surface diagnostics. In preliminary results not shown in this study, the admixture of oxygen-containing species prevented the formation of unwanted iron carbides and beneficially affected the nitrocarburizing results in some steels. On this topic, a manuscript is pending.

In a second set of measurements, time-dependencies of the concentrations were studied with admixture of 6 % O₂ of the total flow and no admixture. The measured concentrations matched well with the values recorded in the previous set of measurements and remained stable for the treatment duration of 8 h, aside from the concentration of CO with no admixture. There an exponential decay was observed, from which the oxygen leak rate of 2 sccm was derived. Furthermore, the decay was found to occur on the same time scale than the process time, which can be explained by the high surface area of the active screen made of carbon-fibre reinforced carbon. In a previous study, the decay was shown to only progress with plasma activity [20], accordingly the adsorbed oxygen can be assumed to require an activation energy to be released. Finally, oxygen-containing gas pockets within the solid carbon active screen can be

excluded as major sources of oxygen, as the carbon mass flow, thus the abrasion rate, remains constant and in consequence, oxygen released this way would present itself as an additional leakage.

The now proven stability of the plasma-chemical conditions for the treatment duration is an important validation for previous measurements and their application to metallographical investigations. Furthermore, it is an important step towards process control of industrial-scale nitrocarburizing plasmas.

References

- [1] Ebersbach U *et al.* 1991 *HTM J. Heat Treat. Mat.* **46** 339
- [2] Karakan M, Alsaran A, and Çelik A 2004 *Mater. Des.* **25** 349-353
- [3] Mandkarian N and Mahboudi F 2009 *Vacuum* **83**:7 1036-1042
- [4] Jeon E-K, Park I M, and Lee I 2007 *Mater. Sci. Eng. A* **449** 868-871
- [5] Díaz-Guillén J C *et al.* 2020 *Surf. Coat. Technol.* **385** 125420
- [6] Bogaerts A *et al.* 2017 *Plasma Process. Polym.* **14** e1600070
- [7] Pintassilgo C D *et al.* 2007 *J. Phys. D: Appl. Phys.* **40** 3620-3632
- [8] De Bie C *et al.* 2011 *Plasma Sources Sci. Technol.* **20** 024008
- [9] Eliasson B *et al.* 1998 *Ind. Eng. Chem. Res.* **37** 3350
- [10] Goujard V *et al.* 2011 *J. Phys. D: Appl. Phys.* **44** 274011
- [11] Gordon I *et al.* 2017 *J. Quant. Spectrosc. Radiat. Transfer* **96** 139
- [12] Ba Y *et al.* 2013 *J. Quant. Spectrosc. Radiat. Transfer* **130** 62
- [13] Cottaz C *et al.* 2000 *J. Mol. Spectrosc.* **203** 285
- [14] Toth R A, database provided by mark4sun.jpl.nasa.gov/h2o.html
- [15] Gomez L *et al.* 2010 *J. Quant. Spectrosc. Radiat. Transfer* **111** 2256
- [16] Maki A G *et al.* 2000 *J. Mol. Spectrosc.* **202** 67
- [17] Maki A G, Quapp W, and Klee S 2000 *J. Mol. Spectrosc.* **171** 420
- [18] Coxon J A and Hajigeorgiou P 2004 *J. Chem. Phys.* **121** 2992
- [19] Puth A *et al.* 2018 *Plasma Sources Sci. Technol.* **27** 075017
- [20] Puth A *et al.* 2020 *Plasma Sources Sci. Technol.* **29** 035001
- [21] Hamann S *et al.* 2015 *J. Phys. D: Appl. Phys.* **48** 34
- [22] Lebrun J P 2000 *US Patent Specification* 7,074,460 B2 18.04

5 Investigation at a laboratory-scale ASPN reactor using an AS made of CFC⁴

5.1 Introduction

Conventional plasma nitrocarburizing (CPNC) is a widely used technology for the thermochemical treatment of plain carbon and low alloy steels with the focus on the improvement of the performance of components for a higher fatigue strength as well as for increased wear and corrosion resistance. Assisted by pulsed dc discharges, plasma nitriding and plasma nitrocarburizing have been employed as surface engineering methods to enhance tribological properties of metal surfaces for several decades. In a variety of applications, the conventional plasma nitriding technique (CPN) has become an industrial standard approach for surface hardening and surface modification [1 – 5]. These methods are based on thermochemical diffusion processes. In the CPN case, the metallic components to be treated act as a cathode for the used discharges, in general, driven in N₂-H₂ feed gas mixtures. In case of plasma nitrocarburizing small admixtures of carbon-containing precursor gases, e.g. CO₂ and/or CH₄, are added to the feed [6]. The physico-chemical mechanism of CPN is governed by the interaction of excited atomic and molecular species with the metallic surfaces of the components heated to an appropriate temperature. However, limitations of the CPN technology concerning the variation of the carburizing potential of the process atmosphere have to be pointed out. For the CPN technology, the control of the mass flow of the carbon-containing gases is typically based on empirical-derived recipes combined with the operator's experience, with little regard to the concurrent process conditions. Therefore, even for a low percentage of addition of carbon-containing gases the risk of soot production and cementite precipitation in the compound layer is high [1].

Already about two decades ago, the basic principle of a modified plasma assisted nitriding technique, the active screen plasma nitriding (ASPN), has been developed to overcome the limitations of CPN by relocating the glow discharge region from the metallic components to an additionally introduced separate active screen (AS) made of construction steel. This screen surrounds the workload, thus avoiding detrimental hollow cathode and arcing effects. The AS plasma ensures (i) a radiation controlled excellent temperature homogeneity of the metallic workload, and (ii) the generation of highly reactive gas species from the precursor gases. For large industrial-scale ASPN systems, a weak bias voltage applied to the components' surfaces, is essential to achieve a reasonable nitriding response [7, 8]. In case a visible secondary plasma forms around the workload, this is referred to as the bias plasma. In recent years, the ASPN technology has demonstrated its growing commercial potential as well as an increasing scientific interest [7 – 11].

Recently the importance of added co-alloys to the screen material, normally made of steel, for the treatment result, e.g. aluminium or silver, has become the centre of interest [12, 13]. In addition, it was found, that the nitriding efficiency could be increased by small amounts of hydrocarbons in the N₂-H₂ plasma [14]. Already in 2000, a solid graphite target, directly located in the plasma volume, has been proposed as alternative to gaseous carbon-containing precursors with sputtering processes as a source for reactive species [15]. In particular, present in the gas phase non-saturated H-C-N compounds can cause a remarkable intensification of nitrocarburizing processes while simultaneously destroying the impeding passive layer on stainless steel surfaces [16].

For several years, in particular, in fusion research and in plasma-based deposition processes of hard carbon and carbon-nitrogen layers the interaction phenomena between the plasma and carbon-containing surfaces have been in the centre of interest [17 – 23]. In 2011, Crespi *et al.* proposed the use of an AS

⁴ Published as: **Puth A**, Hamann S, Kusýn L, Burlacov I, Dalke A, Spies H-J, Biermann H, and Röpcke J 2018 *Plasma Sources Sci. Technol.* **27** 075017

made of graphite for the deposition of CN layers on polymer substrates. As a main process, physical sputtering was found to provide carbon-containing species to the plasma for the synthesis of CN [24].

The use of carbon-containing feed gases, e.g. CH₄ and CO₂, has led to a growing complexity of the ASPN processes, in turn requiring appropriate diagnostic techniques. Non-intrusive *in-situ* plasma diagnostics methods provide information about the fundamental mechanisms of advanced plasma nitrocarburizing. In particular, the quantitative monitoring of absolute concentrations of relevant molecular species and their respective temperatures can support a better understanding of these technological plasmas.

Laser absorption spectroscopy in the mid-infrared spectral range (IRLAS) combined with Fourier transform infrared (FTIR) spectroscopy, complemented by optical emission spectroscopy (OES) and Langmuir probe diagnostics have been proven to be versatile techniques for gaining insight into physical and chemical plasma phenomena. Although frequently used for studies of molecular discharges in a wide spectral range, FTIR spectroscopy is generally insufficiently sensitive for monitoring transient species in plasmas. In contrast nowadays, IRLAS using different radiation sources, such as lead-salt tuneable diode (TDLs), quantum cascade (QCLs), and inter-band cascade lasers (ICLs), is well suited for the measurement of absolute concentrations of a wide variety of molecular species in ground and excited states.

Already in 2012, tuneable diode laser absorption spectroscopy (TDLAS) has been used to monitor the concentration of NH₃ depending on the H₂-N₂ ratio of the feed gas mixture in an industrial-scale reactor [25]. In a subsequent spectroscopic study based on TDLAS and FTIR spectroscopy, the conventional and the AS nitriding approaches have been investigated and compared using CH₄ or CO₂ as gaseous carbon precursors [26]. Varying the discharge conditions, the evolution of the concentrations of the methyl radical and of eight stable molecular species were monitored and the degree of dissociation of the carbon-containing precursors was determined. OES provided the rotational temperature of molecular nitrogen [26]. Time-resolved Langmuir probe measurements combined with OES allowed insight into general processes of the ASPN approach [27]. Recently, the interplay between the plasma at the biased metallic components and the screen plasma was investigated in the same ASPN reactor, leading to a better understanding of nitrocarburizing phenomena [28].

In 2011 quantum cascade laser absorption spectroscopy (QCLAS) was first used for a time-resolved study of industrial CPN processes involving admixture of BCl₃ [29, 30]. The investigation benefited from the wide spectral range accessible with external-cavity quantum cascade lasers (EC-QCL), thus allowing for multi-component detection. In turn, EC-QCLs became the state-of-the-art source for a number of applications including ASPN plasmas [31, 32].

Recently, in an industrial-scale reactor, a combined approach based on IRLAS and bias power management has been proposed for process control of the active screen plasma nitrocarburizing (ASPNC) technology [33]. While the bias power applied to the components was found to enable a dynamic control in uptake of nitrogen and carbon on the treated surfaces, the concentration of HCN measured directly in the plasma volume is a parameter of the carburizing potential of the discharge [33]. In the same reactor system, the use of an AS made of carbon-fibre reinforced carbon (CFC) compared to a conventionally used steel screen led to a significant improvement of treatment results for different treated types of alloyed steel [34].

Advanced diagnostics approaches, such as OES and IRLAS, have been suffering from limitations of the construction principles of the used plasma reactors. An optical path is required for the implementation of *in-situ* IRLAS. Therefore, cylindrical ASPN reactors have to provide a line-of-sight through the reactor walls and the AS. Furthermore, as a matter of principle of measurement, concentrations of molecules can only be determined by IRLAS as column-integrated values. Local deviations from the average along the line-of-sight cannot be discerned.

In 2015, to overcome these specific diagnostic limitations inherent to the construction of industrial-scale ASPN reactors, a novel type of laboratory-scale reactor has been designed [31]. For detailed studying of complex processes, the plasma nitriding monitoring reactor, PLANIMOR, is characterized by a linear internal electrode configuration combined with separate diagnostic observation possibilities. This model reactor is characterized by different distinct plasma regions and specific transitions between them, as (i) at the AS, (ii) at the sample holder, and (iii) in the intermediate space. These three regions can be observed and studied separately and spatially resolved. The general plasma-chemical similarities of PLANIMOR and the industrial-scale ASPN reactor have previously been reported [32]. Recently, in H_2-N_2 plasmas at PLANIMOR, spectroscopic investigations have been performed to compare two different screen electrodes: (i) a carbon screen without the usage of any additional gaseous carbon-containing precursors, and (ii) a screen made of steel combined with small CH_4 admixtures [35]. Based on QCLAS the evolution of the concentrations of four stable molecular species, NH_3 , HCN , CH_4 , and C_2H_2 , were monitored. Significant differences were found in the concentrations of HCN and C_2H_2 , which are 30 and 70 times higher with use of the CFC screen compared to the steel screen, respectively. Additionally, the emission characteristics of the AS plasmas, studied by OES, showed remarkable differences in the intensity of the CN (0-0) band [35].

In the present study, a more detailed spectroscopic investigation of plasma-chemical aspects in nitrocarburizing processes using an AS made of CFC has been performed in PLANIMOR. Combining TDLAS and EC-QCLAS the evolution of the concentrations of the methyl radical and of eight stable species, CH_4 , HCN , NH_3 , CO , C_2H_2 , C_2H_4 , C_2H_6 , and C_2N_2 , have been monitored. One objective was to study the dependencies of concentrations (i) on power and (ii) on the H_2-N_2 ratio in the feed gas mixture. In addition, values of the temperature of different molecular species have been determined. Based on the measured concentrations the carbon consumption rate of the used AS was calculated, both as a function of power and of feed gas mixture.

5.2 Experimental

The schematic top-view of the experimental arrangement at PLANIMOR combined with QCLAS and TDLAS spectrometers is shown in figure 5.1. The reactor is only briefly described here with further details in references [31] and [35]. PLANIMOR predominantly consists of a borosilicate glass tube with a length of 40 cm and an inner diameter of 10 cm. The centre section of 16 cm in length is expanded to an inner diameter of 13 cm with two perpendicular flanges providing a diagnostic path for an optical White cell with 38 cm in length [36]. The plane of the White cell is parallel to the screen and the sample holder. These are in turn located on two opposing hollow stainless steel cylinders, which are moveable coaxially to the glass vessel. The feed gas is introduced via the cylinder further containing the grounded anode and the meshed electrode, i.e. the AS made of CFC. At the opposite cylinder, see figure 5.1, right part, the heated sample holder is mounted and the pumping system is connected.

As power supply for the AS plasma a generator at a frequency of $f = 1$ kHz at a 60 % duty cycle has been used. The average values of the voltage and current were in the ranges of $U_{\text{screen}} = 190 - 250$ V and $I_{\text{screen}} = 170 - 430$ mA, respectively. Therefore, the power of the screen plasma could be varied in the range of $P_{\text{screen}} = 30 - 150$ W.

The H_2-N_2 feed gas mixture and the total gas flow were controlled by two independent mass flow controllers. Finally the pumping system, consisting of a butterfly valve and a turbomolecular pump, was maintaining the gas pressure at a set value in the range of $p = 1 - 5$ mbar.

For the IRLAS measurements in PLANIMOR, a combined TDLAS and EC-QCLAS spectrometer consisting of the IRMA system [37] and an EC-QCL (Daylight solutions) setup has been used [35, 38]. The IRLAS spectrometer covers the fingerprint region for the species given in table 5.1. For simultaneously recording of spectra, the spectrometer consists of a three channel configuration,

including measurement, reference gas, and etalon channels. Based on an optical multipath cell of White cell type leading to an optical length of $L = 1.9$ m inside the reactor an increased sensitivity for species of down to 10^{12} molecules cm^{-3} could be ensured, see table 5.1. The infrared beam of the measurement channel directed via KBr windows into the multipath cell is finally focused on a liquid-nitrogen cooled HgCdTe infrared detector, see figure 5.1.

Table 5.1 compiles the used spectral positions, line strengths, and estimated limits of detections of the molecular species sampled by the IRLAS measurements of the present study. The spectral positions and the identification of the absorption lines of the monitored molecular plasma components have been performed using well-documented reference gas spectra and an etalon of known free spectral range [39].

In figure 5.2 QCLAS and TDLAS absorption spectra of CH_4 , HCN, and C_2H_2 in the spectral range near 1356.7 cm^{-1} and of CO and C_2N_2 in the spectral range near 2150.6 cm^{-1} , respectively, are presented. The conditions were the following, total gas flow $\Phi_{\text{Total}} = 10$ sccm $\text{H}_2 + 10$ sccm N_2 , plasma power $P_{\text{screen}} = 55$ W, and pressure $p = 3$ mbar. The inset of figure 5.2 b) shows an absorption feature of CH_3 at 606.1 cm^{-1} for the same conditions, except the plasma power of $P_{\text{screen}} = 93$ W.

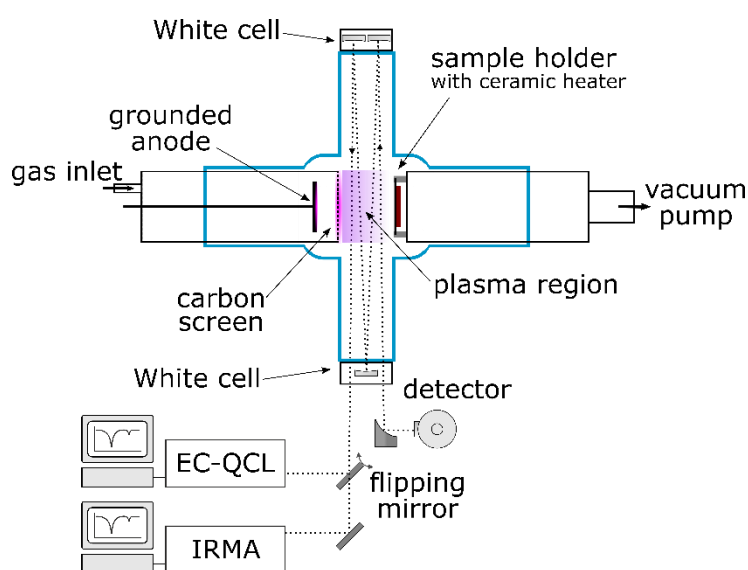


Figure 5.1 Schematic top-view of the experimental arrangement at PLANIMOR combined with QCLAS and TDLAS spectrometers. The plane of the White cell is parallel to the screen and the sample holder. (Here depicted as rotated by 90° for better illustration.)

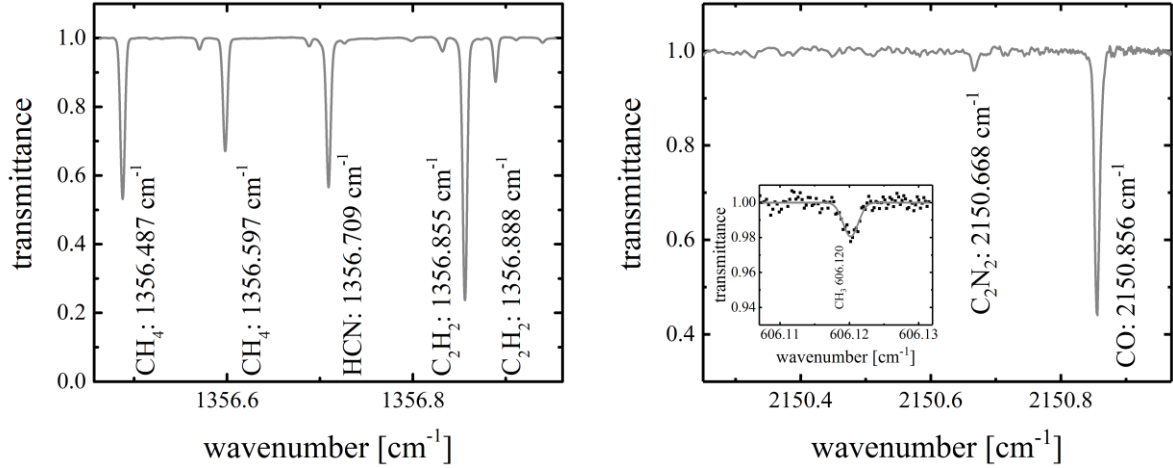


Figure 5.2 a) QCLAS transmittance spectrum of CH_4 , HCN , and C_2H_2 in the spectral range near 1356.7 cm^{-1} and b) TDLAS transmittance spectrum of CO and C_2N_2 in the spectral range near 2150.6 cm^{-1} , both using an AS made of CFC. Conditions: $\Phi_{\text{Total}} = 10 \text{ sccm H}_2 + 10 \text{ sccm N}_2$, $P_{\text{screen}} = 55 \text{ W}$, $p = 3 \text{ mbar}$. The inset shows the $Q(3-3)$ absorption line of CH_3 at 606.1 cm^{-1} at $P_{\text{screen}} = 93 \text{ W}$.

Table 5.1 Species, spectral positions, and line strengths at room temperature, used for the IRLAS measurements and the respective estimated limits of detection using a combined TDLAS^(T) and EC-QCLAS^(Q) spectrometer in PLANIMOR.

Species	Spectral position [cm^{-1}]	Absorption line strength [$\text{cm}^{-1}/(\text{molecule cm}^{-2})$]	Limit of detection [molecules cm^{-3}]	Ref.
$\text{CH}_4^{(Q)}$	1356.5974	$1.190 \cdot 10^{-20}$	$1 \cdot 10^{13}$	[39]
$\text{HCN}^{(Q)}$	1356.9389	$4.636 \cdot 10^{-23}$	$2 \cdot 10^{14}$	[39]
$\text{HCN}^{(Q)}$	1388.3225	$3.592 \cdot 10^{-22}$	$5 \cdot 10^{13}$	[39]
$\text{NH}_3^{(Q)}$	1388.0552	$2.726 \cdot 10^{-22}$	$1 \cdot 10^{14}$	[39]
$\text{CO}^{(T)}$	2150.3409	$1.840 \cdot 10^{-21}$	$1 \cdot 10^{11}$	[39]
$\text{CO}^{(T)}$	2150.8560	$1.826 \cdot 10^{-19}$	$1 \cdot 10^{13}$	[39]
$\text{C}_2\text{H}_6^{(T)}$	2993.4710	$3.850 \cdot 10^{-20}$	$1 \cdot 10^{12}$	[39]
$\text{C}_2\text{H}_4^{(T)}$	2993.8362	$1.496 \cdot 10^{-21}$	$2 \cdot 10^{13}$	[39]
$\text{C}_2\text{H}_2^{(Q)}$	1356.8881	$8.920 \cdot 10^{-21}$	$1 \cdot 10^{13}$	[39]
$\text{CH}_3^{(T)}$	606.1203	$4.547 \cdot 10^{-19}$	$1 \cdot 10^{12}$	[40,41]
$\text{C}_2\text{N}_2^{(T)}$	2150.6668	$1.13 \cdot 10^{-20}$	$5 \cdot 10^{12}$	[42]

For further insight into the plasma chemical conversion, the measured concentrations were used to calculate absolute conversion efficiencies to the monitored reaction products. These values are normalized on the plasma power.

Analogous to references [43] and [44] the conversion efficiency, R_C , is expressed as:

$$R_C = n_{\text{molecules}} \cdot \frac{\Phi_{\text{Total}}}{60} \cdot \frac{10^3}{p} \cdot \frac{1}{P_{\text{Total}}}, \quad (5.1)$$

with $n_{\text{molecules}}$ the concentration of the monitored molecular reaction product in molecules cm^{-3} , Φ_{Total} the total gas flow rate in sccm, p the pressure in mbar, and P_{Total} the plasma power in W.

5.3 Results and discussion

Along the axis of the optical measurements, determined by the position of the White cell in PLANIMOR, the plasma in front of the carbon screen and the surrounding volume are characterized by considerable gradients of the gas temperature T_{gas} . In the plasma bulk, the gas temperature can reach relatively high values, as indicated by short-lived species such as ions and radicals. The glass walls of the reactor, in particular, the side arms of the White cell, although not actively cooled, are maintained close to room temperature.

In previous studies of nitriding plasmas, the gas temperature was derived from the optical emissions of the N_2 and N_2^+ bands [26, 28, 45]. In an industrial-scale ASPN reactor, it was shown that the rotational temperature of the plasma of the metallic screen, determined from the N_2^+ (0-0) band of the first negative system, corresponds to the process temperature measured at the metallic components [26, 28]. Recently, for PLANIMOR a similar dependency of this temperature on the plasma power at the AS has been reported, at slightly lower absolute values than in the industrial-scale reactor [32]. Independent on the screen material of steel or carbon, the temperature was found to increase from 650 to 900 K with the plasma power [35].

Since the rotational temperatures factor into the line strengths and thus the determination of absolute concentrations, spatial thermal inhomogeneity needs to be taken into account. Three different methods have been applied:

- (i) using an EC-QCL the intensity ratio of two HCN absorption lines was studied to determine the rotational temperature of this molecule,
- (ii) by TDLAS the intensity ratio of two CO lines was used for calculating the rotational temperature of CO, and
- (iii) based on TDL measurements the line profile of the Q(3-3) line of CH_3 has been analysed to derive the gas temperature of this radical.

The results have been complemented with the rotational temperature of the N_2^+ (0-0) band from [35].

In figure 5.3 the temperatures of the stable species, HCN and CO, of the methyl radical, and of the N_2^+ ions depending on the plasma power at the AS, P_{screen} , are shown. The discharge was maintained in a gas flow of $\Phi_{\text{Total}} = 20$ sccm, at a feed gas composition of $\text{N}_2:\text{H}_2 = 1:1$, and a pressure of $p = 3$ mbar.

Deviations between the curves corresponding to the four different approaches validate the requirement to consider spatial temperature inhomogeneity. A threefold sectioning of the visible discharge zone located at the AS, a flowing afterglow zone placed in the downstream region of the discharge, and a volume of gas at both ends of the White cell is proposed. Accordingly, OES predominantly samples the visibly emitting discharge zone, with LAS sampling occurring through all three zones.

The rotational temperature of the N_2^+ molecule was found to range between 650 and 900 K followed by the methyl radical with temperatures between 400 and 800 K both increasing with power [35]. The temperature values of the N_2^+ ions indicate that the emission originates from the hot region inside the plasma bulk. Further, CH_3 is predominantly produced in the plasma zone, but due to its lifetime of a few ms, it can diffuse to a certain extent into the colder regions. This behaviour is reflected in the lower averaged temperature of about 200 K compared to N_2^+ . It is of note, that both transient species show a comparable relative dependence, i.e. a strong increase with power.

Both stable molecules, HCN and CO, are characterized by considerably lower temperatures. The temperature of HCN shows only a slight increase with power between 340 and 400 K, while the temperature of CO increases up to 500 K at values of $P_{\text{screen}} = 106$ W. At a high plasma power applied

to the plasma screen, the difference in temperatures of both stable species exceeds the margin of error. The higher temperature of CO can be attributed to the formation by sputtering of carbon by oxygen.

Concerning the determination of absolute densities, thermal equilibration between translational and rotational degrees of freedom is assumed.

While the determined temperatures of CO and CH₃ were further used for the determination of their respective concentrations, the temperature of HCN was interpreted to be representative for the temperatures of all stable species with the exception of CO. As the only detected di-atomic and further only oxygen-containing molecule, CO is assumed to be only produced by sputtering of solid carbon by oxygen. Contrary to this, the production pathways of other stable species can be assumed to be related spatially and chemically, resulting in thermalisation.

The concentrations of C₂H₂, CH₄, HCN, NH₃, CO, C₂H₆, and CH₃ and the related mole fraction of these molecules depending on the plasma power of the screen for a gas flow rate of 10 sccm of N₂ and 10 sccm of H₂ are shown in figures 5.4 a) and b), respectively. It can be seen, that the concentrations of all carbon containing molecules increase, while that of NH₃ shows a maximum for a screen plasma power, P_{screen} , between 40 and 60 W. The reason for the decreasing concentration for plasma powers higher than $P_{\text{screen}} = 60$ W is the thermal dissociation of NH₃ due to the increasing gas temperature in the volume of and around the plasma zone, which can be seen in the temperatures of N₂⁺ and of CH₃ being significantly higher than 673 K.

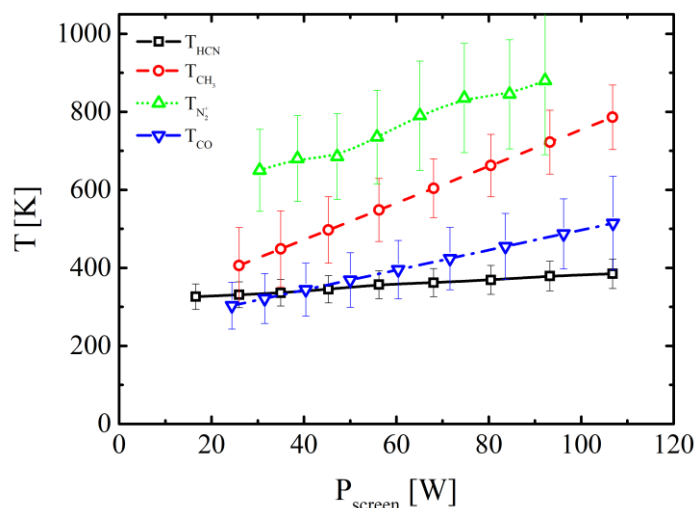


Figure 5.3 Temperatures of stable species, HCN and CO, of the radical CH₃ and of the ion N₂⁺ measured as functions of the plasma power at the AS P_{screen} . $\Phi_{\text{Total}} = 20$ sccm, N₂:H₂ = 1:1, $p = 3$ mbar. T_{HCN} and T_{CO} are derived from the rotational temperatures of HCN and CO, T_{CH_3} from line profile analysis of CH₃, and $T_{\text{N}_2^+}$ from the rotational temperature of the (0-0) band of the FNS of N₂⁺ (from [35]).

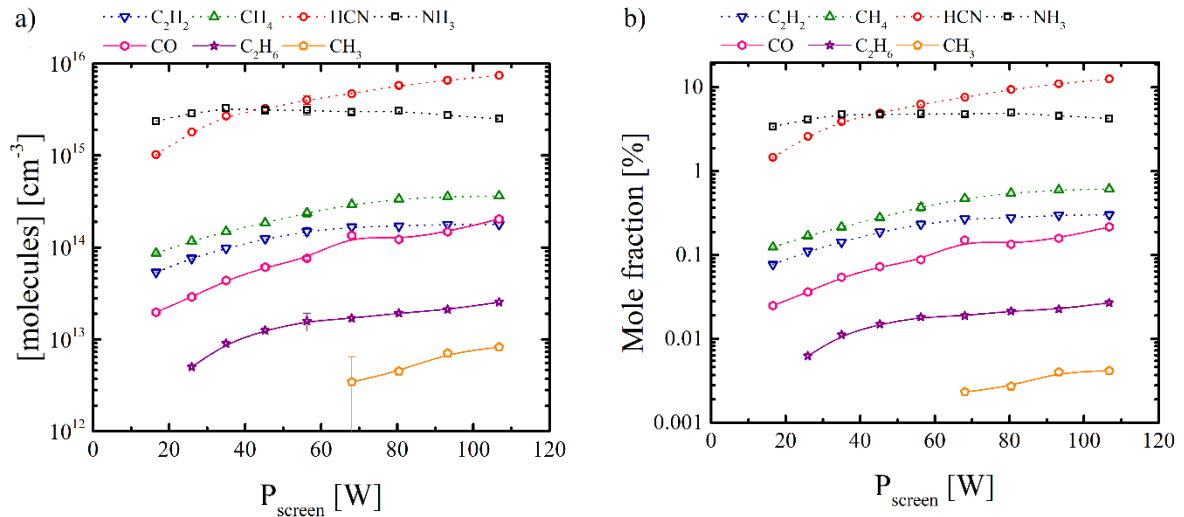


Figure 5.4 a) Concentrations and b) mole fractions of C_2H_2 , CH_4 , HCN , NH_3 , CO , C_2H_6 , and CH_3 as functions of the plasma power at the active screen P_{screen} . $\Phi_{\text{Total}} = 20 \text{ sccm}$, $\text{N}_2:\text{H}_2 = 1:1$, $p = 3 \text{ mbar}$.

The concentrations of the carbon-containing reaction products increases with the power of the screen plasma. While CH_4 , C_2H_2 , C_2H_6 , HCN , and CH_3 are the reaction products of the $\text{N}_2\text{-H}_2$ feeding gas with the solid carbon of the screen, CO is formed due to both the contamination of the reactor walls and of the carbon screen with oxygen and the leakage of the reactor leading to a noticeable amount of O_2 in the gas phase. In the plasma at the screen, molecular oxygen is dissociated and thus able to form CO by chemical sputtering. Furthermore, for the formation of the hydrocarbons and HCN , chemical sputtering of the solid carbon is assumed as the main process [35].

As shown in figures 5.4 a) and b), HCN and NH_3 are the most abundant reaction products, followed by CH_4 , C_2H_2 , and CO . The mole fraction of HCN reaches up to 13 % of the whole gas mixture, that of NH_3 is up to 5 %, and the amounts of CH_4 , C_2H_2 , and CO are up to 0.7, 0.3, and 0.2 %, respectively (see figure 5.4 b)). That of C_2H_6 is up to 0.04 % and the mole fraction of CH_3 can be found in the ppm range.

For the $\text{N}_2\text{-H}_2$ mixing ratios of 1:3 and 3:1 the concentrations of C_2H_2 , CH_4 , HCN , NH_3 , CO , C_2H_6 , C_2H_4 , C_2N_2 , and CH_3 , measured as functions of the plasma power at the screen, are shown in figures 5.5 a) and b). Similar to the case of the $\text{N}_2\text{-H}_2$ ratio of 1:1 the concentration of NH_3 has a maximum at around $P_{\text{screen}} = 60 \text{ W}$ and that of the carbon containing reaction products increases, except that of CO . While the concentration of CO increases continually for the $\text{N}_2\text{-H}_2$ ratio of 1:1 (see figure 5.4 a)), it behaves more independently on the plasma power for the ratios of 1:3 and 3:1 (see figures 5.5 a) and b)). This further indicates that the production of CO is caused by the oxygen contamination and leakage of the reactor. Independent on the used feeding gas mixtures the concentration of CO is between $2 \cdot 10^{13}$ and $2 \cdot 10^{14} \text{ cm}^{-3}$.

It can be seen that the concentration of NH_3 is higher by a factor of 2 with a hydrogen admixture of 75 % comparing to the hydrogen admixture of 25 %. At the identical conditions, the concentration of HCN is 20 % higher.

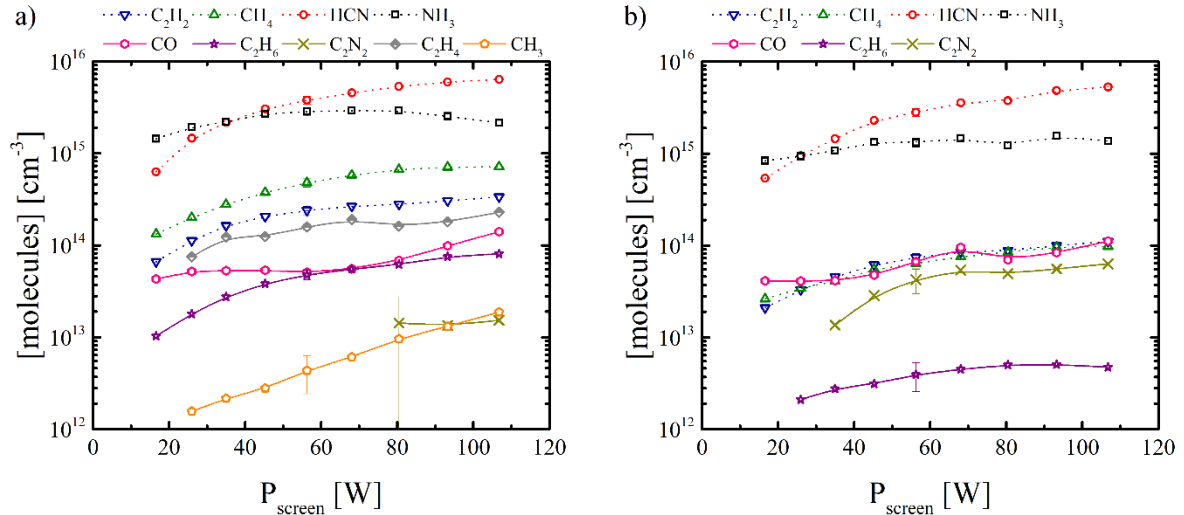


Figure 5.5 Concentrations of C_2H_2 , C_2H_4 , CH_4 , HCN , NH_3 , CO , C_2H_6 , C_2N_2 , and CH_3 measured as functions of the plasma power at the active carbon screen. a) $N_2:H_2 = 1:3$ and b) $3:1$, $p = 3$ mbar.

Comparing the usage of the two N_2 - H_2 gas mixtures (figures 5.5 a) and b)), it can be seen that CH_3 was observed nearly over the whole range of the plasma power in the case of the higher admixture of hydrogen, only, while the concentration of C_2N_2 was close to the detection limit. The latter was well measurable in the case of the higher amount of nitrogen being four times higher comparing to the lower amount of nitrogen. It has to be noted that the concentration of C_2N_2 for the $N_2:H_2$ ratio of 1:1 should be in a range of higher than $1 \cdot 10^{13} \text{ cm}^{-3}$ and lower than $6 \cdot 10^{13} \text{ cm}^{-3}$, so in between of the C_2N_2 concentrations shown in figures 5.5 a) and b). However, for the series of measurements at the N_2 - H_2 ratio of 1:1 the signal-to-noise ratio was insufficient.

Further differences of the concentrations shown in figures 5.5 a) and 5.5 b) can be seen in the hydrocarbons. On the one hand, the concentrations of CH_4 , C_2H_2 , and C_2H_6 is higher with 75 % H_2 than with 25 % H_2 in the feeding gas mixture. The reason is the surplus of H_2 , which is available for the chemical sputtering of carbon in the plasma from the solid surface of the AS leading to a higher net production rate of hydrocarbons. On the other hand, the ratio between CH_4 , C_2H_2 , and C_2H_6 changes with the feeding gas mixing ratio. While the concentration ratio of CH_4 and C_2H_6 is around 10 for the higher amount of H_2 in the feeding gas, it increases up to 20 for the lower H_2 content. Furthermore, the concentration of C_2H_2 , being the half of that of CH_4 for 75 % H_2 , reaches comparable values to the CH_4 concentration when the admixture of H_2 in the feeding gas is decreased down to 25 %.

The conversion efficiencies of C_2H_2 , C_2H_4 , CH_4 , HCN , NH_3 , CO , C_2H_6 , C_2N_2 , and CH_3 for the three N_2 - H_2 ratios of 1:3, 1:1, and 3:1 are shown in figures 5.6 a), b), and c), respectively. It can be seen, that the conversion efficiency of HCN shows a similar behaviour depending on the plasma power. It increases for plasma powers up to $P_{\text{screen}} = 45$ W and remains constant for higher power values. The conversion efficiency of NH_3 decreases with the plasma power nearly by a half an order of magnitude for all mixing ratios. The maximum values of the conversion efficiencies of NH_3 and HCN are reached for the feeding gas mixture of $N_2:H_2 = 1:1$ (see figure 5.4 a) and 5.5a), b)).

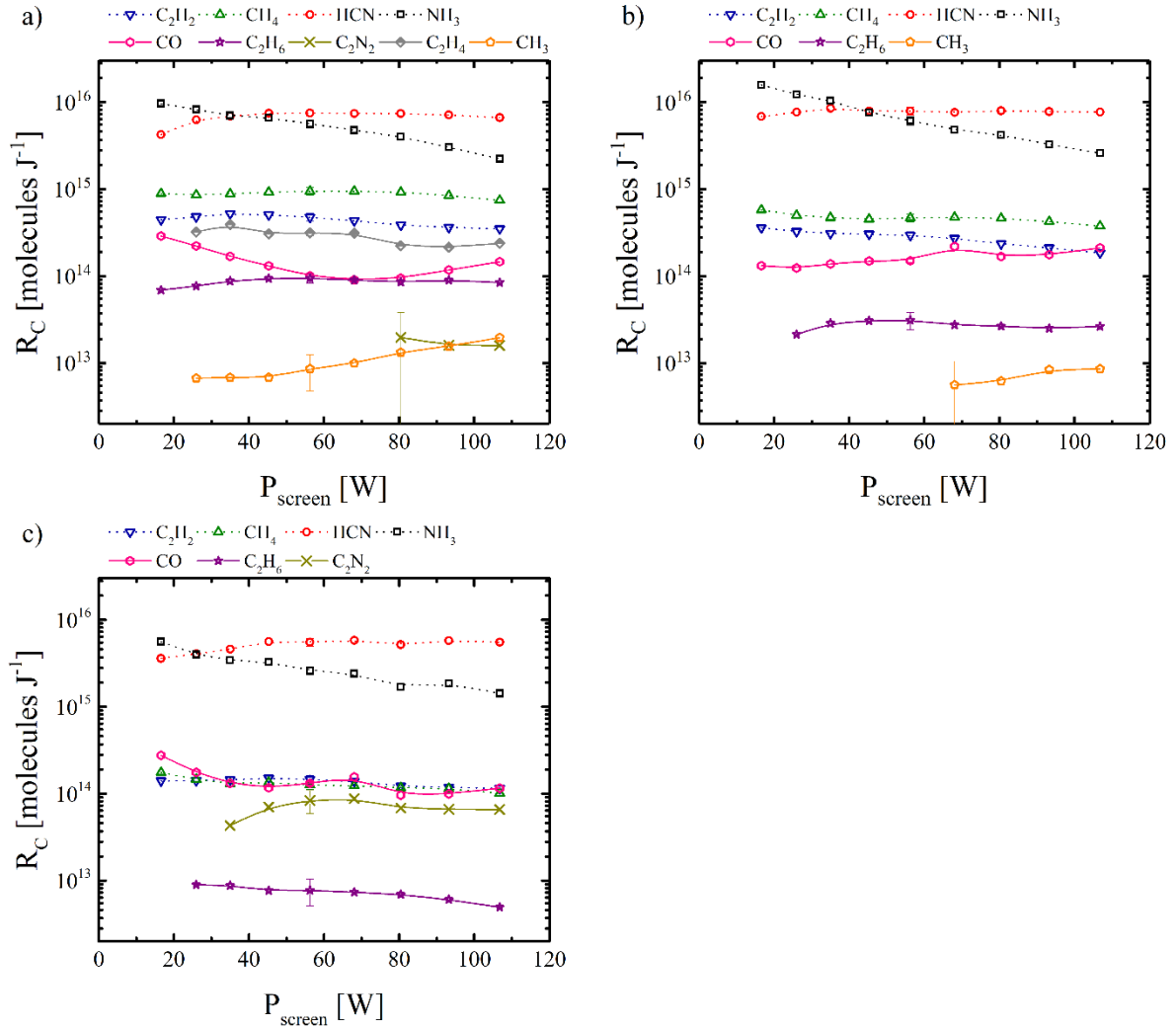


Figure 5.6 Conversion efficiencies, R_C , of C_2H_2 , C_2H_4 , CH_4 , HCN , NH_3 , CO , C_2H_6 , C_2N_2 , and CH_3 as functions of the plasma power at the active carbon screen. Conditions: a) $N_2:H_2 = 1:3$, b) $1:1$, and c) $3:1$, $p = 3$ mbar.

Also for the stable hydrocarbons, CH_4 and C_2H_2 , the conversion efficiency shows a similar behaviour. For both molecules, a decrease in dependence on the plasma power can be found, whereby the ratio of both values is changing with the N_2 - H_2 feeding gas ratio. The conversion efficiency of CH_3 increases by a factor of three with the plasma power.

While the conversion efficiency of C_2H_6 increases slightly with the plasma power for the feeding gas mixture of $N_2:H_2 = 1:3$ (see figure 5.6 a)), it is close to constant for the $N_2:H_2$ ratio of $1:1$ (see figure 5.6 b)) and decreases by a factor of nearly two for $N_2:H_2 = 3:1$ (see figure 5.6 c)).

Due to the strong changes in the chemistry for the three different N_2 - H_2 ratios of $1:3$, $1:1$, and $3:1$, also the dependencies of the concentrations of the molecular reaction products were measured for 90 % and 10 % hydrogen in the feeding gas mixture. In figure 5.7 the concentrations of C_2H_2 , CH_4 , HCN , NH_3 , CO , C_2H_6 , C_2H_4 , C_2N_2 , and CH_3 depending on the gas mixture for a screen plasma power of $P_{screen} = 93$ W and a pressure of $p = 3$ mbar are shown. As it has been found in a previous work for a screen plasma power of $P_{screen} = 33$ W, maxima in the concentrations of HCN and NH_3 can be seen for a nitrogen content around 50 % [35]. The concentrations of the hydrocarbon species increase with the amount of hydrogen (with a lower amount of nitrogen) in the gas mixture, whereas the CH_4 concentration is lower than that of C_2H_2 for the lowest amount of H_2 and exceeds it at 25 % hydrogen (75 % nitrogen) in the feed gas. Accordingly, C_2H_2 is the final hydrocarbon product when there is a lack of H_2 in the gas mixture.

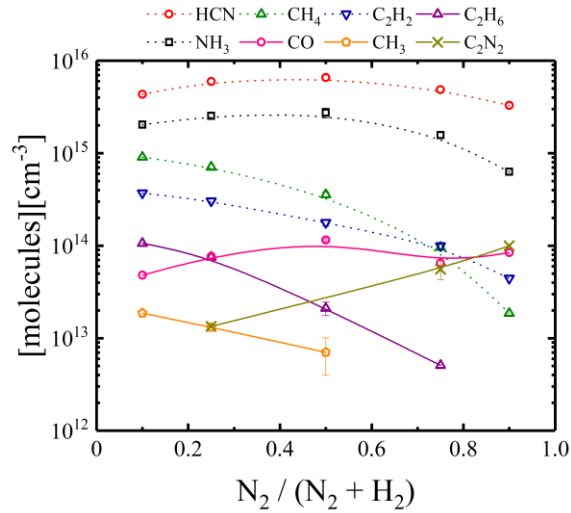


Figure 5.7 Concentrations of C_2H_2 , C_2H_4 , CH_4 , HCN , NH_3 , CO , C_2H_6 , C_2N_2 , and CH_3 measured as functions of the gas mixture. $P_{screen} = 93$ W, $p = 3$ mbar.

Noticeably, the concentration ratio of CH_4 and CH_3 remains nearly constant with the admixture of nitrogen.

Due to the contamination and the leakage of the reactor, the concentration of CO is independent on the feeding gas mixture as previously mentioned. Furthermore, the concentration of C_2N_2 decreases with the decreasing amount of N_2 .

Due to the fact, that the relatively high concentrations of the carbon-containing reaction products is caused by the erosion of the solid carbon screen due to sputtering processes and the reaction of the feeding gas with carbon, the determined molecular concentrations can be used to calculate this carbon consumption rate, C_C , of the screen, i.e. the mass of carbon, consumed by the carbon-containing products, per time unit. As it is shown in figures 5.8 a) and b), the carbon consumption rate is in a range of $C_C = 5 - 96$ mg h^{-1} and depends strongly on the plasma power. It should be mentioned, that the molecular concentrations of the reaction products have also been measured using different working pressures. The result is a similar mole fraction for all detected species independent on the pressure (not shown). The sole exception is the mole fraction of the CH_3 radical, which is decreasing with pressure because of increasing collision rates in the gas phase.

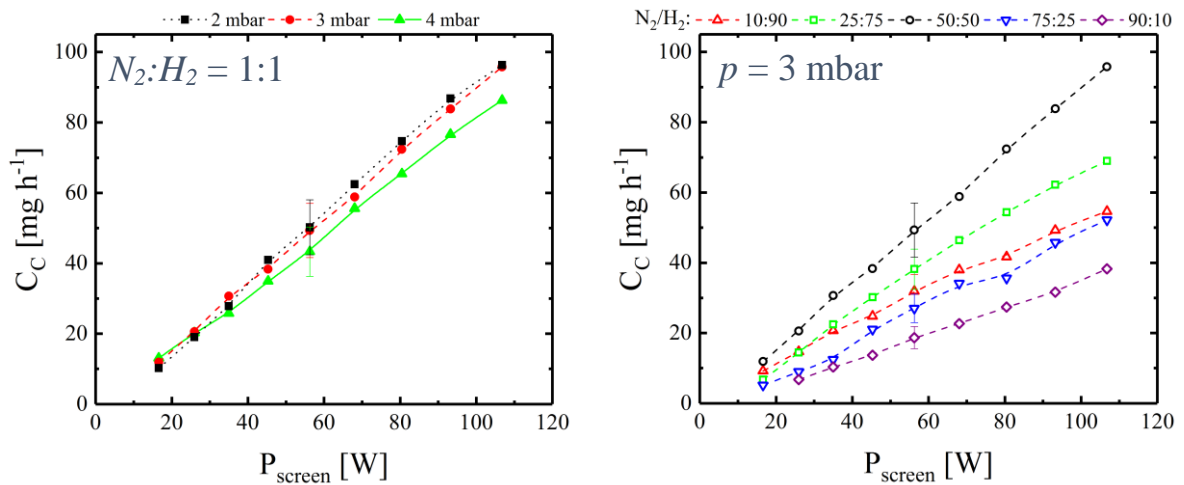


Figure 5.8 Carbon consumption rates, C_C , as functions of the plasma power at the active screen a) at a feed gas mixture $N_2:H_2 = 1:1$ for different pressures and b) at a pressure $p = 3$ mbar for different feed gas mixtures.

Finally, as presented in figure 5.8 a), this pressure independent mole fraction of the carbon containing main reaction products leads to a carbon consumption of the screen material, which is independent on the pressure, as well.

A strong influence of the carbon consumption can be found for the mixing ratio of the feeding gas, as it can be seen in figure 5.8 b). For all N_2 - H_2 gas mixtures C_C increases strongly with the plasma power. While the carbon consumption is only up to 40 mg h^{-1} for a mixing ratio of $N_2:H_2 = 9:1$ it increases up to 53 mg h^{-1} for $N_2:H_2 = 3:1$ and has a maximum of up to 96 mg h^{-1} for $N_2:H_2 = 1:1$. With a higher amount of hydrogen it decreases with values up to 70 mg h^{-1} for a N_2 - H_2 ratio of $1:3$ and up to 55 mg h^{-1} for $N_2:H_2 = 1:9$. In reference to figure 5.7, it should be clear that the values of the carbon consumption are dominated by the HCN concentration for high amounts of nitrogen while the concentrations of CH_4 and C_2H_2 become a more noticeable fraction for the higher H_2 content in the gas mixture. This leads to the fact that the carbon mass flow is similar for the N_2 - H_2 ratios of $3:1$ and $1:9$ for the highest plasma power.

The carbon consumption rate depends strongly on the size and the surface of the AS, which correlates with the plasma power as well. These values can be used to calculate the carbon consumption efficiency, E_{CC} , i.e. the consumption of carbon normalized on the plasma power, to simplify any comparison between different reactors. The carbon consumption efficiency, E_{CC} , depending on the plasma power for five different N_2 - H_2 ratios is shown in figure 5.9. In contrast to the carbon consumption itself, which just increases with the power, it can be seen that the power dependence of the efficiency differs for the different mixing ratios of N_2 and H_2 . While the carbon consumption efficiency increases with the power for nitrogen amounts of 90 % and 75 %, it stays nearly constant for a mixing ratio of $N_2:H_2 = 1:1$ for plasma powers higher than 35 W. For a content of nitrogen of 25 % the carbon consumption efficiency increases strongly between 16 and 35 W and seems to decrease slightly for plasma powers higher than 68 W. A decrease with the plasma power can be found for a gas mixing ratio of $N_2:H_2 = 1:9$.

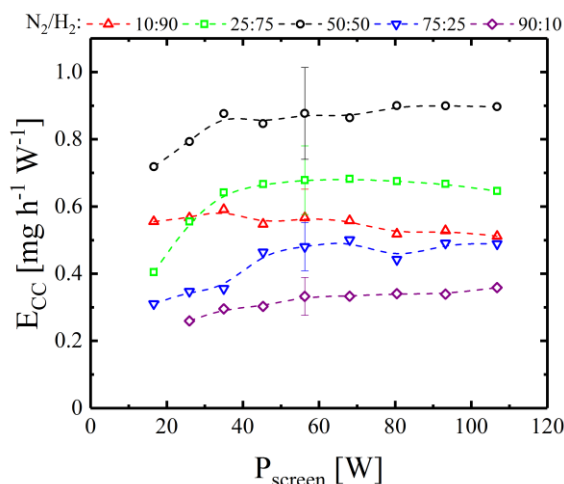


Figure 5.9 Carbon consumption efficiencies, E_{CC} , at $p = 3 \text{ mbar}$ measured as functions of the power at the AS for different N_2 - H_2 gas mixtures.

Nevertheless, as it has been found for the carbon consumption, the highest efficiency is reached for a mixing ratio of $N_2:H_2 = 1:1$ with up to $0.9 \text{ mg h}^{-1} \text{ W}^{-1}$ followed by those for the N_2 - H_2 ratios of $1:3$ and $1:9$ (see figure 5.9). For the highest plasma power, the carbon consumption efficiency for $N_2:H_2 = 3:1$ reaches nearly the same value of that for $N_2:H_2 = 1:9$, but both differ nearly by a factor of two for the lowest plasma power. The lowest values of E_{CC} are obtained for the highest content of nitrogen in the gas mixture, i.e. a N_2 - H_2 ratio of $9:1$.

Additionally to the measurements of the concentrations of the carbon containing reaction products, the weight of the carbon screen was measured with the help of a micro balance resulting in a value of

$m = 30.5$ g before the installation in PLANIMOR. After an operation time of approximately 60 hours of the screen plasma for several set of measurements at different conditions, a weight loss of about 3.9 g, including some losses by mechanical damages due to mounting and dismounting, was determined, corresponding to an average carbon consumption of the carbon screen of about 65 mg h^{-1} .

5.4 Summary and conclusions

In the present study, in the laboratory-scale plasma nitriding monitoring reactor (PLANIMOR) pulsed dc $\text{N}_2\text{-H}_2$ plasmas with the usage of an active screen made of carbon were investigated using a combined approach of quantum cascade laser absorption spectroscopy (QCLAS) and tuneable diode laser absorption spectroscopy (TDLAS). Under variation of the parameter plasma power, gas mixture, and pressure the evolution of the concentrations of eight stable molecular species, CH_4 , C_2H_2 , C_2H_4 , C_2H_6 , NH_3 , HCN , C_2N_2 , and CO , and of the CH_3 radical could be monitored using *in-situ* QCLAS and TDLAS.

Besides the determination of concentrations, the used infrared laser absorption spectroscopy (IRLAS) allowed the determination of the temperatures of some of the detected molecules. Using the line ratio method enabled the determination of the rotational temperature of CO and HCN . By analysing the Doppler broadening of the absorption line profile of the CH_3 radical the gas temperature of this radical could be determined.

With the increasing plasma power at the active screen a linear increase of the determined temperatures could be found. While the rotational temperature of HCN increased from 350 to 400 K that of CO increased up to 500 K with the plasma power. The gas temperature of the CH_3 radical ranged between 400 and 800 K being approximately 200 K lower than the rotational temperature of N_2^+ obtained by OES in a previous study [35]. Regarding these results, a strong spatial inhomogeneity of temperatures in the observed plasma-chemical processes in PLANIMOR could be shown being the main differences to those in an industrial-scale active screen plasma nitrocarburizing (ASPNC) reactor [32].

The most abundant reaction products of the conversion of the $\text{N}_2\text{-H}_2$ feed gas with the solid carbon of the active screen are HCN and NH_3 . The concentrations of the carbon-containing reaction products increases with the plasma power and that of NH_3 have a maximum for the power of the screen plasma between $P_{\text{screen}} = 40 \text{ W}$ and 60 W . All of them show a similar behaviour for different $\text{N}_2\text{-H}_2$ mixing ratios of the feed gas. The sole exception with no direct correlation to the plasma power is the concentration of CO , which is the only detected molecule being formed as a result of the contamination and of the leakage of the reactor.

With the increase of the amount of N_2 in the gas mixture, it has been found, that the concentrations of HCN and NH_3 have a maximum at an admixture of around 50 % of N_2 . Furthermore, the concentration of C_2N_2 increases by one order of magnitude with the N_2 content while that of the hydrocarbons, CH_4 , CH_3 , C_2H_2 , and C_2H_6 , decreases strongly with the decreased amount of hydrogen.

The determined molecular concentrations have been used to calculate the carbon consumption which was found to be up to 96 mg h^{-1} resulting in a carbon consumption efficiency of $0.9 \text{ mg h}^{-1} \text{ W}^{-1}$. Both calculated quantities are strongly depending on the feeding gas mixture with a maximum for a $\text{N}_2\text{-H}_2$ ratio of 1:1 and are independent on pressure.

Although the evolution of the concentrations of nine molecular species could be measured depending on a variety of parameters, this work can be considered as a further and, nevertheless, early step to reveal the plasma chemistry in ASPNC processes using an active screen electrode made of carbon. Further studies will be necessary, in particular, the adaption of the obtained results to the industrial-scale ASPNC processes and the effect on the treatment of different kinds of steels. In the different plasma regions, an improved spatial resolution, not provided by the IRLAS measurements, would be very helpful for further

insights in fundamental phenomena. Additional investigations into the temperature distributions of involved species should furthermore reduce the amount of assumptions made in that topic of discussion.

References

- [1] Spies H-J 2013 *J. Heat Treatm. Mat.* **68** 13
- [2] Haruman E, Bell T, and Sun Y 1992 *Surf. Eng.* **8** 275
- [3] Ruset C and Grigore E 2010 *Surf. Eng.* **26** 61
- [4] Howse H-J and Pistorius P G H 1999 *Surf. Eng.* **15** 476
- [5] Bell T, Sun Y, and Suhadi A 2000 *Vacuum* **59** 14
- [6] Ebersbach U *et al.* 1991 *J. Heat Treat. Mat.* **46** 39
- [7] Georges J 1999 *US Patent Specification* 5,989,363
- [8] Gallo S C and Dong H 2009 *Surf. Coat. Technol.* **203** 3669
- [9] Li C X 2010 *Surf. Eng.* **26** 135
- [10] Spies H-J *et al.* 2014 *Int. Heat Treat. Surf. Eng.* **8** 94
- [11] Burlacov I *et al.* 2014 *Int. Heat Treat. Surf. Eng.* **8** 139
- [12] Naeem M *et al.* 2017 *Mater. Lett.* **189** 213-216
- [13] Lin K, Li X, Tian L, and Dong H 2015 *Surf. Coat. Technol.* **283** 122
- [14] Lebrun J P 1996 *EU Patent Specification* 0 801 142 B1, 12.04.
- [15] Lebrun J P 2000 *US Patent Specification* 7,074,460 B2, 18.04.
- [16] Lebrun J P 2006 *EU Patent Specification* 1 274 873 B1, 19.04.
- [17] Somers M and Christiansen T L 2015 Gaseous processes for low temperature surface hardening of stainless steel. In: *Thermochemical Surface Engineering of Steels*. Ed. E. J. Mittemeijer and M. Somers, Elsevier 581
- [18] Schlüter M, Hopf C, and Jacob W 2008 *New J. Phys.* **10** 053037
- [19] Jacob W, Hopf C, and Schlüter M 2005 *Appl. Phys. Lett.* **86** 204103
- [20] Hopf C and Jacob W 2005 *J. Nucl. Mater.* **342** 141
- [21] Hopf C, von Keudell A and Jacob W 2003 *J. Appl. Phys.* **94** 2373
- [22] Jacob W, Hopf C, and Schlüter M 2006 *Phys. Scr.* **T124**, 32
- [23] Schwarz-Selinger T, von Keudell A, and Jacob W 1999 *J. Appl. Phys.* **86** 3988
- [24] Crespi A E *et al.* 2011 *Mater. Lett.* **65** 2985
- [25] Burlacov I *et al.* 2012 *Surf. Coat. Technol.* **206** 3955
- [26] Hamann S *et al.* 2013 *Plasma Sources Sci. Technol.* **22** 055022
- [27] Hannemann M *et al.* 2013 *Surf. Coat. Technol.* **235** 561
- [28] Hamann S *et al.* 2015 *J. Phys. D: Appl. Phys.* **48** 345204
- [29] Röpcke J *et al.* 2016 *Photonics* **3** 45
- [30] Lang N *et al.* 2011 *Jpn. J. Appl. Phys.* **50** 08JB04
- [31] Hamann S *et al.* 2015 *Rev. Sci. Instrum.* **86** 123503
- [32] Hamann S *et al.* 2015 *Contrib. Plasma Phys.* **55** 689
- [33] Burlacov I *et al.* 2016 *HTM J. Heat Treat. Mat.* **71** 141-147
- [34] Burlacov I *et al.* 2017 *HTM J. Heat Treat. Mat.* **72** 254-259

- [35] Hamann S *et al.* 2017 *J. Appl. Phys.* **121** 153301
- [36] White J U 1942 *J. Opt. Soc. Am.* **32** 285
- [37] Röpcke J *et al.* M 2000 *Rev. Sci. Instrum.* **71** 3706
- [38] Lopatik D *et al.* 2012 *Meas. Sci. Technol.* **23** 115501
- [39] Rothman L S *et al.* 2005 *J. Quant. Spectrosc. Radiat. Transfer* **96** 139-204
- [40] Stancu G D, Röpcke J, and Davies P B 2005 *J. Chem. Phys.* **122** 014306
- [41] Stancu G D *et al.* 2005 *Contrib. Plasma Phys.* **45** 358
- [42] Jacquinet-Husson N *et al.* 2016 *J. Mol. Spectrosc.* **327** 31-72
- [43] Hempel F *et al.* 2012 *Plasma Sources Sci. Technol.* **21** 055001
- [44] Mechold L *et al.* 2001 *Plasma Sources Sci. Technol.* **10** 52
- [45] Naeem M *et al.* 2016 *Surf. Coat. Technol.* **300** 67-77

6 Application of a FC for investigation of a laboratory-scale ASPN reactor using an AS made of CFC⁵

6.1 Introduction

The determination of temperatures of the detected molecular species is a key challenge in LAS applied to plasmas, as on the one hand, a thermal equilibrium cannot be generally assumed and on the other hand, the line strength of a transition is dependent on the rotational temperature. In section 4, for the case of an industrial-scale ASPNC process, several studies found a thermal equilibrium between species and the sample temperature measured with a thermocouple at the centre of the reactor vessel [1, 2]. However, for the laboratory-scale PLANIMOR, a deviation of the temperature of CO and HCN molecules was found [3]. Accordingly, due to small overall plasma volume and linear principle of construction of PLANIMOR, a close study of the temperatures is required. For the determination of the rotational temperature of a vibrational band of a single species, two or more transitions of this species are plotted in the natural logarithm of their population density as a function of the lower level energy and subsequently linearly fitted. This method is called the Boltzmann plot, whereby the rotational temperature is then derived from the slope of the linear fit.

Conducting this study with conventional laser sources, such as lead-salt TDLs and EC-QCLs, typically results in a low number of transitions, requiring considerable amounts of measurement time for a single species, with a large effort required to identify the spectral positions. However, by use of a FC source, a self-calibrated broadband spectrum can be measured, thus reducing the measurement time and allowing for precise identifications. In chapter 3.4, a general introduction to FC sources, their principles of operation, characteristics, and applicable detection schemes were provided.

In the present chapter, the interrogated plasma is maintained at 3 mbar, at a mixed feed gas flow of 10 sccm H₂ and 10 sccm N₂, and a fixed plasma power between 26 and 128 W applied to an AS made of CFC. As means of interrogation, a FC with a spectral coverage between 2750 and 3450 cm⁻¹ was combined with a Michelson interferometer and recorded using a balanced detector. The resulting interferograms were matched to the repetition rate f_{rep} of the FC to counteract the truncation-induced ILS, a method described in general terms in section 3.4.2. Furthermore, by a process called interleaving, multiple broadband spectra with different sampled frequencies were combined, to further enhance the resolution. Finally, individual transitions were fitted with Gaussian profiles.

This way, hundreds of transitions were detected and assigned to the molecular species CH₄, C₂H₂, C₂H₆, HCN, and NH₃, and their respective rovibrational bands. Subsequently, the rotational temperatures were determined by the Boltzmann plot method. In addition, the translational temperatures of each band were derived from the translational temperatures determined by line profile analysis of the individual transitions. Furthermore, the concentrations of all species were determined and compared with the values published in [3].

⁵ This chapter is intended for a future publication. Contributing authors include: Puth A, Lang N, Maslowski P, Nishiyama A, Kowzan G, Moreira P W P jr., Klose S, Röpcke J, and van Helden J H.

6.2 Experimental

In figure 6.1, the experimental setup is schematically shown with the FC source and the laboratory-scale PLANIMOR on the left and the Michelson interferometer on the right. The emission of the FC is coupled into a single-mode mid-infrared optical fibre made of ZrF₄ via an aspheric fibre coupler and coupled out using an OAP. The optical fibres were used to reduce atmospheric absorption and improve the stability of the alignment. After passing the MPO of PLANIMOR and thus interrogating the afterglow region of the discharge, the emission is again transferred with an optical fibre to the Michelson interferometer. The collimated beam is split with a beamsplitter (BS), resulting in a reflected beam (R beam) and a transmitted beam (T beam). Both arms of the interferometer end in retroreflectors, which are mounted back-to-back on a moving stage, providing an OPD four times the travel distance of the stage. Interference is ensured by spatial overlap of the returning beams, and is recorded on both arms with a MCT balanced detector. Before a measurement set, the balancing of the detector is calibrated according to the manufacturer's instructions. For the monochrome HeNe reference laser, a beam propagation parallel to the FC emission is given, with a vertical displacement of 12 mm. However, for the reference laser only the interference of a single interferometer arm is recorded and the respective detector is omitted from the schematic in figure 6.1 for clarity. Sampling is synchronized with the zero-crossings of the sinusoidal interference signal of the frequency-stabilized reference wavelength $\lambda_{\text{ref}} = 632.99 \text{ nm}$.

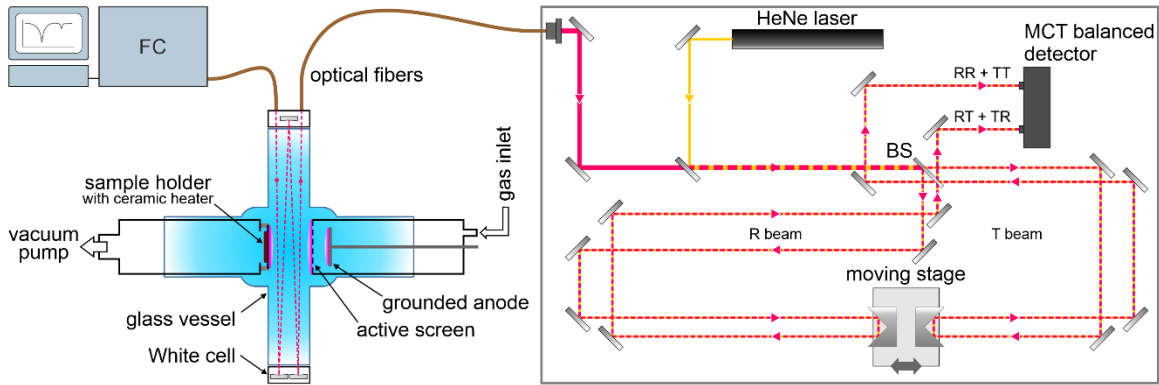


Figure 6.1 Schematic top-view of the experimental arrangement at PLANIMOR combined with a FC source (left top) and a Michelson interferometer (right). Both the reflected (R beam) and the transmitted (T beam) arms of the interferometer and their combinations are marked. The HeNe laser is used as a sampling reference of the interferometer and propagates parallel to the FC emission with a vertical displacement of 12 mm. The corresponding optical detector is not depicted. The White cell is rotated by 90° for illustrative purposes.

The comb source used in this study is a mode-locked fibre-based femtosecond FC already presented in small detail in section 3.4.1. It has an output power of approximately 170 mW, attenuated with an angled linear polarizer placed before the first fibre. This way the power at the balanced detector is kept below the level of saturation of 1 mW. The spectral coverage of the FC ranges from 2750 to 3450 cm^{-1} and is shown in figure 3.11. Due to the DFG process generating the FC at 3114 nm from two combs at 1040 nm and 1560 nm, respectively, the carrier-envelope offset f_0 has a fixed value of zero. Thus, for interleaving, the repetition rate f_{rep} of the FC is varied in order to sample different frequencies, according to equation (6.1):

$$f_{\text{rep}} = 250 \text{ MHz} + n \cdot 173.75 \text{ Hz}, \quad n \in [0, 1, 2, 3] \quad (6.1)$$

Concerning the travel of the moving stage, a distance of 0.4 m is set to guarantee a travel distance of 0.3 m at a constant speed of 120 mm s^{-1} . Synchronization between the moving stage and the start of measurement is achieved using a light barrier. Consequently, the interferograms are measured approximately symmetrically around the centre burst. Measurements are taken with a sampling rate of

2 MS s⁻¹ at a travel speed of 120 mm s⁻¹ of the moving stage, for a total of 4 MS. During the return of the stage, no sampling takes place. For averaging, 50 interferograms are collected per measurement condition, in total requiring 7 minutes per repetition rate and plasma setting.

Extensive descriptions of PLANIMOR can be found in references [4, 5] and chapter 5.2 of this thesis. For the interrogated plasma, a gas flow of 10 sccm H₂ and 10 sccm N₂ at a reactor pressure of 3 mbar is maintained. The plasma power at the AS made of CFC is stabilized to $P_{AS} = 26, 46, 91, \text{ or } 128 \text{ W}$. With use of a MPO of White type, an absorption length of 1.90 m is reached, passing the afterglow of the discharge.

6.3 Methods

Table 6.1 presents a set of parameter values used as initials for the matching process. With q being the number of samples per reference wavelength λ_{ref} introduced in equation (3.16) and the refractive index n for humid air at λ_{ref} and 3.35 μm . Equation (3.16) is reproduced in equation (6.1) and determines the number of elements N_0 remaining in a matched interferogram after truncation [8]:

$$N_0 = \text{round}\left(q \frac{c}{2 \cdot \lambda_{ref} \cdot f_{rep}}\right) \quad (6.1)$$

In order to account for wavelength-dependent atmospheric effects the equation further reads:

$$N_0 = \text{round}\left(q \frac{c}{2 \cdot \lambda_{ref} \cdot f_{rep}} \cdot \frac{n(3.35 \mu\text{m})}{n(\lambda_{ref})}\right) \quad (6.2)$$

However, this fails to take into account changes in humidity affecting the refractive indices. Therefore, an interval of discrete values centred on N_0 is assumed, with each corresponding to a truncation process. Next, the absolute of a FFT is applied to each resulting truncated interferogram, in turn resulting in multiple spectra. By fitting to isolated, low-pressure absorbance features of the plasma, tabulated in table 6.2, the best-matched case is manually determined on basis of the lowest residuals of the fits.

Table 6.1 Values used for the matching process.

Parameter	Value	Reference
q	2	
λ_{ref} [nm]	632.99091788	Datasheet
$n(\lambda_{ref})$	1.000272452	[6]
$n(3.35 \mu\text{m})$	1.000267118744879	[7]

Table 6.2 Spectral positions and associated species of transitions used for determination of the best-matched case. Data taken from the HITRAN database [9].

Species	Spectral position [cm ⁻¹]	Reference
CH ₄	2927.076189	[10]
CH ₄	3028.752260	[11]
CH ₄	3113.707320	[11]
CH ₄	3113.711931	[11]
HCN	3206.935939	[12]
HCN	3300.927340	[13]
HCN	3300.973687	[13]

Due to concerns of the long-term stability of the transmission signal, determination of the absorbance spectrum by relating the transmission spectra of the plasma in measurement condition and of the vacuum

background condition was not considered. Accordingly, the alternative approach of defining a local background by polynomial fitting of transition-free spectral ranges was used to piecewise assemble the interleaved absorbance spectrum from the transmission spectrum of each repetition rate. If not stated otherwise, presented spectra are interleaved.

However, a unique challenge lays in large number of transitions contained in the spectral range and subsequent handling of large quantities in information. Extracts of the HITRAN database for all isotopes of the species CH₄, C₂H₂, C₂H₄, C₂H₆, CO₂, H₂, H₂CO, H₂O, HCN, NH₃, NO, N₂O, NO₂, OH, and O₃ were referenced from a script to identify fitted absorption features within the spectral range of 2700 to 3500 cm⁻¹. Final association of the fit parameters with a specific transition occurred on the user's selection. Furthermore, the baseline definition required for the Gaussian fit was applied to the spectra of the four plasma power settings simultaneously, reducing the time required for analysis. After inspection, each individual fit was saved, as well as a list of fit parameters on basis of the HITRAN extracts.

For determination of the rotational temperatures, the populations of states n with consideration of their statistical weight of the lower level g'' were plotted as a function of their lower level energy E'' . The populations are derived from:

$$n = \frac{\int_{-\infty}^{\infty} \ln\left(\frac{I_0}{I}\right) dv}{\sigma_{int} \cdot L}, \quad (6.3)$$

with the numerator being the integral absorbance of the transition in cm⁻¹, as introduced in equation (3.7), and L being the length of absorption in cm. Further, the cross section

$$\sigma_{int} = \frac{g'}{g''} \cdot \frac{A_{ij}}{\nu_{ij}^2} \cdot \frac{1}{8 \cdot \pi \cdot c}, \quad (6.4)$$

where g' is the upper statistical weight, A_{ij} is the Einstein coefficient of the transition ij in s⁻¹, and the wavenumber of the transition ν_{ij} in cm⁻¹. Finally, the data of a vibrational band is plotted this way and subsequently fitted with a linear model, whereby the rotational temperature T_{rot} of the vibrational band is determined by:

$$T_{rot} = - \frac{1}{k_B \cdot m}, \quad (6.5)$$

with m being the slope of the fit in cm and k_B being the Boltzmann constant in cm⁻¹ K⁻¹ with a value of 0.6950356.

With the rotational temperatures, the line strengths of every measured transition were determined by application of equation (6.6) [9]:

$$S_{ij}(T) = S_{ij}(T_{ref}) \cdot \frac{Q(T_{ref})}{Q(T)} \cdot \frac{\exp\left(-\frac{h \cdot c \cdot E''}{k_B \cdot T}\right)}{\exp\left(-\frac{h \cdot c \cdot E''}{k_B \cdot T_{ref}}\right)} \cdot \frac{[1 - \exp\left(-\frac{h \cdot c \cdot \nu_{ij}}{k_B \cdot T}\right)]}{[1 - \exp\left(-\frac{h \cdot c \cdot \nu_{ij}}{k_B \cdot T_{ref}}\right)]}, \quad (6.6)$$

where Q is the total internal partition sum, available in tabularised form from the HITRAN database. Furthermore, the Planck constant h and Boltzmann constant k_B are used.

6.4 Results and discussion

6.4.1 General remarks

An overview absorbance spectrum of a nitrocarburizing plasma in PLANIMOR with a flow of 10 sccm H_2 and 10 sccm N_2 , a pressure of 3 mbar, and a plasma power of 128 W applied to an AS made of CFC is shown in figure 6.2. Additionally presented are simulations of CH_4 , C_2H_2 , C_2H_6 , HCN, and NH_3 at a rotational temperature of 350 K, manually matched to the amplitude of their corresponding features and plotted negatively for clarity [9, 14]. Incidentally, the $\nu_2+\nu_3$ combination band of HCN, with the corresponding band head at 2805.585 cm^{-1} , is not included in the HITRAN database and was identified by use of Jørgensen and Maki *et al.* [13, 15].

Absorbance features with an amplitude exceeding 0.7 are not considered in the determination of temperatures and concentrations, due to concerns about the non-linearity of the detector and the applied fit model at high values of absorbance.

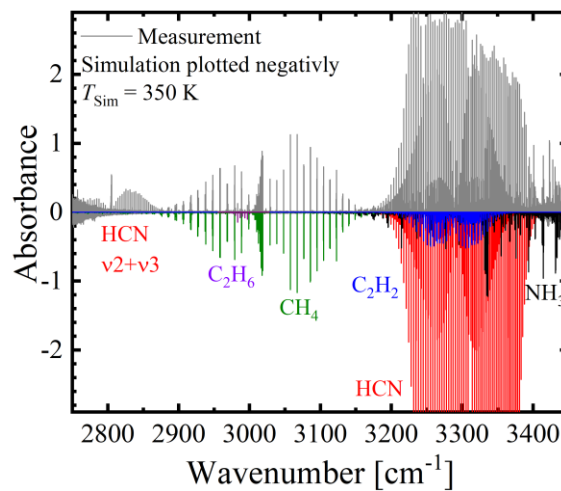


Figure 6.2 Absorbance spectrum of a nitrocarburizing plasma in PLANIMOR and simulations of CH_4 , C_2H_2 , C_2H_6 , HCN, and NH_3 at 350 K plotted negatively. Conditions: $\Phi_{\text{Total}} = 10\text{ sccm H}_2 + 10\text{ sccm N}_2$, $p = 3\text{ mbar}$, $P_{\text{AS}} = 130\text{ W}$, CFC-AS in use.

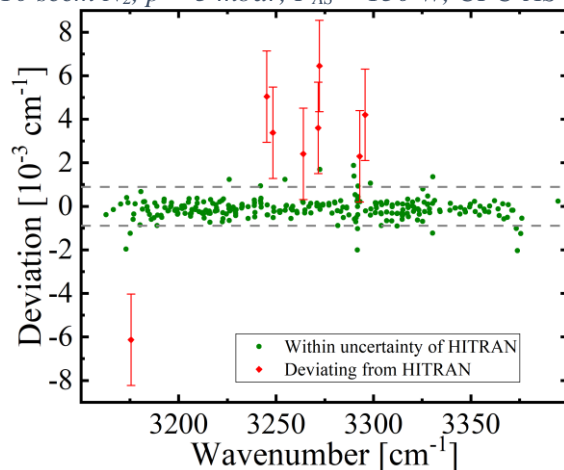


Figure 6.3 Deviations of fit centre wavenumbers to corresponding database values as a function of the spectral position of $\text{H}^{12}\text{C}^{14}\text{N}$. Margins of error are only presented for outliers (red) for clarity. The statistical standard deviation is given in grey dashed lines. Conditions: see figure 6.2.

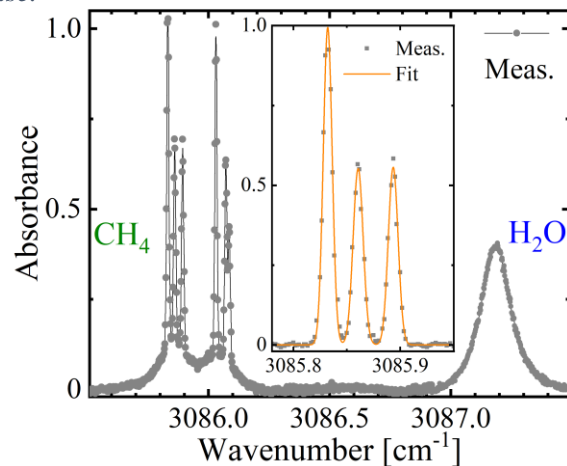


Figure 6.4 Absorbance spectrum including atmospheric H_2O and CH_4 lines, as well as low-pressure CH_4 lines. Inset is a zoom-in with the baseline fitted to the atmospheric absorption, resulting in only the low-pressure absorbance of CH_4 , shown with three Gaussian fits. Conditions: see figure 6.2.

With use of four different repetition rates at approximately 250 MHz or 0.008339 cm^{-1} , the average distance between sampled frequencies is 62.5 MHz, equivalent to 0.002085 cm^{-1} . This can be assumed as the uncertainty of the determined centre wavelength for fitted transitions. To evaluate the quality of the x-axis calibration, figure 6.3 plots the deviations of determined centre wavenumbers from the corresponding values as to the HITRAN database, as a function of the spectral position of all 273 fitted transitions of $\text{H}^{12}\text{C}^{14}\text{N}$ at a plasma power of 130 W. The error margins, the sum of the spectral resolution and the uncertainty of 10^{-4} cm^{-1} of the values given by HITRAN, are only depicted for the eight outliers for clarity.

A great majority of fits agree with the HITRAN values, with no clear trend of the outliers. Possible explanations for outliers are low signal-to-noise ratios and non-identified underlying line profiles of other transitions.

Furthermore, even with the use of optical fibres, the beam path still included approximately 4 m of absorption length at atmospheric conditions, resulting in strongly pressure broadened absorption features of predominantly H_2O and CH_4 . In some spectral regions, this prevents the analysis of transitions at plasma conditions, due to distortion or signal loss. Figure 6.4 presents the spectral range around 3086 cm^{-1} , with broad features of CH_4 and H_2O at atmospheric conditions and narrow features of CH_4 originating from the interrogated afterglow volume. As the inset shows, by assuming the atmospheric feature as part of a baseline, fitting of the low-pressure transitions can still be possible. Inset and main plot share the same axis labelling.

6.4.2 Rotational and translational temperatures

For the determination of rotational and translational temperatures, the observed transitions require association to their respective vibrational band based on the HITRAN database [9]. Table 6.3 lists the number of recorded lines grouped for their respective bands and isotopic species. Further, the ranges of the lower level energy of the transitions E'' and the minimum lower level energy are given. References to the database contributions are omitted, due to the large number of lines involved.

As can be seen in table 6.3, for $\text{H}^{12}\text{C}^{14}\text{N}$ only a limited number of transitions originating in the ground state are available, with more ground state transitions available for both isotopes $\text{H}^{13}\text{C}^{14}\text{N}$ and $\text{H}^{12}\text{C}^{15}\text{N}$. This is due to line saturation of transitions at small values of the lower level energy. Accordingly, in figure 6.5 a) a gap can be observed in lower level energies between 0 and 1000 cm^{-1} , which is not seen in the hot band originating in 0110 presented in figure 6.5 b). The red lines in figure 6.5 are linear fits including all available transitions, with the blue curve in figure 6.5 a) excluding the eight transitions with the highest lower level energy, marked in the plot with a cyan rectangle. Indicated margins of error consider the uncertainties reported in the HITRAN database, the margins of error in the resulting rotational temperatures T_{rot} are based on the $2\text{-}\sigma$ certainty interval of the linear fit, and margins of error in the translational temperature T_{D} on the standard deviations of the individual temperatures as determined by line profile analysis of each transition.

The difference of 35 K in temperature shows the significant influence of transitions originating in higher energy states, resulting in an overall higher rotational temperature. In case of figure 6.5 b), the same observation can be made, as the linear fit underestimates the state populations at the extremes of the available lower level energy range, while simultaneously overestimating the middle, albeit generally matching within the margins of error.

Table 6.3 Number of recorded lines, their vibrational band assignment, ranges of lower level energy E'' , and minimum lower level energy for the respective isotopic species. Identification based on the HITRAN database [9].

Species	Vibrational quantum number assignments	Number of lines	Range of E'' [cm^{-1}]	Minimum E'' [cm^{-1}]
$^{12}\text{C}_2\text{H}_2$	001 000 +u \leftarrow 000 000 +g	43	2 – 1166	0
	010 110 +u \leftarrow 000 000 +g	45	2 – 1166	0
	010 211 u \leftarrow 000 000 g	9	626 – 971	0
	others	15		
$^{12}\text{CH}_4$	0010 1F2 \leftarrow 0000 1A1	249	0 – 1252	0
	0101 1F2 \leftarrow 0000 1A1	28	31 – 1594	0
	0200 1E \leftarrow 0000 1A1	8	293 – 1994	0
	others	10		
$\text{H}^{12}\text{C}^{14}\text{N}$	1000 \leftarrow 0000	22	0 – 2915	0
	1110 \leftarrow 0110	137	721 – 2685	715
	1200 \leftarrow 0200	42	1414 – 2614	1411
	1220 \leftarrow 0220	72	1435 – 2805	1435
$\text{H}^{13}\text{C}^{14}\text{N}$	1000 \leftarrow 0000	46	0 – 1251	0
$\text{H}^{12}\text{C}^{15}\text{N}$	1000 \leftarrow 0000	29	3 – 1083	0
$^{14}\text{NH}_3$	1000 00 0A2 \leftarrow 0000 00 0A1	57	19 – 884	0
	1000 00 0A1 \leftarrow 0000 00 0A2	56	0 – 884	0
	0010 10 1E \leftarrow 0000 00 0A1	29	103 – 954	0
	0010 10 1E \leftarrow 0000 00 0A2	36	60 – 1008	0
	0002 02 2E \leftarrow 0000 00 0A1	29	19 – 592	0
	0002 02 2E \leftarrow 0000 00 0A2	34	0 – 856	0
	0002 00 0A2 \leftarrow 0000 00 0A1	12	19 – 790	0
	0002 00 0A1 \leftarrow 0000 00 0A2	19	45 – 1170	0
	others	1		

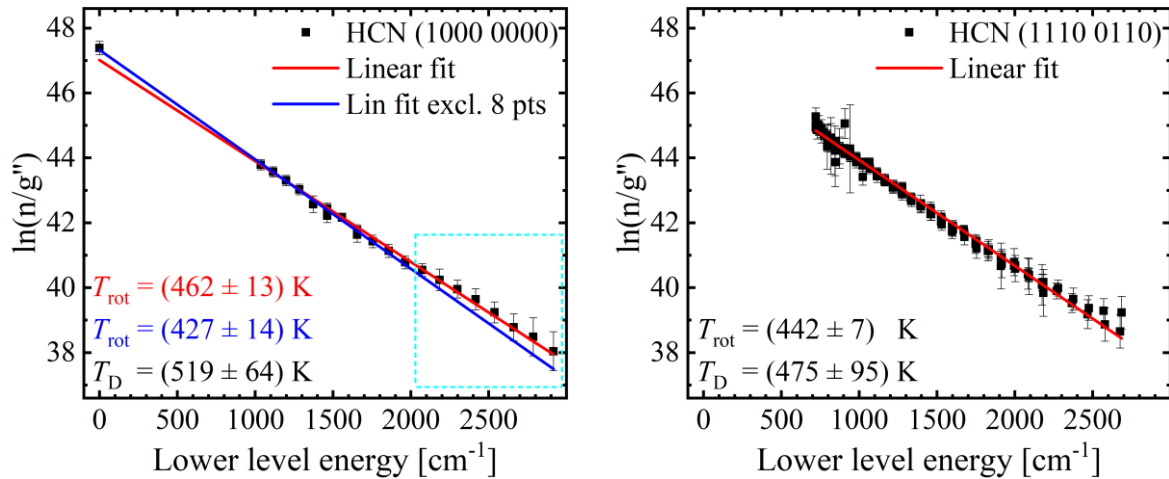


Figure 6.5 Boltzmann plot for the a) 1000 \leftarrow 0000 and the b) 1110 \leftarrow 0110 vibrational bands of $\text{H}^{12}\text{C}^{14}\text{N}$, with full-range linear fits (red) and a limited-range linear fit (blue). Resulting rotational and translational temperatures are given. Conditions: $\Phi_{\text{Total}} = 10 \text{ sccm H}_2 + 10 \text{ sccm N}_2$, $p = 3 \text{ mbar}$, $P_{\text{AS}} = 130 \text{ W}$, CFC-AS in use.

In order to gain insight on the rotational temperature of HCN ground state transitions, the two isotopes $\text{H}^{13}\text{C}^{14}\text{N}$ and $\text{H}^{12}\text{C}^{15}\text{N}$ are studied, with the assumption of a thermal equilibrium between the three isotopes of HCN. Due to the lower terrestrial abundance of 1.1 and 0.4 %, respectively, the overall absorbance is reduced [9]. Figure 6.6 shows the Boltzmann plot for a) $\text{H}^{13}\text{C}^{14}\text{N}$ and b) $\text{H}^{12}\text{C}^{15}\text{N}$ ground state transitions with linear fits and corresponding temperatures. The temperatures derived from both Boltzmann plots agree well, both in rotational and translational temperatures. However, in particular the

rotational temperatures are approximately 100 K lower than the corresponding rotational temperature of $\text{H}^{12}\text{C}^{14}\text{N}$, shown in figure 6.5 a). This difference can be explained by the lower level energy of the sampled transitions. For the predominant isotope, nearly all transitions originating in the ground state have a lower level energy in excess of 1000 cm^{-1} , in contrast to the two heavier isotopes, where the lower level energy of interrogated transitions at most reaches 1250 cm^{-1} .

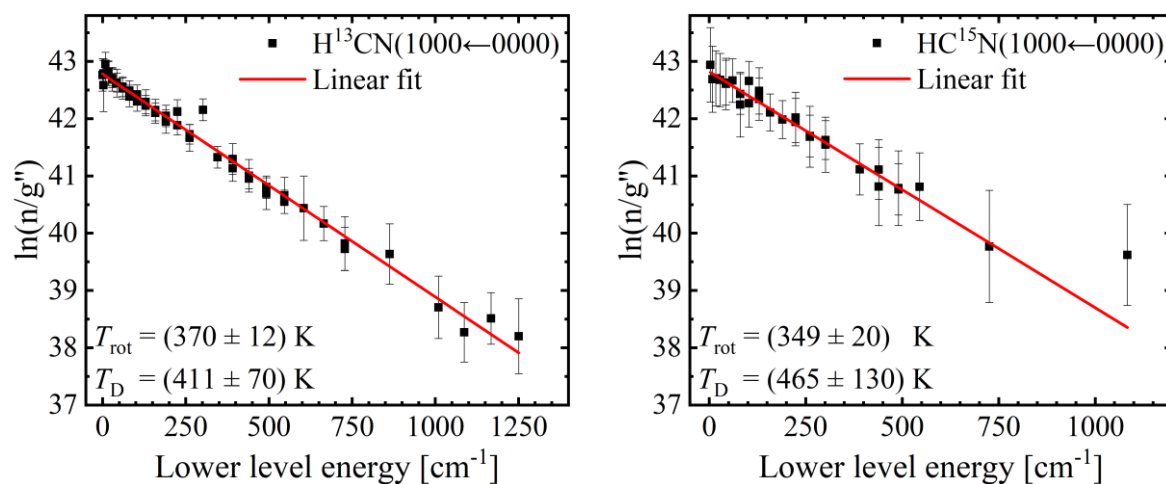


Figure 6.6 Boltzmann plot for the $1000 \leftarrow 0000$ vibrational bands of a) $\text{H}^{13}\text{C}^{14}\text{N}$ and b) $\text{H}^{12}\text{C}^{15}\text{N}$, and corresponding linear fits (red). Conditions: see figure 6.5.

As the population at elevated lower level energy is overrepresented in figure 6.5 a), the resulting rotational temperature fails to account for the large bulk of the overall population at lower level energies smaller than 1000 cm^{-1} . Accordingly, rotational temperatures resulting from the less prevalent isotopes $\text{H}^{13}\text{C}^{14}\text{N}$ and $\text{H}^{12}\text{C}^{15}\text{N}$ are assumed to be representative of the rotational temperature of vibrational transitions originating in the ground state of HCN. This results in figure 6.7, comparing rotational and translational temperatures of different bands of the HCN isotopes at 130 W plasma power at the AS.

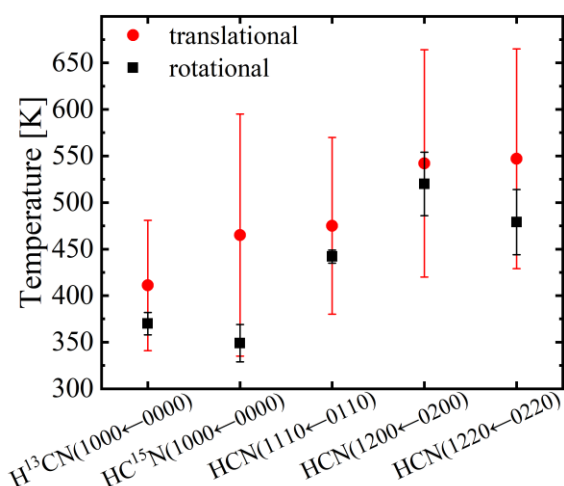


Figure 6.7 Rotational and translational temperatures for vibrational bands of HCN isotopes. Conditions: see figure 6.5

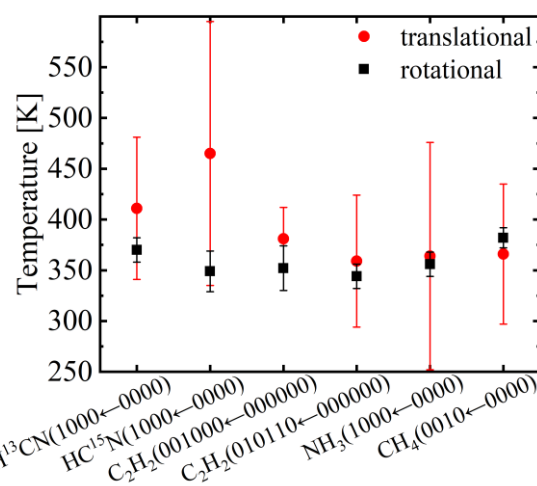


Figure 6.8 Rotational and translational temperatures for vibrational bands originating in the ground state of CH_4 , C_2H_2 , HCN, and NH_3 . Conditions: see figure 6.5

In the first place, the increased rotational temperature of the hot bands of HCN, originating in the 0110, 0200, and 0220 vibrational state, in comparison to the ground state transitions can be noted. Quantitatively, the ground states thermalize around 360 K, the rotational temperature of the band originating in the 0110 state is 442 K, and the two remaining hot bands can be approximated at 500 K. This trend can be correlated to the minimum lower level energy of the respective bands given in table 6.3. A similar increase can be seen in the translational temperature, however due to the strongly

increased margins of error compared to those of the rotational temperature, clear conclusions cannot be drawn.

Figure 6.8 shows a comparison of the temperatures of the ground state transitions of CH₄, C₂H₂, HCN, and NH₃. Concerning the rotational temperatures, a thermal equilibrium between the presented species has been reached at approximately 360 K, while the average of the translational temperatures is slightly higher at 380 K. Again, the increased margins of error of the translational temperatures are observed, resulting in an agreement between determined rotational and translational temperatures, with a significantly lower uncertainty of the values of rotational temperatures. As the rotational temperatures are derived from the integrated absorbance, they are less sensitive to broadening mechanisms such as the instrumental broadening or a low sampling of the line profile.

Finally, figure 6.9 presents the rotational temperatures of ground state bands as functions of the plasma power applied to the AS. This includes rotational temperatures of CH₄, C₂H₂, HCN, and NH₃, as well as the average of the ground state rotational temperatures (brown curve) and the rotational temperature of HCN as determined in Puth *et al.* [3]. Comparing the two curves, a good agreement can be found at low values of plasma power. Both near linearly increase with increasing power at the AS, with a slight difference in slope and offset, with the average of the ground state rotational temperatures increasing from 310 K at 25 W plasma power to 380 K at 130 W. Of particular interest is the close agreement of the rotational temperature of H¹²C¹⁴N as determined in this study (red solid dot) with the temperature curve previously published, since the temperature of this isotope diverges from the group of other rotational temperatures of ground states at plasma powers in excess of 50 W.

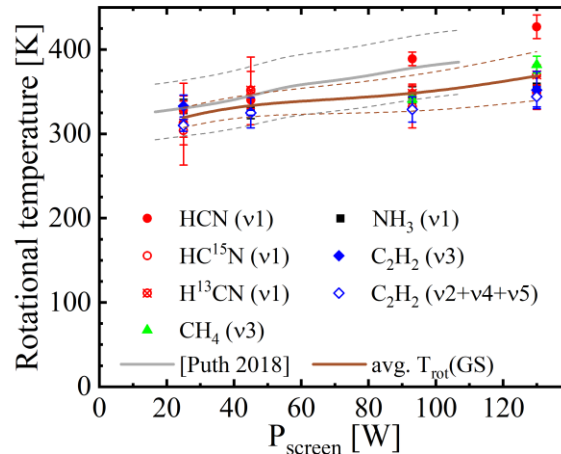


Figure 6.9 Rotational temperatures of bands originating in the ground state of CH₄, C₂H₂, H¹²C¹⁴N, H¹³C¹⁴N, H¹²C¹⁵N, and NH₃ as functions of the plasma power applied to the AS. Two curves indicate the rotational temperature determined in Puth *et al.* (grey) and the average of the ground state rotational temperature (brown), with their respective uncertainties (dashed lines)[3]. Conditions: $\Phi_{Total} = 10 \text{ sccm H}_2 + 10 \text{ sccm N}_2$, $p = 3 \text{ mbar}$, CFC-AS in use.

6.4.3 Concentrations

For the determination of the absolute concentrations of CH₄, C₂H₂, HCN, and NH₃, the average rotational temperatures of the ground state transitions as shown in figure 6.9 were used. With equation (6.6), the absolute concentrations of CH₄, C₂H₂, H¹²C¹⁴N, and NH₃ were determined for the four measurement conditions at a plasma power at the AS of 26, 46, 91, and 128 W, and are presented in figure 6.10 as functions of the plasma power. The pointed lines are B-splines of the concentrations published in Puth *et al.* measured using LAS with EC-QCLs [3], whereas the solid data points are measurements of the current study. For CH₄, C₂H₂, and in particular HCN a good agreement between both measurements can be seen. However, for NH₃ the agreement is restricted to low values of plasma powers, with the concentrations measured in this study reaching a plateau in concentration at $4 \cdot 10^{15} \text{ cm}^{-3}$.

For the equivalent curve measured with EC-QCL sources, a maximum concentration of $3 \cdot 10^{15} \text{ cm}^{-3}$ at approximately 40 W plasma power with decreasing concentrations was reported, with decreasing values for both lower and higher values of applied power. On the other hand, this discrepancy is only just above the combined margins of error, with the concentration of NH_3 at 93 W measured with a FC being approximately 30 % higher than the same concentration being measured using EC-QCLs.

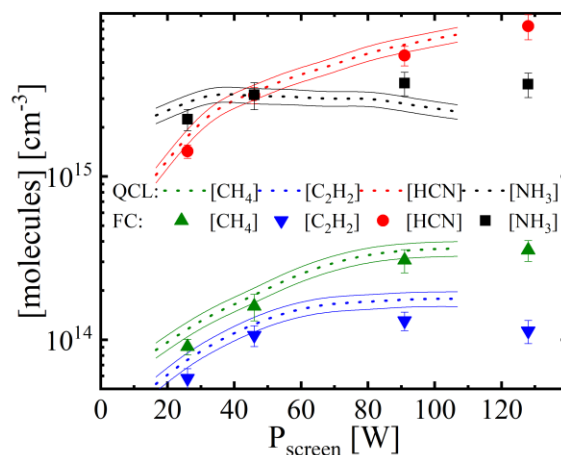


Figure 6.10 Concentrations of CH_4 , C_2H_2 , $\text{H}^{12}\text{C}^{14}\text{N}$, and NH_3 , as functions of the plasma power at the AS, determined with LAS using EC-QCL sources (dotted lines) and a FC source (solid points) [3]. Rotational temperatures are reported in figure 6.9 for both. Conditions: $\Phi_{\text{Total}} = 10 \text{ sccm H}_2 + 10 \text{ sccm N}_2$, $p = 3 \text{ mbar}$, CFC-AS in use.

6.5 Summary and conclusions

In the present study, a frequency comb between 2750 and 3450 cm^{-1} was used to investigate a laboratory-scale nitrocarburizing plasma in a $\text{H}_2:\text{N}_2$ gas flow at 3 mbar with a solid carbon source, previously studied using LAS with EC-QCL and TDLAS sources [3]. An average sampling point distance of 0.002085 cm^{-1} for the spectral range was achieved by interleaving of four spectra at different repetition rates, each an average of 50 single measurements. This way, 1028 transitions were fitted to Gaussian line profiles and identified. By plotting the natural logarithm of the weighted population of each transition of a vibrational band as a function of the transitions lower level energy, the Boltzmann plot method, rotational temperatures of the respective vibrational band were determined with a high level of precision. For the hot bands of HCN, the rotational temperatures were found to be $(442 \pm 7) \text{ K}$ and $(500 \pm 25) \text{ K}$ at a plasma power of 130 W. Further, the method failed to produce authentic temperature values for the ground state of HCN, as saturation effects limited the access to only transitions of a high lower level energy. However, the rotational temperatures of H^{13}CN and HC^{15}N were established as approximately 360 K at 130 W applied plasma power, thus in thermal equilibrium with the rotational temperatures of bands originating in the ground states of CH_4 , C_2H_2 , and NH_3 . Concerning the translational temperatures of each band, in all but one case they were found to be elevated compared to the corresponding values of rotational temperature, with typically a much-increased uncertainty. Comparing the rotational temperatures of ground state bands as determined with LAS using a FC source for applied plasma powers of 26, 46, 91, and 128 W with the rotational temperature of HCN reported in Puth *et al.* [3], a good agreement was found. Concerning the absolute concentrations as determined by both approaches, the concentrations of CH_4 , C_2H_2 , and HCN match, with slightly lower values determined from the comb spectra. However, a maximum in concentration of NH_3 at 40 W plasma power could not be confirmed, with a plausible explanation for the deviation in trend being the condition of the reactor between the two studies.

The large amount of information contained within the interrogated spectral range presents a unique challenge, as for this particular experiment hundreds of lines require manual fitting and proper

management of the acquired data. As the detected molecular species are common products of plasma chemistry involving nitrogen, hydrogen, and carbon at low pressure, similar experiments e.g. in the field of plasma-assisted diamond deposition, are expected to return spectra comparable in complexity to the present one. However, further progress in automation of spectral analysis is expected.

In comparison to established methods of temperature determination, as presented in chapters 4 and 5, the information on rotational temperatures is at least by a factor of 2 more precise and much more comprehensive. In turn, the assumption of a thermal equilibrium between rotational and translational temperatures can be checked, as well as the assumption of a thermal equilibrium between detected species. Both assumptions applied for the QCLAS and IRLAS study shown in chapter 5, are confirmed by the present study, which also serves as a proof-of-concept of comb spectroscopy applied to plasma processes.

References

- [1] Hamann S *et al.* 2015 *J. Phys. D: Appl. Phys.* **48** 34
- [2] Puth A *et al.* 2020 *Plasma Sources Sci. Technol.* **29** 035001
- [3] Puth A *et al.* 2018 *Plasma Sources Sci. Technol.* **27** 075017
- [4] Hamann S *et al.* 2015 *Rev. Sci. Instrum.* **86** 123503
- [5] Hamann S *et al.* 2017 *J. Appl. Phys.* **121** 153301
- [6] Ciddor P E 1996 *Appl. Opt.* **35** 1566
- [7] Mathar R J 2007 *J. Opt. A: Pure Appl. Opt.* **9** 470 – 476
- [8] Rutkowski L *et al.* 2018 *J. Quant. Spectrosc. Ra.* **204** 63 – 73
- [9] Gordon I *et al.* 2017 *J. Quant. Spectrosc. Radiat. Transfer* **96** 139
- [10] Abe M *et al.* 2013 *J. Opt. Soc. Am. B* **30**:4 1027 – 1035
- [11] Daumont L *et al.* 2013 *J. Quant. Spectrosc. Radiat. Transfer* **116** 101 – 109
- [12] Yang C *et al.* 2008 *J. Quant. Spectrosc. Radiat. Transfer* **109** 2857 – 2868
- [13] Maki A G *et al.* 2000 *J. Mol. Spectrosc.* **202** 67 – 82
- [14] Zimmermann H 2015 *Q-MACSoft – Ht v1.4.0*, neoplas control GmbH
- [15] Jørgensen U G 1990 *Astron. Astrophys.* **232** 420 – 430

7 Investigation of chemically similar plasma processes to PNC⁶

7.1 Introduction

The unique set of chemical and physical properties of diamond makes it an excellent candidate for mechanical, electrical, optical, thermal, and biomedical applications [1]. Recently, new types of microwave plasma-assisted chemical vapour deposition (MPACVD) reactors operating on a $\text{H}_2/\text{CH}_4/\text{CO}_2$ gas mixture at low pressure were designed to allow large-area nanocrystalline diamond (NCD) film synthesis at a low substrate temperature [2, 3]. Among these new technologies, a distributed antenna array (DAA) microwave system composed of a 4×4 source planar matrix was designed in order to achieve NCD films at a substrate temperature as low as $100\text{ }^\circ\text{C}$ on 4-inch wafers. Its efficiency for NCD growth on conventional (silicon) and unconventional substrates such as silicon nitride, $\text{AlN}/\text{ZnO}/\text{IDTs}/\text{LiNbO}_3$ multilayered structures and titanium implants has been demonstrated [4 – 6]. However, such a low temperature process is associated with a very low growth rate of only a few tens of nanometer per hour (nm h^{-1}) [7]. This hinders the synthesis of thick NCD films, which significantly reduces the potential of low temperature and large area NCD layers deposited at low temperature for industrial applications. It is worth to emphasize the fact that the low growth rate is still one of the main barriers for the industrial application of chemical vapour deposited (CVD) diamond [8].

To overcome this drawback, the addition of nitrogen in the feed gas can be considered. Indeed, in the last decades, it has been found that the addition of nitrogen permits to increase the growth rate and to improve the poly- and nanocrystalline diamond CVD processes in several ways: *i*) emergence of a $\langle 100 \rangle$ texture, *ii*) improvement of the film purity and *iii*) n-type doping of the film [9 – 14]. Recent studies have demonstrated a significant increase of the growth rate of NCD films synthesized at low temperature in $\text{H}_2/\text{CH}_4/\text{CO}_2/\text{N}_2$ feed gas, while maintaining a satisfactory purity [15].

In this paper, we focus on the study of the chemistry of $\text{H}_2/\text{CH}_4/\text{CO}_2/\text{N}_2$ -fed plasma ignited in a DAA reactor in order to gain further insights into the NCD deposition process. Results of investigations carried out over wide pressure and nitrogen flow ranges with *in-situ* optical emission spectroscopy (OES) in the visible and laser absorption spectroscopy (LAS) in the mid-infrared spectral range are presented. For the latter one, two different radiation sources were utilized. Firstly, tunable diode lasers (TDL) on lead-salt basis were used, integrated within the infrared multicomponent acquisition (IRMA) system [16]. Secondly, external-cavity quantum cascade lasers complemented the spectral range of IRMA [17 – 20] providing a mode-hop free tuning range of approximately 100 cm^{-1} [17, 21, 22].

The experiments on the microwave discharge have been conducted with the following aims:

- (i)* identification of nitrogen-containing species which are produced in the set gas mixture,
- (ii)* characterization of the gas temperature of the various species in the plasma, in particular nitrogen-containing species,
- (iii)* determination of the concentrations of measured species in dependence on process parameters,
- (iv)* discussion of chemical processes occurring in the gas phase and possible reactions at surfaces leading to the generation of molecules and of the role of nitrogen-containing species in the NCD growth process.

Using tunable diode laser absorption spectroscopy (TDLAS) the concentrations of CH_3 and CO were monitored and quantum cascade laser absorption spectroscopy (QCLAS) enabled the monitoring of the concentrations of the precursor, CH_4 , and of the reaction products, C_2H_2 , NH_3 , and HCN . Simultaneously, OES was used to obtain information about the temperature of H_2 in the active discharge

⁶ Authored by: Dekkar D, Puth A, Bisceglia E, Moreira P W P jr., Pipa A V, Lombardi G, Röpcke J, van Helden J H, and Bénédic F 2020, submitted to *J. Phys. D: Appl. Phys.*

zone and its degree of dissociation and, therefore, the concentrations of atomic and molecular hydrogen. The conversion rates of the feed gas species to the molecular reaction products were also determined. The results presented below are arranged in three parts: temperature measurements, densities obtained, and discussion about plasma chemistry and kinetics.

7.2 Experiment

7.2.1 Experimental arrangement

The experimental arrangement of the DAA CVD reactor for depositing NCD films is shown in figure 7.1 together with the optical diagnostics. The DAA reactor consists of 16 coaxial plasma sources arranged in a 4x4 matrix operated by a 6 kW microwave generator at 2.45 GHz. With the applied microwave power, localized discharges are sustained around each individual source. The discharges merge into a homogeneous plasma, which extends to the molybdenum substrate holder (with a diameter of 10 cm) located 15 cm below the microwave sources in the centre of the vessel to avoid the influence of the wafer surface on the measured concentrations. The reactor is connected to four gas lines, supplying methane, molecular hydrogen, carbon dioxide, and nitrogen. Further details of the design and operating principles of the reactor can be found elsewhere [23, 24].

The effects of nitrogen addition were studied for a pressure range of $p = 0.35$ to 0.55 mbar and a nitrogen fraction, replacing the H_2 feed gas, between 0 and 6 % of the total gas flow. The admixtures of CH_4 and CO_2 to the H_2 gas were chosen to be 2.6 % and 1 %, respectively. The total gas flow rate was $\Phi_{total} = 50$ sccm.

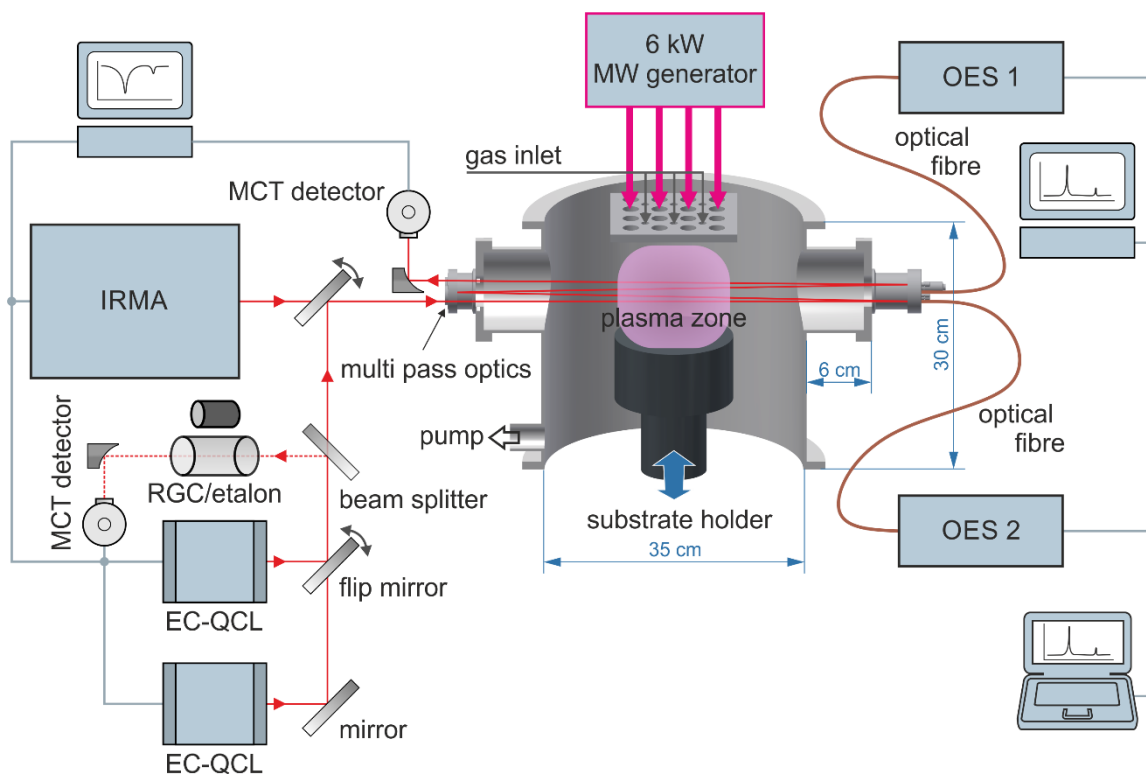


Figure 7.1 Experimental arrangement of the DAA microwave reactor combined with the LAS spectrometer, consisting of the IRMA system and two EC-QCLs, and the two OES spectrometers.

7.2.2 Optical arrangement

The OES and LAS measurements were performed simultaneously. The windows for optical investigations were situated about 10 cm below the microwave sources, which typically corresponds to the position of the substrate when growing diamond films, and thus allowed to observe the discharge volume above the substrate, as it is typical for a DAA reactor [25].

Two spectrometers were used for recording optical emission spectra. A compact Avantes Avaspec-2048L spectrometer was used to obtain overview spectra in the spectral range of $\lambda = 250 - 850$ nm. Complementary measurements were carried out using an Acton SpectraPro 2500i monochromator in combination with an Andor iStar DH734-18F-03 iCCD camera for identification of the spectra using a grating of 600 grooves mm^{-1} . Edge filters with cut-off wavelengths of 320 nm and 530 nm, respectively, were applied to separate the diffraction orders. Additionally, three spectral windows have been recorded at high-resolution with a grating of 2400 grooves mm^{-1} , namely the spectral ranges containing the H_α and H_β lines of the Balmer series and the (2-2) Q molecular hydrogen band of the Fulcher- α system. In those cases, calibrations were conducted using a tungsten band lamp.

The light was guided from the reactor to the spectrometers by optical fibres. The entrance aperture of each fibre was placed in the focal point of a quartz lens (25 mm diameter) to select a collimated emission from the reactor. Figure 7.2 depicts an example of an optical emission spectrum of the MW plasma with a $H_2/CH_4/CO_2/N_2$ feed gas mixture with identified spectral features of a variety of H_2 lines, the H_α , H_β , and H_γ lines of the Balmer series and nitrogen containing species, such as CN, NH, and N_2 . The inset shows five H_2 lines of the Fulcher- α (2-2) Q band recorded at high-resolution, which were used for the determination of the gas temperature and the degree of dissociation of hydrogen.

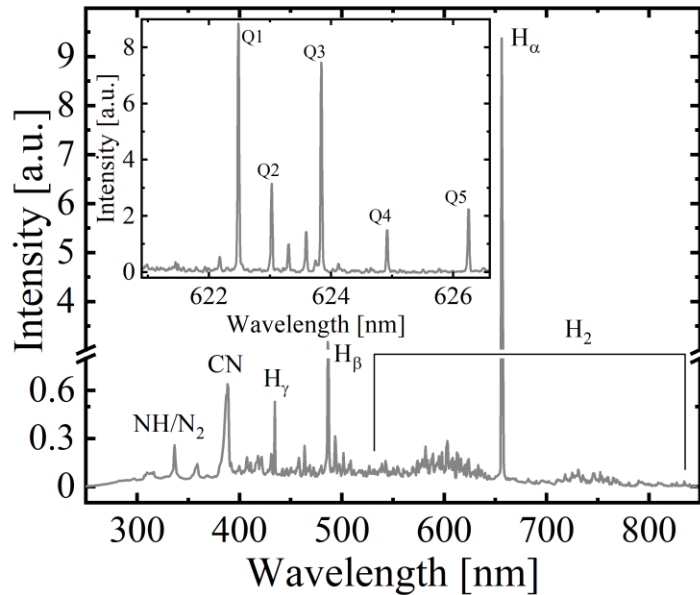


Figure 7.2 Optical emission spectrum with identified spectral features of the MW plasma in a $H_2-N_2-CH_4-CO_2$ gas mixture measured with the Avantes Avaspec-2048L spectrometer. Conditions: $p = 0.35$ mbar, $P = 3$ kW, $\Phi_{total} = 50$ sccm, N_2 admixture: 1 sccm, CH_4 admixture: 1.3 sccm, CO_2 admixture: 0.5 sccm. The inset shows a high-resolution spectrum, recorded with the Acton SpectraPro 2500i, of the spectral range between 621 and 627 nm with the five H_2 lines of the (2-2) Q transitions of the Fulcher- α band used for determining the gas temperature.

In addition to the OES setup, two different types of lasers were used for the LAS diagnostics. Firstly, two EC-QCLs (Daylight Solutions, MHF-21047-01 and MHF-41048) were combined on a single beam path, with a beam splitter providing a secondary channel for reference and etalon spectra for absolute spectral calibration. Secondly, the IRMA system had no such separate reference channel as it incorporates up to four TDLs with their required infrastructure and this has been presented in detail

elsewhere [16]. While the use of flipping mirrors could not be avoided to couple all diagnostics with the reactor, the *in-situ* spectra were recorded in series for the different laser sources.

The various laser beams are shaped using a focal mirror and enter the multipass cell (MPC) of the type White cell, which replaces the optical windows of the reactor, 10 cm below the microwave sources. The optical plane of the White cell is parallel to the substrate. With 20 passes an absorption length of 10.4 m is achieved. The plane of the White cell being parallel to the plasma sources provides a spatial resolution of the AS measurements lower than 1.2 cm in height and lower than 4 cm in width, defined by the mirror sizes. The probed volume, schematically shown in figure 7.1, diagonally crosses the reactor thus provides maximum possible absorption length in the plasma zone. After leaving the reactor, the beam is focused on a liquid-nitrogen cooled HgCdTe (MCT) infrared detector (EG&G JUDSON, bandwidth 1 MHz) by an off-axis parabolic.

In the absorption spectra, a fringing with an amplitude of up to 10 % of the total signal strength was observed and eliminated in post-processing of the data, see figure 7.3. In this figure, an example of a raw and post-processed EC-QCL absorption spectrum together with a Gaussian fit of the absorption features to determine the temperature is shown. The spectral positions of the molecular ground state and hot band transitions probed in the present study are given in table 7.1.

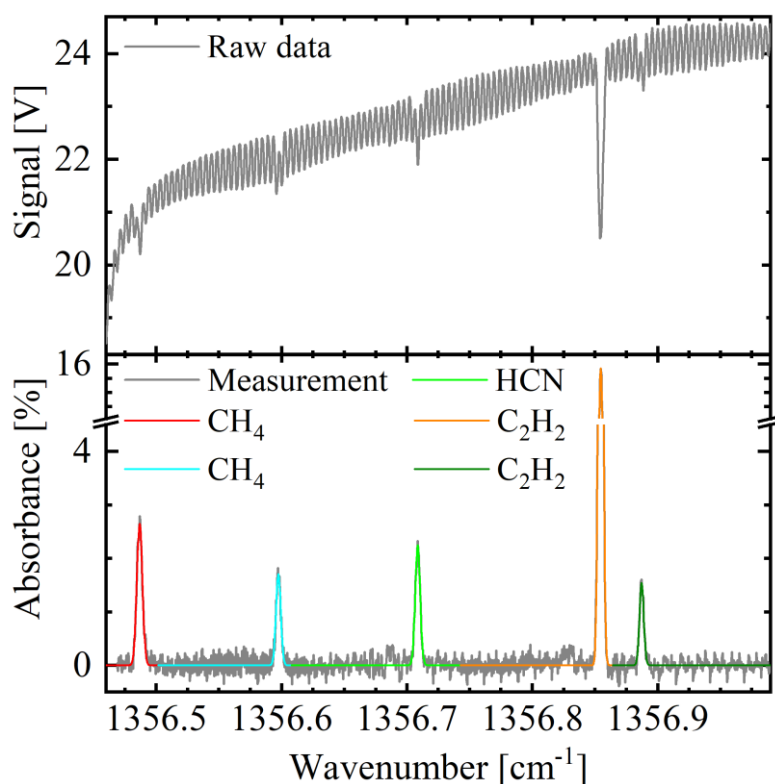


Figure 7.3 EC-QCL absorption spectrum of CH_4 , HCN , and C_2H_2 measured in a $\text{H}_2\text{-N}_2\text{-CH}_4\text{-CO}_2$ microwave plasma. Conditions: $p = 0.45$ mbar, $P = 3$ kW, $\Phi_{\text{total}} = 50$ sccm, N_2 admixture: 0.5 sccm, CH_4 admixture: 1.3 sccm, CO_2 admixture: 0.5 sccm. Upper part: raw transmission spectrum; lower part: post-processed absorbance spectrum with reduced fringe level and fitted line profiles.

Table 7.1 Species, spectral positions, linestrengths at room temperature, lower level energies, and quantum number assignments of the transitions used for determination of temperatures and concentrations. The superscript *Q* denotes use of an EC-QCL, *T* of a TDL.

Species	Spectral pos. [cm ⁻¹]	S ₀ [cm ² cm ⁻¹ mol. ⁻¹]	E'' [cm ⁻¹]	Vibr. quantum num. asgmt.	Rot. quantum num. asgmt.	Ref.
CH ₄ ^(Q)	1356.487	1.784·10 ⁻²⁰	470.805	0001 1F2 – 0000 1A1	10F2 2 – 9F1 2	[34]
	1356.597	1.190·10 ⁻²⁰	470.799	0001 1F2 – 0000 1A1	10E 1 – 9E 1	
C ₂ H ₂ ^(Q)	1356.855	1.301·10 ⁻¹⁹	155.289	000110 +u – 00000 +g	R 11 e	[35, 36]
	1356.888	8.920·10 ⁻²¹	766.808	000211 2u – 000101 g	R 11 e	
CH ₃ ^(T)	606.120	4.547·10 ⁻¹⁹	186.011	v2 ←ground	Q(3,3)	[37]
CO ^(T)	2150.856	1.826·10 ⁻¹⁹	3.845	1 – 0	R 1	[38]
NH ₃ ^(Q)	1388.055	2.726·10 ⁻²²	1541.87	0001 01 1E'' –	14 14 aE'A2'' –	[39]
				0000 00 0A2''	15 15 aA1''A2'	
HCN ^(Q)	1356.709	1.307·10 ⁻²¹	1115.818	0310 – 0110	P16f	[40, 41]
	1388.182	4.621·10 ⁻²⁰	106.417	0200 – 0000	P8	
H ₂ O ^(Q)	1387.934	3.054·10 ⁻²²	2004.815	020 – 010	432 – 321	[42]

7.3 Applied methods

7.3.1 Determination of atomic and molecular hydrogen densities via OES

The concentrations of atomic and molecular hydrogen were estimated from the degree of dissociation of hydrogen, measured by OES. The underlying method was developed by Lavrov and co-workers in 2006 [26, 27]. Therein, the relative intensities of the atomic (H_α, H_β) transitions and the molecular (2-2) Q1 hydrogen line are used, which are inferred in the framework of the so-called corona collisional-radiative model that includes electron impact excitation and spontaneous emission. As a simplification, the fine structure components of the atomic hydrogen lines are accounted for in two limiting cases:

Case 1: The excited hydrogen atoms are not perturbed by the medium during spontaneous emission.

Case 2: The population densities over the fine structure sublevels of the excited hydrogen atoms take the form of a Boltzmann distribution.

In the present work, the results obtained by both mutually exclusive cases agree within a factor of two. Thus, an averaged value between the two cases was used as an estimate and the margin of error increased accordingly.

As a result the method provides the density ratio of atomic and molecular hydrogen $[H]/[H_2]$ [26, 27]. The degree of dissociation D , defined as the ratio of dissociated molecules $[H_2]_{diss}$ to the total amount of hydrogen molecules $[H_2] + [H_2]_{diss}$, can be expressed as

$$D = \frac{[H_2]_{diss}}{[H_2] + [H_2]_{diss}} = \frac{[H]/[H_2]}{[H]/[H_2] + 2} \quad (7.1)$$

To determine the total amount of hydrogen molecules introduced to the reactor, one has to assume that the influence of the plasma chemistry on the hydrogen concentration can be neglected. Furthermore, by using the ideal gas law and the molar fraction of hydrogen in the feed gas x_{mol,H_2}^{total} , one can write:

$$[H_2] + [H_2]_{diss} = x_{mol,H_2}^{total} \cdot \frac{p}{k_B T_g} \quad (7.2)$$

where k_B is the Boltzmann constant, p is the pressure in the reactor, and T_g is the gas temperature. Substituting $[H_2] + [H_2]_{diss}$ in equation (7.1) by the expression (7.2), and taking into account that the density of the dissociated molecules is a half of the atomic density, $[H_2]_{diss} = [H]/2$, the atomic hydrogen densities can be expressed as:

$$[H] = 2 \cdot D \cdot x_{mol,H_2}^{total} \cdot \frac{p}{k_B T_g} \quad (7.3)$$

The product of the total molecular density and the fraction of the non-dissociated molecules gives the density of molecular hydrogen in the reactor:

$$[H_2] = (1 - D) \cdot x_{mol,H_2}^{total} \cdot \frac{p}{k_B T_g} \quad (7.4)$$

The gas temperature T_g , required for determination of $[H]/[H_2]$ as well as for equations (7.3, 7.4), was determined from the Fulcher- α (2-2) Q band, see inset in figure 7.2, by the method suggested in [28] and further developed in [29 – 31].

7.3.2 Laser absorption spectroscopy

The concentrations of the precursor gas CH_4 and of the reaction products CH_3 , CO , C_2H_2 , HCN , and NH_3 were determined by LAS using the Beer-Lambert law:

$$\int \ln \left(\frac{I_0(\nu)}{I_t(\nu)} \right) d\nu = n_i \cdot L \cdot S_i(T_{rot,i}) \quad (7.5)$$

where $I_0(\nu)$ and $I_t(\nu)$ are the wavenumber dependent laser intensities measured without and with absorbing media, n_i is the density of species i , L is the absorption length, $S_i(T_{rot,i})$ is the line strength of the selected absorption line of species i at the rotational temperature $T_{rot,i}$. Further information can be found in the HITRAN database [32]. For the plasma investigated here, an equilibrium between the translational and the rotational temperature was assumed [33]. The gas temperature was determined for every individual species from the Doppler broadening of the absorption lines. The contribution of the instrumental profile was estimated via the spectrum of a reference gas cell at room temperature. Figures 7.3 and 7.4 present examples of evaluated spectra for QCLAS.

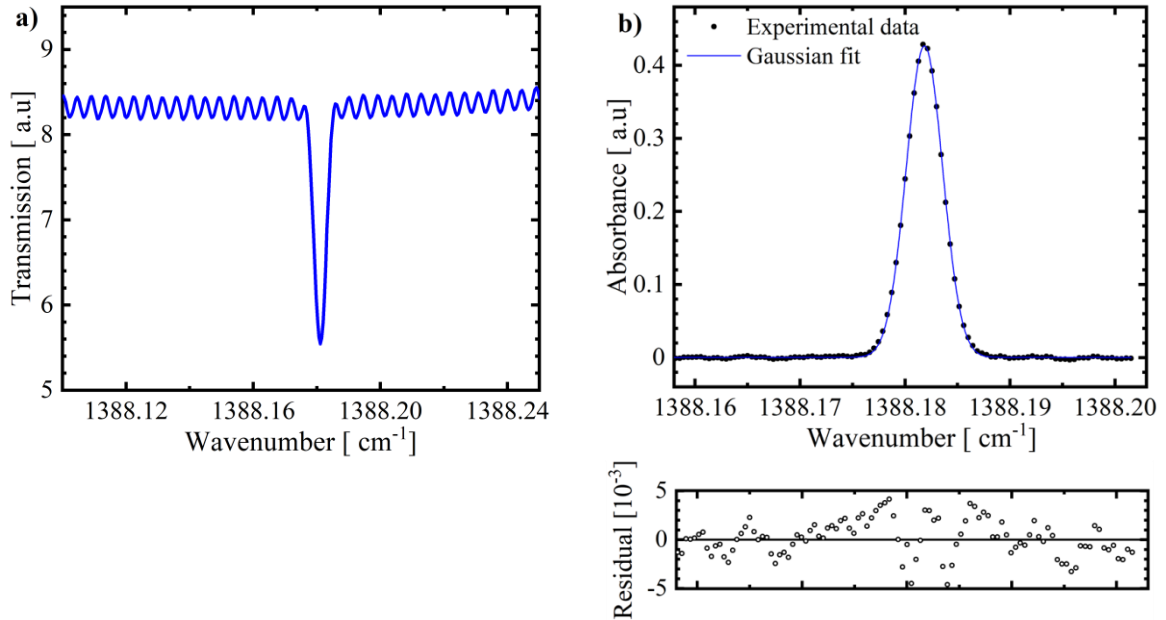


Figure 7.4 Example fit of an absorption line of HCN at 1388.182 cm^{-1} for the determination of the translational temperature and the absolute concentration in a $H_2-N_2-CH_4-CO_2$ microwave plasma. Conditions: $p = 0.45 \text{ mbar}$, $P = 3 \text{ kW}$, $\Phi_{total} = 50 \text{ sccm}$, N_2 admixture: 0.5 sccm , CH_4 admixture: 1.3 sccm , CO_2 admixture: 0.5 sccm . a) Raw absorption spectrum, b) fringe-reduced absorption spectrum with a Gaussian fit and its residual.

The conversion efficiency, R_C , of the feed gas species to product molecules in the plasma is expressed as:

$$R_C = n_{molecule} \Phi_{total} \frac{1}{60} \frac{10^3}{p} \frac{1}{P} \quad (7.6)$$

where R_C has units of molecules J^{-1} , $n_{molecule}$ is the measured molecular concentration in molecules cm^{-3} , Φ_{total} is the total gas flow rate in sccm, p is the pressure in mbar, and P is the power in W.

7.4 Results and discussion

7.4.1 Temperature measurements

For a comprehensive gas-phase characterization of the DAA CVD process, the gas temperature determination is crucial since the rates of the chemical reactions depend exponentially on the temperature. Additionally, the rotational temperature is required for the determination of the species densities from absorption spectroscopy due to the temperature dependence of the line strength. Here, we assume an equilibrium between the rotational and the gas temperature determined from the line profile analysis of the measured absorption spectra.

It should be noted that the applied diagnostics (LAS and OES) only return line-of-sight integrated values. However, there is a principle difference between the OES and LAS techniques. OES probes electronically excited species with very short lifetimes (especially excited hydrogen, both atomic and molecular), which exist only in the active discharge regions, where a sufficient amount of high energetic electrons are available for excitation to take place. Thus, OES provides information about the hottest regions along the line-of-sight. LAS probes the species in their ground electronic states. Chemically stable species, such as CH_4 and NH_3 , are present not only in the active discharge region but also in the gas volume between the discharge zone and the reactor walls. If the absorption length within the cold and hot regions are comparable, then the cold gas volumes contribute stronger to the measured absorption due to their large species densities in accordance to the ideal gas law. Moreover, stable species can be decomposed efficiently in the discharge region. Chemically active (CH_3) or vibrationally excited (H_2O ($v=1$)) species are created in the active discharge zone and can diffuse into the cold gas regions, but their short lifetime will limit their statistical distance of travel outside the active discharge zone. Therefore, every measured species has its own gas temperature in dependence on the species lifetime and chemical reactivity, as it was inferred in previous investigations of DAA reactor [33].

Figure 7.5 presents the gas temperatures as a function of N_2 admixture as determined from the Doppler broadening of the HCN and NH_3 lines originating from the ground electronic state and the gas temperature of H_2 determined from the rotational structure of excited electronic state of H_2 . The obtained gas temperatures are independent of the admixed nitrogen flow. In case of NH_3 , concentrations could be determined for a nitrogen flow above 0.7 % but the signal-to-noise ratio for a nitrogen flow below 2 % did not allow to derive translational temperatures for NH_3 .

No noticeable trend in temperature as a function of admixed nitrogen was found for all the species investigated and average values are presented in figure 7.6. The stable species C_2H_2 , CH_4 , and HCN had the lowest gas temperature at about 400 K. Chemically active CH_3 and vibrationally excited C_2H_2 , HCN, and H_2O molecules indicated as hot band (HB) in figure 7.6, showed elevated gas temperatures in the range of 400 to 700 K. The highest value for the gas temperature of about 900 K was found for electronically excited H_2 , corresponding to the hottest regions of the plasma bulk from where the emissions of the hydrogen Fulcher- α band are originating. The gas temperatures for the various species determined here in presence of nitrogen are consistent with the gas temperatures determined by Nave *et al.* for H_2 - CH_4 - CO_2 plasmas in the similar experimental conditions [33].

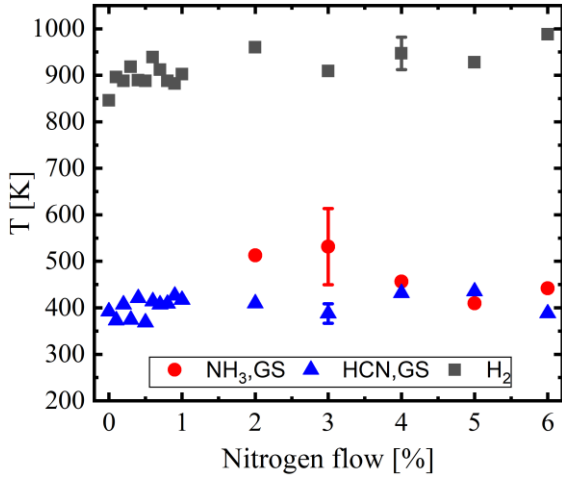


Figure 7.5 Dependence of the gas temperature of the ground state NH_3 , HCN , and H_2 on the N_2 admixture. Conditions: $p = 0.35$ mbar, $P = 3$ kW, $\Phi_{\text{total}} = 50$ sccm, CH_4 admixture: 1.3 sccm, CO_2 admixture: 0.5 sccm.

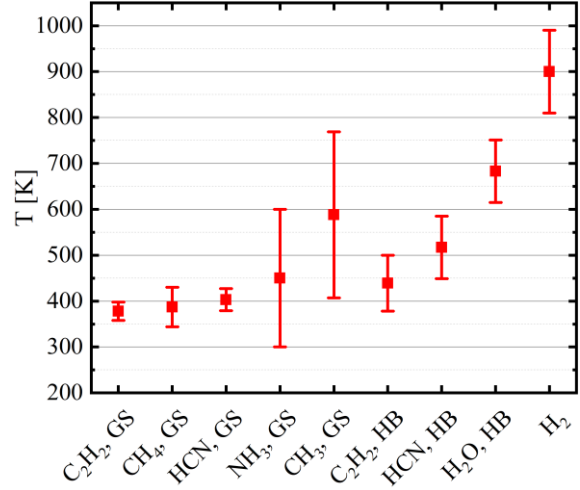


Figure 7.6 Gas temperatures of the studied species; ground state (GS) and hot band (HB). Conditions: $p = 0.35$ mbar, $P = 3$ kW, $\Phi_{\text{total}} = 50$ sccm, CH_4 admixture: 1.3 sccm, CO_2 admixture: 0.5 sccm.

7.4.2 Species densities

7.4.2.1 Gas phase composition in dependence on the nitrogen flow

Figure 7.7 gives an overview of the concentrations for eight different atomic and molecular species, the precursors H_2 and CH_4 , and the products H , CH_3 , C_2H_2 , CO , HCN , and NH_3 , in dependence on the nitrogen flow at $p = 0.35$ mbar, $P = 3$ kW, and $\Phi_{\text{total}} = 50$ sccm. The concentrations of the species differ significantly and range over four orders of magnitude from $6 \cdot 10^{11}$ to $3 \cdot 10^{15}$ molecules cm^{-3} . The highest concentration is found for H_2 ($3 \cdot 10^{15}$ molecules cm^{-3}), which is the dominant fraction of the feed gas. The degree of dissociation of hydrogen is between 7 and 13 %, thus atomic hydrogen is the second most abundant species in the active discharge region with densities of about $(5 \pm 3) \cdot 10^{14}$ molecules cm^{-3} . This value is comparable with values obtained by Nave *et al.* ($2 \cdot 10^{14}$ cm^{-3}) for a $\text{H}_2/\text{CH}_4/\text{CO}_2$ plasma [43].

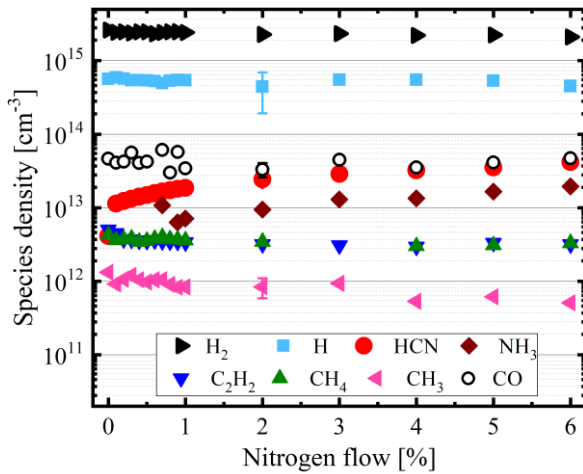


Figure 7.7 Species densities as a function of N_2 admixture. Conditions: $p = 0.35$ mbar, $P = 3$ kW, $\Phi_{\text{total}} = 50$ sccm, CH_4 admixture: 1.3 sccm, CO_2 admixture: 0.5 sccm.

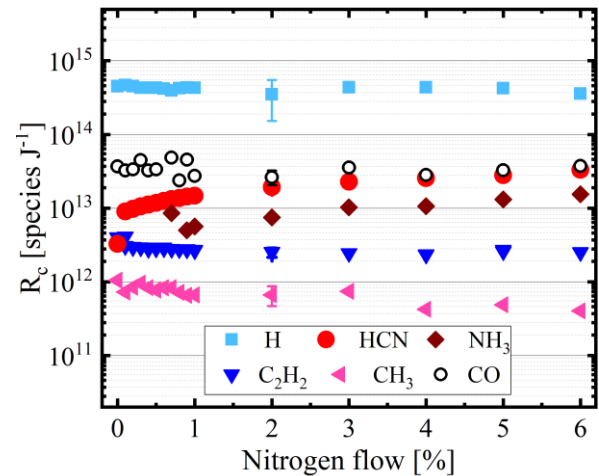


Figure 7.8 Conversion efficiency of the precursor molecules to reaction products as a function of N_2 admixture. Conditions: $p = 0.35$ mbar, $P = 3$ kW, $\Phi_{\text{total}} = 50$ sccm, CH_4 admixture: 1.3 sccm, CO_2 admixture: 0.5 sccm.

With the nitrogen flow increasing from 0 to 6%, the concentrations of NH₃ and HCN gradually increased from $0.5 \cdot 10^{13}$ to $1.5 \cdot 10^{13}$ molecules cm⁻³ and from $1 \cdot 10^{13}$ to $4 \cdot 10^{13}$ molecules cm⁻³, respectively. In contrast, the densities of CO and the other hydrocarbon products remained constant: around $3 \cdot 10^{13}$ molecules cm⁻³ for CO, around $5 \cdot 10^{12}$ molecules cm⁻³ for C₂H₂ and CH₄ and around $8 \cdot 10^{11}$ molecules cm⁻³ for CH₃. It should be emphasized, that the concentrations of the nitrogen-containing products NH₃ and HCN are higher than the concentrations of CH₄, CH₃, and C₂H₂. Moreover, the conversion of CH₄ is very efficient since the concentration injected in the feed gas is $1.65 \cdot 10^{14}$ molecules cm⁻³, which means that 97 % of the CH₄ has been dissociated.

Figure 7.8 shows the conversion efficiencies of the precursor molecules into H, CH₄, CH₃, C₂H₂, CO, HCN, and NH₃ in the H₂/CH₄/CO₂/N₂ MW plasma depending on the nitrogen flow. They range between $5 \cdot 10^{11}$ and $2 \cdot 10^{15}$ molecules J⁻¹. The conversion efficiency of H is one order of magnitude higher than that of HCN and NH₃.

7.4.2.2 Detailed view on species concentrations in dependence on pressure and flow

In this part, the effects of the nitrogen flow and the gas pressure on the concentrations of the measured species are represented in order to show the variation of the concentrations of precursor molecules as well as the reaction products in detail. All the results for the concentrations of species are given for a standard condition (SC) defined as follows: a microwave power of 3 kW, a total flow rate of 50 sccm and a fixed gas flow for CH₄ at 1.3 sccm and for CO₂ at 0.5 sccm. In this section, three values of the total pressure are considered: 0.35, 0.45, and 0.55 mbar.

Figure 7.9 shows the molecular hydrogen concentrations. The concentration increases with pressure in accordance with the ideal gas law. A minimal gradual decrease of the concentrations as a function of nitrogen flow related to the dilution of the input gas flow by nitrogen can be observed. However, the concentration of atomic hydrogen is independent on the gas pressure, see figure 7.10, and remains in the range of 0.4 to $0.8 \cdot 10^{14}$ molecules cm⁻³, whereas due to the large errors in the obtained data no clear trend can be observed as a function of the nitrogen flow.

The concentrations of NH₃ and HCN are shown for the three pressures as a function of the nitrogen flow rate in the survey figures 7.11 and 7.12, respectively. Generally, the NH₃ and HCN concentrations increase significantly by almost an order of magnitude with nitrogen admixture and pressure. The concentrations range from $0.5 \cdot 10^{13}$ to $7 \cdot 10^{13}$ molecules cm⁻³ for HCN and from $0.5 \cdot 10^{13}$ to $4.5 \cdot 10^{13}$ molecules cm⁻³ for NH₃. We note that for 0 % admixture of N₂ a small quantity of HCN is observed. This indicates that HCN is produced already without addition of nitrogen, most probably due to residual nitrogen gas from small leaks in the reactor. As mentioned before, concentrations of NH₃ could only be determined for a nitrogen flow above 0.7 %, which means that the density of NH₃ is below the detection limit of $5 \cdot 10^{13}$ molecules cm⁻³.

It is of particular interest, that nitrogen-containing species are considerably more abundant than hydrocarbons, such as C₂H₂, CH₃, and CH₄. A more detailed discussion on the nitrogen and carbon mass balance will be given in section 4.2.3.

The concentration of CH₄ decays slightly with increasing N₂ flow for the highest pressure of 0.55 mbar and shows no clear trend for the other two pressures. Furthermore, the concentration increases with pressure, similarly to the H₂ concentration, as seen in figure 7.13. The CH₃ concentration (figure 7.14) is independent on pressure, similar to the concentration of hydrogen atoms generated in the active discharge region, and decreases with nitrogen flow. The additional loss of CH₃ can be attributed to the formation of HCN and the subsequent decrease of available carbon in the reactor. The CH₃ concentration ranges from $0.8 \cdot 10^{12}$ to $2.0 \cdot 10^{12}$ molecules cm⁻³. The C₂H₂ concentration (figure 7.15) also decreases with nitrogen flow similar to the concentration of CH₃, however as a stable species it accumulates in the

cold parts of the reactor. Accordingly, its concentration is proportional to the total number of particles, i.e. the pressure, and ranges from $3 \cdot 10^{12}$ to $1 \cdot 10^{13}$ molecules cm^{-3} .

Regarding the concentrations of CO, the rotational temperature required to calculate the concentrations could not be determined in this work due to a larger laser linewidth than usual. Therefore, we used the rotational temperature of 380 K, which was previously determined in an extensive study of the gas and rotational temperature of CO in this reactor by Nave *et al.* [33]. There is no dependence of the concentration of CO on the nitrogen flow within the error of the obtained densities (figure 7.16), while it increased from $3.1 \cdot 10^{13}$ to $5.9 \cdot 10^{13}$ molecules cm^{-3} with rising pressure. The concentration of CO is found to be of the same order of magnitude as the concentrations of HCN and NH_3 .

To summarize, the densities of all stable species (CO, H_2 , CH_4 , C_2H_2 , HCN, and NH_3), which can be accumulated in the cold regions of the reactor, increase with pressure in accordance to the ideal gas law. Short living species (H and CH_3) densities are independent on pressure. An increase of the nitrogen containing species density with nitrogen flow is accompanied by a decrease of hydrocarbon molecules concentrations. It is also noteworthy that in this study the concentrations of the species probed at 0 % of nitrogen are similar to values reported in previous studies [43].

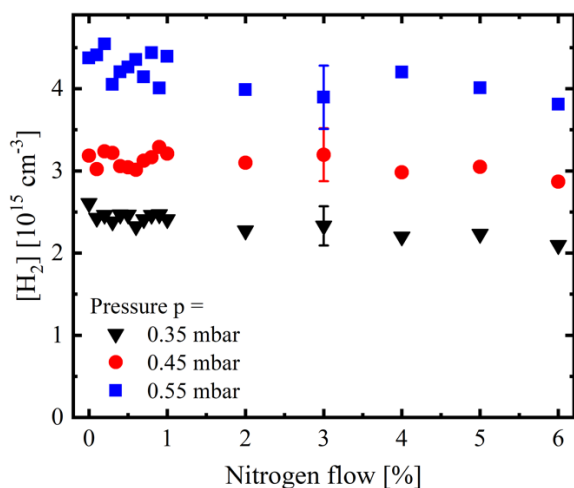


Figure 7.9 Molecular hydrogen concentration at 3 pressures as functions of N_2 admixture at SC.

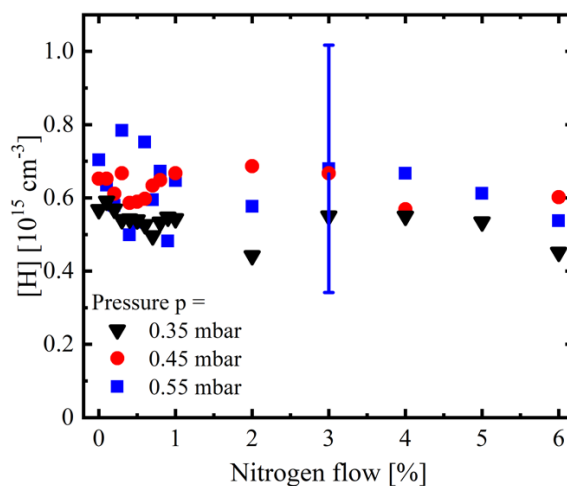


Figure 7.10 Atomic hydrogen concentration at 3 pressures as functions of N_2 admixture at SC.

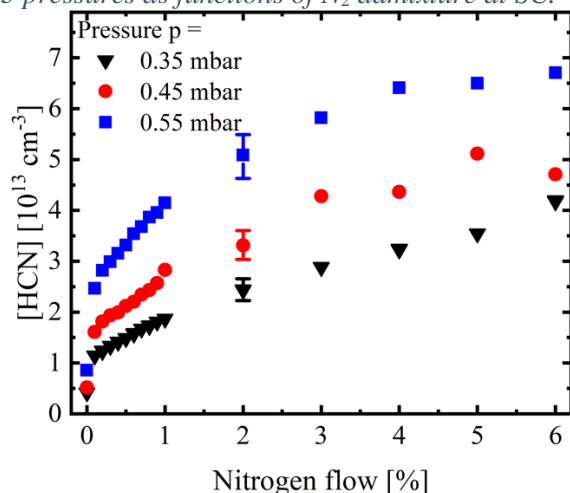


Figure 7.11 Hydrogen cyanide concentration at 3 pressures as functions of N_2 admixture at SC.

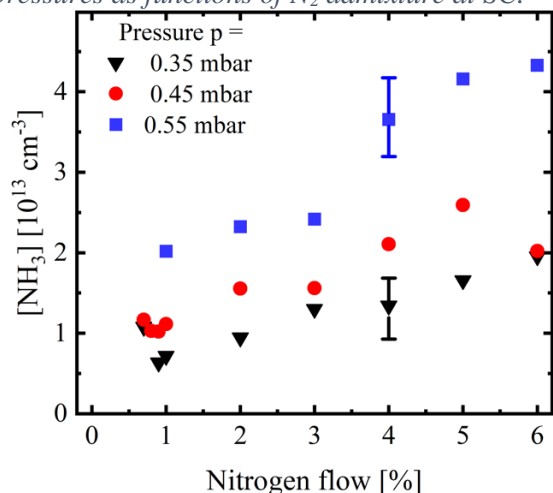


Figure 7.12 Ammonia concentration at 3 pressures as functions of N_2 admixture at SC.

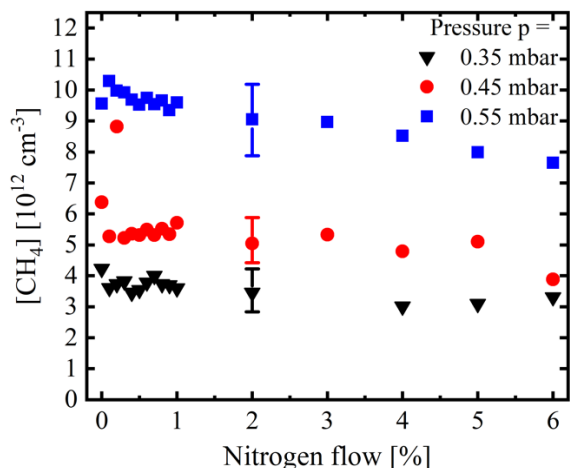


Figure 7.13 Methane concentration at 3 pressures as functions of N_2 admixture at SC.

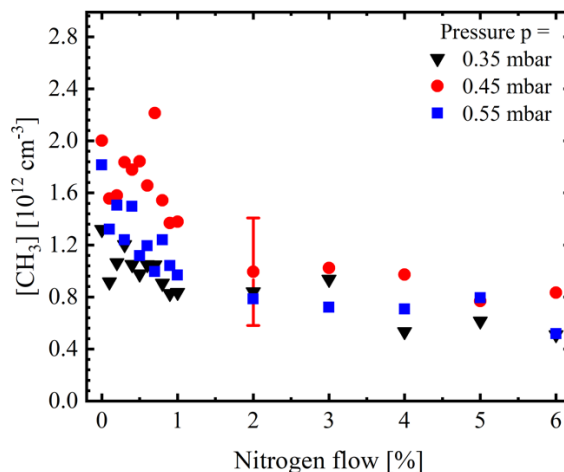


Figure 7.14 Methyl concentration at 3 pressures as functions of N_2 admixture at SC.

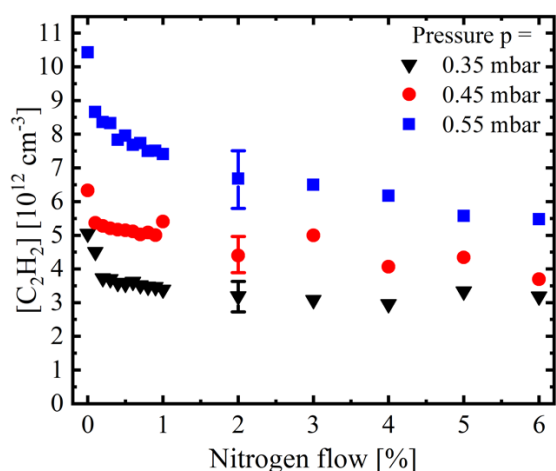


Figure 7.15 Acetylene concentration at 3 pressures as functions of N_2 admixture at SC.

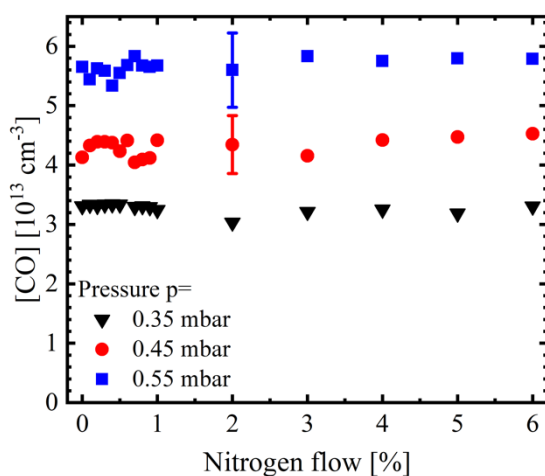


Figure 7.16 Carbon monoxide concentration at 3 pressures as functions of N_2 admixture at SC.

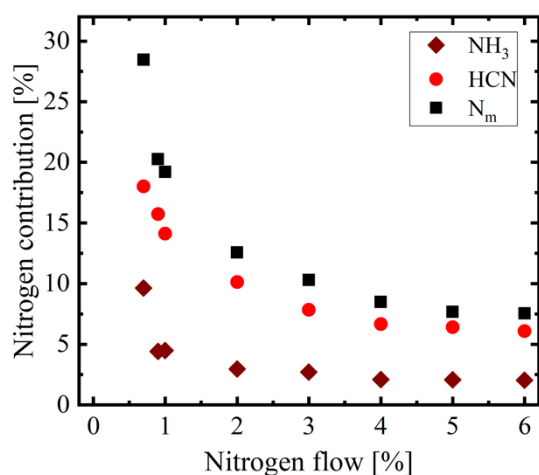


Figure 7.17 Nitrogen mass balance in dependence on the N_2 admixture at $p = 0.35 \text{ mbar}$ and SC.

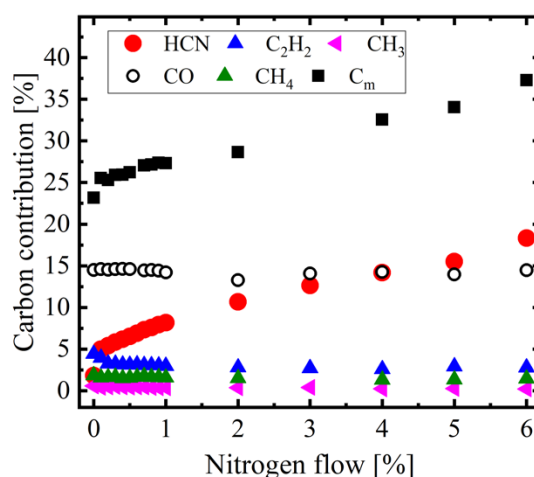


Figure 7.18 Carbon mass balance in dependence on the N_2 admixture at $p = 0.35 \text{ mbar}$ and SC.

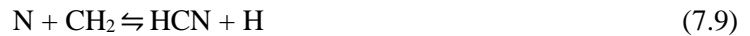
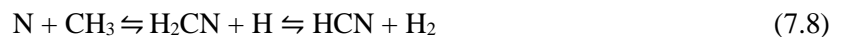
7.4.2.3 Nitrogen and carbon mass balance

The nitrogen and carbon mass balances of the plasma chemical processes as a function of the nitrogen flow are shown in figure 7.17 and 7.18, respectively. The upper curves (N_m and C_m) represent the sum of all nitrogen (figure 7.17) and carbon (figure 7.18) masses of the probed species normalized on the total nitrogen and carbon masses introduced into reactor, respectively. The nitrogen mass balance decreases from 28 to 7 % with the increasing nitrogen flow. The main contribution comes from HCN, with a variation from 18 to 5 %, while the contribution of NH_3 is much less important in the range 2 – 10 %. A nitrogen mass balance significantly lower than 100 % as estimated here is attributable to the assumption of other nitrogen-containing species being present in the plasma, but not being monitored by LAS. Especially N_2 molecules, which are in the feed gas and were not dissociated in the discharge. Additionally CN, NH, NH_2 , N_2^+ could contribute to the mass balance. OES indicates the presence of electronically excited N_2 , NH, and CN as shown in figure 7.2 but the used spectral ranges do not allow the determination of the species densities. It can be seen in figure 7.18, that in the carbon case, the contributions of potential sources of carbon (CO, CH_4 , CH_3 , and C_2H_2) show no noticeable trend as function of nitrogen flow, whereas HCN contribution increases from 5 to 17 %. Therefore, this indicates that the carbon involved in the formation of this significant amount of HCN has to come not only from the hydrocarbons species but also from walls, which act as sinks for carbon atoms. Between 5 % and 17 % of the available carbon in the gas phase appears as HCN and CO. The contributions of CH_4 , CH_3 , and C_2H_2 are less pronounced. It should be underlined that the deposition observed on the reactor walls could also affect the nitrogen and carbon mass balance since the reactor walls could act as sinks for nitrogen and carbon as previously discussed for carbon and oxygen [43].

7.5 Plasma chemistry and kinetics

A deep understanding of the plasma kinetics is required in order to understand the species behavior described in this article and to improve the NCD deposition process, in particular, in terms of the growth rate and the microstructure, at low temperature and on a large area in the DAA reactor, in the presence of nitrogen. Some aspects of plasma chemistry and kinetics are thus briefly discussed in the following.

According to figure 7.7, HCN is among the major products detected in the plasma with a concentration of about 10^{13} molecules cm^{-3} . This result is in a good agreement with literature in which HCN has been identified as one of the most abundant stable species in low pressure methane- and nitrogen-containing microwave discharges [44]. It is created mainly according to the following reactions [45, 46]:

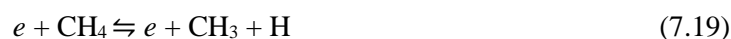


It can be seen that a majority of these reactions producing HCN involve CH_x as reactant, in particular, CH₃, which explains the decrease of the CH₃ density with increasing nitrogen flow (figure 7.14). Thus, the more nitrogen is admixed, the more HCN and the less CH_x is produced.

The decreasing trend of the concentrations of CH₄ and C₂H₂ as a function of nitrogen flow (figures 7.13 and 7.15) can be also considered to be related to the HCN formation. Indeed, the production of C₂H₂ requires CH₃ as a reactant through the following consecutive reaction scheme [47 – 49]:



CH₃ is in turn a product of the dissociation of CH₄ through reactions (7.19) and (7.20):



Thus, if CH₃ is likely to be engaged in reactions leading to HCN formation, the reaction balances (7.14) to (7.20) will shift accordingly, thus the concentrations of C₂H₂ and CH₄ are expected to decrease.

As NH₃ is the second major nitrogen-containing compound detected by LAS with a concentration of about 3·10¹³ molecules cm⁻³ depending on plasma conditions, the following reactions may be involved [50 – 52]:



The formation of NH₃ from these mechanisms is therefore supposed to consume H₂ and to produce H-atoms.

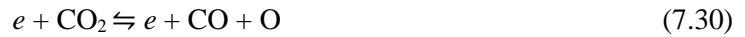
At low process pressure, NH₃ is mainly produced at the surface of the vessel pressure by the stepwise addition reactions between adsorbed nitrogen N (s) and hydrogen H (s) containing radicals at the surface and incoming atomic N and H radicals [53]:





However, the densities measured for H₂ and H are approximately two orders of magnitude higher than those of detected nitrogen-containing species, so that the production of NH₃ does not strongly and directly affects the concentrations (figures 7.9 and 7.10).

CO is the predominant oxygen-containing species in the plasma and its concentrations are found to be of the same order of magnitude as HCN and NH₃ concentrations, i.e. 3·10¹³ to 6·10¹³ molecules cm⁻³ depending on plasma conditions (figure 7.16). It is created from CO₂ according to the following reaction:



Carbon monoxide is in turn decomposed into carbon and atomic oxygen at high values of the electron density and temperature [54], as follows:



The plasma produces N atoms mainly through electron-impact dissociation of N₂ as described by equation (7.32). As reported in the literature [55], the N₂ dissociation requires an energy of 9.76 eV. The electron temperature of a few eV estimated in the DAA reactor close to the sources [56] provides a considerable population of high energy electrons situated in the tail of the electron energy distribution function thereby ensuring this N₂ dissociation:



Oxygen atoms may be formed not only by dissociation of CO₂ and CO (reactions (7.30) and (7.31)) but also by titration reaction of nitrogen atoms as follows [57]:



We note that the production of oxygen is very important in the diamond deposition process due to its essential role as an etching product of non-diamond phases [58] and abstraction of hydrogen atoms from surfaces [59].

To summarize, nitrogen addition leads to an increase in the concentration of nitrogen-containing molecules in the plasma (HCN, CN). In the conventional MPACVD growth process (high surface temperature, H₂/CH₄ gas mixture) these molecules are supposed to be responsible for the profitable growth of the sp² bonded carbon phase in the diamond film which generally leads to low purity of the films [60, 11, 13]. However, in the case of the DAA reactor working with a H₂/CH₄/CO₂ basic gas mixture, the addition of nitrogen could result in an appreciable amount of atomic oxygen, which is responsible of sp² phases etching, through reaction (7.33). Therefore, satisfactory film purity can be maintained while increasing the growth rate [61].

7.6 Conclusions

Employing infrared laser absorption spectroscopy combined with optical emission spectroscopy, the effects of adding nitrogen to a H₂/CH₄/CO₂ plasma used for low-temperature and large-area deposition of nanocrystalline diamond films on plasma chemistry was examined. As the positive influence of nitrogen on the formation of diamond films is evident, it is desirable to clarify whether this is due to modifications of the plasma reactivity. In addition to carbon-containing species (CH₃, CH₄, C₂H₂, and CO) usually probed by LAS in a H₂/CH₄/CO₂ plasma, nitrogen-containing species such as HCN and NH₃ have been identified and monitored. Using lead-salt tunable diode lasers and external-cavity quantum cascade lasers, translational temperatures of the various species were measured and thus have been used to derive the concentrations of various stable and unstable plasma species, which were found to be in a range between 10¹¹ and 10¹⁵ molecules cm⁻³. The species temperatures are not significantly affected by the nitrogen addition. The formation of HCN seems to be the dominant chemical reaction occurring in the plasma since HCN was found to be among the major products in the plasma besides molecular and atomic hydrogen. The influence of the pressure and nitrogen flow on the molecular concentrations has been studied and discussed. The analysis of the nitrogen and carbon mass balances of measured species indicates that other nitrogen- and carbon-containing species are produced in the plasma such as NH, H₂CN, C₂N₂, CN, and H₂CO though no direct measurement of them was undertaken. It was also shown that the formation of HCN reduces the amount of available C atoms, leading to a decrease of the densities of hydrocarbon species, whereas the presence of nitrogen in the feed gas may help in the production of oxygen-containing etching species favorable to the synthesis of good purity diamond films.

Further works will deal with the correlation of the plasma behavior with the nitrogen amount incorporated in diamond lattice and its influence on NCD films characteristics, in particular on the microstructure.

References

- [1] Williams O A 2011 *Diam. Relat. Mater.* **20** 621
- [2] Kromka A *et al.* 2012 *Vacuum* **86** 776
- [3] Tsugawa K *et al.* 2006 *New Diamond Front. Carbon Technol.* **16** 337
- [4] Baudrillart B *et al.* 2016 *Phys. Status Solidi A* **213** 2575
- [5] Dekkar D *et al.* 2019 *Diam. Relat. Mater.* **94** 28
- [6] Dekkar D *et al.* 2018 *Phys. Status Solidi A* **215** 1800251
- [7] Baudrillart B *et al.* 2017 *Diam. Relat. Mater.* **75** 44
- [8] May P 2008 *Science* **319** 1490
- [9] Tang C J *et al.* 2011 *Diam. Relat. Mater.* **20** 304
- [10] Tang C J *et al.* 2015 *Vacuum* **122** 342
- [11] Chatei H *et al.* 1997 *Diam. Relat. Mater.* **6** 107
- [12] Achard J *et al.* 2007 *Diam. Relat. Mater.* **16** 685
- [13] Vandeveld T *et al.* 1997 *Thin Solid Films* **154** 308
- [14] Corrigan T D *et al.* 2002 *Diam. Relat. Mater.* **11** 43
- [15] Bénédic F *et al.* 30th *International Conference on Diamond and Carbon Materials*, 8-12, September 2019, Seville, Spain
- [16] Röpcke J *et al.* 2000 *Rev. Sci. Instrum.* **71** 3706
- [17] Lopatik D *et al.* 2012 *Meas. Sci. Technol.* **23** 115501
- [18] Lopatik D *et al.* 2012 *Contrib. Plasma Phys.* **52** 864
- [19] Röpcke J *et al.* 2012 *J. Phys. D: Appl. Phys.* **45** 423001
- [20] Hamann S *et al.* 2015 *Rev. Sci. Instrum.* **86** 123503
- [21] Röpcke J *et al.* 2016 *Photonics* **3** 45
- [22] Curl R F *et al.* 2010 *Chem. Phys. Lett.* **487** 18
- [23] Baudrillart B *et al.* 2015 *Phys. Status Solidi A* **212** 2611
- [24] Mehedi H A *et al.* 2014 *Diam. Relat. Mater.* **47** 58
- [25] Latrasse L *et al.* 2007 *Plasma Sources Sci. Technol.* **16** 7
- [26] Lavrov B P, Pipa A V, and Röpcke J 2006 *Plasma Sources Sci. Technol.* **15** 135
- [27] Lavrov B P *et al.* 2006 *Plasma Sources Sci. Technol.* **15** 147
- [28] Lavrov B P and Otorbaev D K 1978 *Pisma v Zhurnal Tekhnicheskoi Fiziki* **4** 1419
- [29] Drachev A I and Lavrov B P 1988 *High Temp.* **26** 129
- [30] Lavrov B P and Tyutchev M V 1984 *Acta Phys. Hung.* **55** 411
- [31] Astashkevich S A *et al.* 1996 *J. Quant. Spectrosc. Radiat. Transfer* **56** 725

- [32] Rothman L S *et al.* 2005 *J. Quant. Spectrosc. Radiat. Transfer* **96** 139
- [33] Nave A S C *et al.* 2016 *Plasma Sources Sci. Technol.* **25** 065002
- [34] Ba Y A *et al.* 2013 *J. Quant. Spectrosc. Radiat. Transfer* **130** 62
- [35] Gomez L *et al.* Y 2009 *J. Quant. Spectrosc. Radiat. Transfer* **110** 2102
- [36] Kabbadj Y and Herman M 1991 *J. Mol. Spectrosc.* **150** 535
- [37] Stancu G D, Röpcke J, and Davies P B 2005 *J. Phys. Chem.* **122** 14306
- [38] Li G *et al.* 2015 *Astrophys. J. Suppl. Ser.* **216** 15
- [39] Cottaz C *et al.* 2000 *J. Mol. Spectrosc.* **203** 285
- [40] Maki A, Quapp W, and Klee S 1995 *J. Mol. Spectrosc.* **171** 420
- [41] Malathy D V *et al.* 2003 *J. Quant. Spectrosc. Radiat. Transfer* **82** 319
- [42] R.A.Toth, "Linelist of water vapor parameters from 500 to 8000 cm⁻¹", database.
- [43] Nave A S C *et al.* 2016 *Plasma Sources Sci. Technol.* **25** 065003
- [44] Truscott B S *et al.* 2015 *J. Phys. Chem. A* **119** 12962
- [45] Pintassilgo C D *et al.* 1999 *Plasma Sources Sci. Technol.* **8** 463
- [46] Leeds S M *et al.* 1999 *Diam. Relat. Mater.* **8** 226
- [47] Alman D A, Ruzic D N, and Brooks J N 2000 *Phys. Plasmas* **7** 1421
- [48] Heintze M, Magureanu M, and Kettlitz M 2002 *J. Appl. Phys.* **92** 7022
- [49] Nakano T, Toyoda H, and Sugai H 1991 *Jpn. J. Appl. Phys.* **30** 2912
- [50] Oumghar A *et al.* 1994 *Plasma Chem. Plasma Process.* **14** 229
- [51] Mertens J D *et al.* 1989 *Int. J. Chem. Kinet.* **21** 1049
- [52] Cohen N 1987 *Int. J. Chem. Kinet.* **19** 319
- [53] Gordiets B *et al.* 1998 *Plasma Sources Sci. Technol.* **7** 379
- [54] Latrasse L *et al.* 2007 *J. Phys. D: Appl. Phys.* **40** 5177
- [55] Frost D C and McDowell C A 1956 *Proc. R. Soc. Lond. A* **236** 278
- [56] Bénédic F, Baudrillart B, and Achard J 2018 *Eur. Phys. J. Appl. Phys.* **81** 10804
- [57] Hong T S *et al.* 1995 *Appl. Phys. Lett.* **67** 2149
- [58] Harris S J and Weiner A M 1989 *Mat. Res. Soc. Symp. Proc.* **162** 163
- [59] Ihara M *et al.* 1992 *Diam. Relat. Mater.* **1** 187
- [60] Bénédic F *et al.* 2003 *Surf. Coat. Technol.* **176** 37
- [61] Bénédic F *et al.* 2020, Submitted to *Diam. Relat. Mater.*

8 Summary, conclusions, and outlook

A series of laser absorption spectroscopic measurements, using lead-salt tuneable diode lasers, external-cavity quantum cascade lasers, and a frequency comb source, have been conducted at an industrial- and a laboratory-scale plasma nitrocarburizing reactor, both equipped with active screens made of carbon-fibre reinforced carbon. This way, the concentrations of CH₄, C₂H₂, CO, HCN, and NH₃ determined for the industrial-scale reactor as functions of the pressure and the total gas flow. HCN and NH₃ were found to be the predominant reaction products within a plasma-chemical environment, composed of at most 50 % reaction products. Furthermore, it was shown that changes to the feed gas composition, in turn producing different concentrations of reaction products, result in structural modifications in the nitrocarburized layers.

In addition, one study established at the laboratory-scale the carbon mass flow, which was subsequently applied to the industrial-scale to gain insight on the carbon consumption at the active screen. A good agreement in the carbon consumption efficiency was reported for the systems at both scales. Further, it was found, that the addition of oxygen-containing admixtures, e.g. O₂ or CO₂, increased the carbon mass flow, while simultaneously decreasing the concentrations of oxygen-free reaction products. With regard to the surface of the treated sample, this is of particular interest, as carbon soot or iron-carbides inhibit the thermochemical diffusion process of nitrocarburizing and accordingly the carburizing potential requires an *in-situ* control. This concluded in two experiments monitoring the concentrations of the major reaction products for the duration of 8 h, equivalent to a typical nitrocarburizing treatment. For most reaction products, no change of concentration in time was found, with the sole exception being CO. With admixture of O₂, the concentration of CO remained stable, while without admixture of O₂ the time dependency was assumed as an offset exponential decay, with the offset equivalent to a leakage of 2 sccm O₂. This also reflects the high surface area of the active screen made of carbon-fibre reinforced carbon, with the contamination of the reaction with oxygen being noticeable in every experiment measuring CO.

In agreement with previous studies, measurements at the industrial-scale determined a thermal equilibrium at the set process temperature measured with a thermocouple in the sample workload. However, for the laboratory-scale reactor the temperatures of N₂⁺, CH₃, CO, and HCN were found to scale differently with increasing plasma power at the active screen, explained by a spatial thermal-inhomogeneity of the interrogated volume. By assuming the rotational temperature of HCN to be representative of the temperatures of other oxygen-free reaction products, the concentrations of CH₃, CH₄, C₂H₂, C₂H₄, C₂H₆, C₂N₂, HCN, and NH₃ were determined as functions of the applied plasma power, feed gas mixture and pressure. With the exception of NH₃, the concentrations of all species were determined to rise with increasing plasma power at the active screen, while for NH₃ a maximum was noted at approximately 50 W plasma power.

The topic of rotational temperatures in the laboratory-scale reactor was revisited by application of a frequency comb source, novel to the field of plasma laser absorption spectroscopy. By matching the frequency comb with the lengths of the interferograms, recorded by a Michelson setup, the instrumental line shape function was effectively nullified. Subsequently line profile analysis of the approximately 1000 detected lines was possible for the four investigated applied power settings, resulting in high-precision Boltzmann plots of rovibrational bands of CH₄, C₂H₂, HCN, H¹³CN, HC¹⁵N, and NH₃. While the determined rotational temperatures agreed well with the values determined by use of lead-salt tuneable diode lasers and external-cavity quantum cascade lasers, it also validated the thermal equilibrium between the ground states of the stable species. Although the application of a frequency comb confirmed previous measurements of temperature and concentration, as well as assumptions of equilibria, the conducted study also serves as a testbed for the technique in plasma-chemical conditions.

In an additional study of plasma-chemical conditions in a microwave plasma-assisted chemical vapour deposition process for nanocrystalline diamond films, the significance of HCN and NH₃ as reaction

products even at low levels of N_2 admixture was shown. The production of HCN was shown to reduce the production of the hydrocarbon species, as HCN is very stable in the plasma phase [1]. Due to the reduced concentrations of hydrocarbon species and the presence of nitrogen resulting in species capable of etching the deposited diamond film, a high purity diamond film is produced. However, by analysis of the nitrogen and carbon mass balance, the presence of further undetected species such as N_2 , NH, H_2CN , C_2N_2 , CN, and H_2CO was inferred. Accordingly, a broad-band laser absorption spectroscopically study of the plasma-chemical condition of this environment would be reasonable to account for a larger part of the reaction products.

Currently three plasma nitrocarburizing reactors are at different stages of installation within the cooperation between the Leibniz Institute for Plasma Science and Technology and the Institute for Materials Engineering of the TU Freiberg. First, an industrial-scale warm-wall reactor, characterised by ohmic heaters placed into the wall of the reactor. This way, the crucial workload temperature is decoupled from the plasma power at the active screen, in turn the plasma-chemistry can be more precisely investigated without affecting the thermochemical diffusion process. Secondly, a laboratory-scale warm-wall reactor will improve upon the PLANIMOR device, by providing a much more homogeneous spatial temperature distribution inside the reactor. Furthermore, the reactor design enables sample treatments at the laboratory-scale. With this, links between the plasma-chemical composition and the treatment results are easier to establish. Finally, a laboratory-scale cold-wall reactor and successor to PLANIMOR is in the early stages of construction. The unique characteristic of this reactor is the implementation of attenuated total reflection (ATR) spectroscopy, an absorption spectroscopic tool to investigate plasma-surface interactions. As the volume of some hundred nanometres from a surface is interrogated, this technique gathers insight into the attachment of particles to a surface, which is of particular interest for the diffusion interface in plasma nitrocarburizing processes.

In parallel to the experimental work on the three new reactors, a frequency comb source will be applied to an industrial-scale reactor and in close to industrial conditions. While on the one hand, this will further insights into plasma nitrocarburizing, it also serves to establish the frequency comb as a robust spectroscopic tool for plasma-chemical analysis in industry.

Declaration

Hiermit erkläre ich, dass diese Arbeit bisher von mir weder an der Mathematisch-Naturwissenschaftlichen Fakultät der Universität Greifswald noch einer anderen wissenschaftlichen Einrichtung zum Zwecke der Promotion eingereicht wurde.

Ferner erkläre ich, dass ich diese Arbeit selbstständig verfasst und keine anderen als die darin angegebenen Hilfsmittel und Hilfen benutzt und keine Textabschnitte eines Dritten ohne Kennzeichnung übernommen habe. Die Stellen, die anderen Werken dem Wortlaut oder dem Sinne nach entnommen sind, habe ich in jedem Falle durch Angabe der Quelle, auch der Sekundärliteratur, als Entlehnung kenntlich gemacht.

Greifswald, den 06. Juli 2020

Curriculum Vitae

Personal details

Name Alexander Detlef Franziskus Puth
Date of birth 1th May 1991
Place of birth Aschaffenburg
Citizenship German
Contact alexander.puth@gmx.de

Education

2010 Abitur, Hanns-Seidel-Gymnasium in Hösbach
2010 – 2013 Bachelor of science in physics,
Goethe-University Frankfurt am Main
2013 Participation in the ERASMUS program at the University of Gothenburg, Sweden
XII 2013 Bachelor thesis: “Entwicklung & Untersuchung einer optischen Ansteuerung eines Thyristorstacks für sphärische Θ -Pinch Plasmaexperimente”
2014 – 2016 Master of science in physics,
Goethe-University Frankfurt am Main
XII 2016 Master thesis: “Aufbau & elektrische Charakterisierung eines Screwpinch Plasma”

Experience

2017 – 2020 Researcher at the Leibniz Institute for Plasma Science and Technology,
Department Plasma Chemical Processes
Focus of research: IR molecular spectroscopy, laser absorption spectroscopy
2017 – 2020 Continuous collaborative exchange with the TU Bergakademie Freiberg
2017 – 2020 Continuous collaborative exchange with the Nicolaus Copernicus University in Torun
2018 – 2020 Continuous collaborative exchange with the University Paris 13

Peer-reviewed publications

- 1 **Puth A**, Hamann S, Kusýn L, Burlacov I, Dalke A, Spies H-J, Biermann H, and Röpcke J; “Spectroscopic investigations of plasma nitrocarburizing processes using an active screen made of carbon in a model reactor” 2018 *Plasma Sources Sci. Technol.* **27** 075017
- 2 Dalke A, Burlacov I, Hamann S, **Puth A**, Spies H-J, Röpcke J, and Biermann H; “Plasma Nitrocarburizing of AISI 316L Austenitic Stainless Steel Applying a Carbon Active Screen: Status and Perspectives” 2018 *HTM J. Heat Treatm. Mat.* **73** 246 – 257
- 3 Dalke A, Burlacov I, Hamann S, **Puth A**, Böcker J, Spies H-J, Röpcke J, and Biermann H; “Solid carbon active screen plasma nitrocarburizing of AISI 316L stainless steel: Influence of N₂-H₂ gas composition on structure and properties of expanded austenite” 2019 *Surf. Coat. Technol.* **357** 1060 – 1068
- 4 **Puth A**, Kusýn L, Pipa A V, Burlacov I, Dalke A, Hamann S, van Helden J H, Biermann H, and Röpcke J; “Spectroscopic study of plasma nitrocarburizing processes with an industrial-scale carbon active screen” 2020 *Plasma Sources Sci. Technol.* **29** 035001
- 5 Jafarpour S M, **Puth A**, Dalke A, Böcker J, Pipa A V, Röpcke J, van Helden J H, and Biermann H; “Solid carbon active screen plasma nitrocarburizing of AISI 316L stainless steel in cold wall reactor: Influence of plasma conditions” 2020 *J. Mater. Res. Technol.* **9** 9195 – 9205
- 6 Dekkar D, **Puth A**, Bisceglia E, Moreira P W T jr., Pipa A V, Lombardi G, Röpcke J, van Helden J H, and Bénédic F; “Effect of admixture of N₂ to low pressure, low temperature H₂-CH₄-CO₂ microwave plasmas used for large area deposition of nanocrystalline diamond films” 2020 *J. Phys. D: Appl. Phys.* – submitted manuscript

Contributions to conferences and workshops

(Presenter underlined)

- 1 Puth A, Hamann S, Burlacov I, Lang N, Dalke A, Spies H-J, van Helden J H, and Röpcke J; “Plasma-chemical study of plasma nitriding processes with an active carbon screen” 2017 International Summer School on Low Temperature Plasma Physics, Bad Honnef (Poster)
- 2 Hamann S, Burlacov I, Spies H-J, Biermann H, van Helden J H, Lang N, Maslowski P, Kowzan G, Puth A, and Röpcke J; “Spectroscopical investigations of plasma nitriding processes using different active screen materials” 2017 OSA Light, Energy and the Environment Congress, Boulder CA (Oral)
- 3 Puth A, Hamann S, Kusýn L, Burlacov I, Dalke A, Spies H-J, Biermann H, and Röpcke J; “Spectroscopic investigations of plasma nitrocarburizing processes using an active screen made of carbon in a model reactor” 2018 8th International Workshop and Summer School on Plasma Spectroscopy, Oxford (Poster)
- 4 Lang N, Puth A, Klose S-J, Kowzan G, Hamann S, Röpcke J, Maslowski P, and van Helden J H; “Direct mid-infrared frequency comb spectroscopy of nitrocarburizing plasma processes” 2018 8th International Workshop and Summer School on Plasma Spectroscopy, Oxford (Poster)
- 5 Puth A, Hamann S, Kusýn L, Burlacov I, Dalke A, Spies H-J, Biermann H, van Helden J H, and Röpcke J; “Plasma chemical study of plasmanitriding processes with an active carbon screen” 2018 DPG Spring meeting, Erlangen (Oral)
- 6 Lang N, Puth A, Klose S-J, Kowzan G, Hamann S, Röpcke J, Maslowski P, and van Helden J H; “Plasma-surface interaction studies: Development and application of advanced laser-based diagnostics”, 2018 45th Conference on Plasma Physics, Prague (Oral)
- 7 Lang N, Puth A, Klose S-J, Kowzan G, Hamann S, Röpcke J, Maslowski P, and van Helden J H; “Mid-infrared frequency comb spectroscopy for plasma-surface interaction studies” 2018 GRC Plasma Processing Science, Smithfield RI (Oral)
- 8 Lang N, Puth A, Klose S-J, Kowzan G, Hamann S, Röpcke J, Maslowski P, and van Helden J H; “Direct mid-infrared frequency comb spectroscopy of nitrocarburizing plasma processes” 2018 8th International Workshop and Summer School on Plasma Spectroscopy, Oxford (Oral)
- 9 Lang N, Puth A, Klose S-J, Kowzan G, Hamann S, Röpcke J, Maslowski P, and van Helden J H; “Direct mid-infrared frequency comb spectroscopy of nitrocarburizing plasma processes” 2018 Fourier Transform Spectroscopy meeting of the OSA Light, Energy and the Environment Congress, Singapore (Oral)
- 10 Lang N, Puth A, Klose S-J, Kowzan G, Hamann S, Röpcke J, Maslowski P, and van Helden J H; “Spectroscopic investigations of plasma nitrocarburizing processes with a mid-infrared frequency comb” 2018 DPG Spring meeting, Erlangen (Oral)
- 11 Lang N, Puth A, Klose S-J, Kowzan G, Hamann S, Röpcke J, Maslowski P, and van Helden J H; “Spectroscopic Investigations of Plasma Nitrocarburizing Processes with a Mid-infrared Frequency Comb” 2018 Mid-Infrared Coherence Sources, Strasbourg (Oral)
- 12 Puth A, Hamann S, Kusýn L, Burlacov I, Dalke A, Spies H-J, Biermann H, and Röpcke J; “Spectroscopic investigations of plasma nitriding processes using an active carbon screen” 2018 OSA Light, Energy and the Environment Congress, Singapore (Oral)
- 13 Puth A, Hamann S, Kusýn L, Burlacov I, Dalke A, Spies H-J, Biermann H, Röpcke J, and van Helden J H; “Plasma-chemical studies of nitrocarburizing with an active screen made of

- carbon in laboratory and industrial scale reactors” 2019 13th Frontiers in Low-Temperature Plasma Diagnostics, Bad Honnef (Poster)
- 14 Lang N, Puth A, Klose S-J, Kowzan G, Hamann S, Röpcke J, Maslowski P, and van Helden J H; “Comprehensive quantitative plasma diagnostics using a mid-infrared frequency comb for analysing an industrial plasma process” 2019 13th Frontiers in Low-Temperature Plasma Diagnostics, Bad Honnef (Poster)
- 15 Lang N, **Puth A**, Klose S-J, Kowzan G, Hamann S, Röpcke J, Maslowski P, and van Helden J H; “Mid-infrared direct frequency comb spectroscopy of plasma processes” 2019 13th Frontiers in Low-Temperature Plasma Diagnostics, Bad Honnef (Oral)
- 15 Lang N, Puth A, Klose S-J, Kowzan G, Hamann S, Röpcke J, Maslowski P, and van Helden J H; “Comprehensive quantitative plasma diagnostics using a mid-infrared frequency comb for analysing an industrial plasma process” 2019 3rd European Conference on Plasma Diagnostics, Lisbon (Poster)
- 16 **Puth A**, Lang N, Dalke A, Biermann H, Maslowski P, Röpcke J, and van Helden J H; “Spectroscopic investigation of a nitrocarburizing plasma utilizing a frequency comb” 2019 19. Fachtagung für Plasmatechnologie, Cottbus (Poster)
- 17 **Puth A**, Lang N, Klose S-J, Maslowski P, Nishiyama A, Dalke A, Biermann H, van Helden J H, and Röpcke J; “Plasma chemical studies of nitrocarburizing plasmas in laboratory reactors using direct frequency comb spectroscopy” 2019 DPG Spring meeting, Munich (Oral)
- 18 Lang N, **Puth A**, Klose S-J, Kowzan G, Hamann S, Röpcke J, Maslowski P, and van Helden J H; “Demonstration of mid-infrared direct frequency comb spectroscopy for analysing plasma processes” 2019 19th Laser Aided Plasma Diagnostics, Whitefish MT (Oral)

Acknowledgment

Working in the scientific field is always a social endeavour and this thesis is no exception from this rule. First and foremost, I would thank Prof. Jürgen Röpcke for his support, drive, and care towards the projects and my personal progress. Thanks to him, the plasma diagnostics group of INP is a productive environment, where generations of previous PhD students and researchers accumulated a wealth of knowledge, as I did within the last 4 years.

The completion of this thesis would in no way have been possible without the scientific and technical discussions and input, provided by my group. In no particular order, I want to thank Dr. Jean-Pierre van Helden, Prof. Ronnie Brandenburg, Dr. Andrei Pipa, Sarah-Johanna Klose, Dr. Stephan Hamann, Dr. Mario Hannemann, Dr. Norbert Lang, and Dr. Andy Nave, as well as Frank Weichbrodt, Uwe Macherius, Mathias Wiese, Sven Glitsch, and Henrik Zimmermann. If anyone can be commended beyond the others, it would be Frank Weichbrodt, Stephan Hamann, and Andrei Pipa, due to their immense contributions to my daily lab life and the measurement campaigns that form the backbone of my thesis. Furthermore, two interns contributed considerably to measurement campaigns: Lukas Kusýn, now a PhD student with Jan Voráč at the Masaryk University, Czech Republic, and Pedro Moreira, who finished his PhD in 2019. Finally, the workshop and administration of INP Greifswald deserve my gratitude for a reliable service over the years in all manners of working life.

Beyond the INP, I want to thank the group of Prof. Horst Biermann and Dr. Anke Dalke, including Dr. Igor Burlacov, Jan Böcker, Dr. Saeed Jafarpour, and Siegismund Eckehard, for our collaboration that started more than 10 years ago and is the centre point of my thesis. The collaboration is still alive and healthy and I hope that future PhD students benefit from the high level of professional exchange I was enjoying.

My gratitude extends to Prof. Piotr Maslowski and his team, namely Dr. Grzegorz Kowzan and Dr. Akiko Nishiyama, for their support in matters of the frequency comb, that was both practically as well as theoretically excellent and a joy too. The company Menlo Systems, in particular Maximilian Bradler, are thanked for providing a great customer support and the comb itself.

A third enjoyable collaboration was with the University Paris 13, Prof. Guillaume Lombardi, Dr. Fabienne Bénédic and their PhD students Enrico Bisceglia and Damia Dekkar, respectively. I wish the two of them the very best for their thesis, as they deserve no less.

Moreover, a final thanks is directed to Rübige Technology GmbH, for providing everything one can wish for during our measurement campaign in Wels, Austria.

With such a wonderful professional life, the friends and family also deserve praise partaking and continuous support. First and foremost Dieter, Stephanie, and Philipp, their significant others and significant smaller ones, that seem to increase in height and number with every other passing year of my studies.

Finally, I want to thank last but not least my friends Rahel, Christine, Julia, Delia, Thorben, Christina, Ramona, Sehoon, Thalita, Felipe, Laura, Miguel, Jasmin, Sarah, Andrea, Sasha, Lukas, Tijes, and Jente and continuing on. Honouring all dear friends would be a herculean task and I am grateful for that.